Tampereen teknillinen korkeakoulu
Julkaisuja 384

Tampere University of Technology
Publications 384

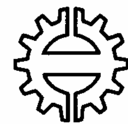

Mika Saarinen

Visible Vertical-Cavity Light Emitters

Tampere 2002

Tampereen teknillinen korkeakoulu
Julkaisuja 384

Tampere University of Technology
Publications 384

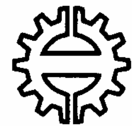

Mika Saarinen

Visible Vertical-Cavity Light Emitters

Thesis for the degree of Doctor of Technology to be presented with due permission for public examination and criticism in Tietotalo Building, Auditorium TB103, at Tampere University of Technology, on the 27th of September 2002, at 12 o'clock noon.

Tampere 2002

ISBN 952-15-0867-1 (printed)
ISBN 952-15-1412-4 (PDF)
ISSN 0356-4940

TTKK- PAINO, Tampere 2002

Abstract

This Thesis is concerned with resonant cavity light-emitting diodes (RCLEDs) and vertical-cavity surface-emitting lasers (VCSELs), which oscillate in the visible spectral range. It presents results obtained from studies of layer growth and device structures and the potential of RCLEDs and VCSELs as light sources for optical data communication systems at short wavelengths. In particular, it demonstrates the applicability of molecular beam epitaxy (MBE) for monolithic growth of RCLEDs and VCSELs complete with quantum wells, microcavities, and distributed Bragg reflectors, oriented perpendicular to the *p-n* junctions of the devices.

Low-cost communication systems based on standard polymethyl methacrylate (PMMA) plastic optical fibres (POFs) require reliable and inexpensive light sources that operate at 650 nm, where the fibre exhibits a local attenuation minimum. The RCLEDs of this Thesis are mainly intended for such applications.

The Thesis first presents a historical background and basic design concepts of vertical-cavity light emitters. Then theoretical considerations are given where appropriate to support the experimental work and to provide theoretical explanations for the observed phenomena. A detailed description of the fibre coupling efficiency, temperature behaviour, and the overall performance of closely optimised 650-nm RCLEDs is given. Finally, characteristics of preliminary 690-nm AlGaInP / GaAs VCSELs are discussed.

Preface

This work has been carried out at Optoelectronics Research Centre (ORC) of Tampere University of Technology (TUT), and in co-operation with research institutes and companies.

The results presented in this Thesis are obtained, in part, within European Union projects, such as SMILES, SMILED, COST-268 and national program COST-268B.

I wish to thank all my colleagues at ORC and other co-operating researchers elsewhere as well as the companies involved for many fruitful discussions and assistance. In particular, I am grateful to the Director of ORC, Professor Markus Pessa, who has been my supervisor, and Dr. Mika Toivonen, Dr. Pekka Savolainen, and Dr. Mihail Dumitrescu. Special thanks are due to Dr. Petteri Uusimaa for guiding me to the miraculous world of crystal growth. I would like to thank also my colleagues Dr. Ning Xiang, Mircea Guina, Petri Melanen, Seppo Orsila, Pekko Sipilä, and Ville Vilokkinen for their valuable contribution.

I wish to express my gratitude to my current employer, Modulight, Inc., for supporting me during the preparation of this Thesis.

Finally, I thank my family for supporting me during my studies and writing this work.

This work was supported, in part, by Material Physics Graduate School (Helsinki University of Technology) and Jenny and Antti Wihuri Foundation, which are gratefully acknowledged.

Tampere, June 2002

Mika Saarinen

Contents

Abstract i
Preface ii
Contents iii
List of publications iv
Author's contribution ix
Abbreviations x

1. Introduction 1
   1.1 History of vertical cavity emitters 2
   1.2 VCSEL and RCLED geometries 4
   1.3 Material system 9
2. Emission characteristics 13
   2.1 RCLEDs 13
      2.1.1 Microcavity effects 13
      2.1.2 Figures of merit 20
      2.1.3 Emission pattern and fibre coupling 20
      2.1.4 Modulation response of RCLED 24
      2.1.5 Applications of visible RCLEDs 25
   2.2 VCSELs 26
      2.2.1 Lasing action 26
      2.2.2 Polarisation 28
      2.2.3 Thermal model 29
      2.2.4 Modulation response of VCSELs 30
   2.3 Plastic optical fibres 31
3. Design and development of visible RCLEDs and VCSELs 34
   3.1 Design and simulation 34
   3.2 Material growth 37
   3.3 Device processing 42
   3.4 Characterisation 43
4. Experimental results 46
   4.1 RCLEDs 46
      4.1.1 Output characteristics 46
      4.1.2 Modulation response 50
      4.1.3 Temperature coefficient 53
      4.1.4 Reliability 53
      4.1.5 Plastic optical fibre coupling 54
   4.2 VCSELs 56
      4.2.1 Output characteristics 56
      4.2.2 Reliability 58
5. Final remarks 60

References 62
Appendices 74

List of publications

This Thesis consists of the following papers:

1. P. Sipilä, M. Saarinen, M. Guina, V. Vilokkinen, M. Toivonen, and M. Pessa, 'Temperature behaviour of resonant cavity light-emitting diodes at 650 nm', *Semiconductor Science and Technology*, **15**, 418 (2000)

2. M. Dumitrescu, L. Toikkanen, P. Sipilä, V. Vilokkinen, P. Melanen, M. Saarinen, S. Orsila, P. Savolainen, M. Toivonen, and M. Pessa, 'Modeling and optimization of resonant cavity light-emitting diodes grown by solid source molecular beam epitaxy', *Microelectronic Engineering*, **51-52**, 449 (2000)

3. M. Guina, S. Orsila, M. Dumitrescu, M. Saarinen, P. Sipilä, V. Vilokkinen, B. Roycroft, P. Uusimaa, M. Toivonen, and M. Pessa, 'Light-emitting diode emitting at 650 nm with 200-MHz small-signal modulation bandwidth', *IEEE Photonics Technology Letters*, **12**, 786 (2000)

4. M. Guina, J. Dekker, A. Tukiainen, S. Orsila, M. Saarinen, M. Dumitrescu, P. Sipilä, P. Savolainen, and M. Pessa, 'Influence of deep level impurities on modulation response of InGaP light emitting diodes', *Journal of Applied Physics*, **89**, 1151 (2001)

5. M. Saarinen, V. Vilokkinen, M. Dumitrescu, and M. Pessa, 'Resonant-cavity light-emitting diodes operating at 655 nm with high external quantum efficiency and light power', *IEEE Photonics Technology Letters*, **13**, 10 (2001)

6. M. Pessa, M. Guina, M. Dumitrescu, I. Hirvonen, M. Saarinen, L. Toikkanen, and N. Xiang, 'Resonant cavity light emitting diode for a polymer optical fibre system', *Semiconductor Science and Technology*, *Topical Review*, **17**, R1 (2002)

7. M. M. Dumitrescu, M. J. Saarinen, M. D. Guina, and M. V. Pessa, 'High speed resonant cavity light emitting diodes at 650 nm', *IEEE Journal of Selected Topics in Quantum Electronics*, **8**, 219 (2002)

8. M. Saarinen, M. Toivonen, N. Xiang, V. Vilokkinen, and M. Pessa, 'Room-temperature CW operation of red vertical-cavity surface-emitting lasers grown by solid-source molecular beam epitaxy', *Electronics Letters*, **36**, 1210 (2000)

9. M. Saarinen, V. Vilokkinen, P. Sipilä, N. Xiang, S. Orsila, M. Guina, P. Melanen, M. Dumitrescu, P. Uusimaa, P. Savolainen, and M. Pessa, 'Visible vertical cavity light emitters for fibre optical communication', (Invited Paper), *Electrochemical Society XXXIII SOTAPOCS Proceedings*, **18**, 49 (2000)

10. M. Saarinen, N. Xiang, V. Vilokkinen, P. Melanen, S. Orsila, P. Uusimaa, P. Savolainen, M. Toivonen, and M. Pessa, 'Red vertical-cavity surface-emitting lasers grown by solid-source molecular beam epitaxy', *Journal of Crystal Growth*, **227-228**, 324 (2001)

11. M. Saarinen, N. Xiang, M. Dumitrescu, V. Vilokkinen, P. Melanen, S. Orsila, P. Uusimaa, P. Savolainen, and M. Pessa, 'Visible-light vertical-cavity surface-emitting lasers grown by solid-source molecular beam epitaxy', *SPIE Proceedings*, **4286**, 156 (2001)

12. M. Dumitrescu, M. Saarinen, N. Xiang, M. Guina, V. Vilokkinen, and M. Pessa, 'Red wavelength range microcavity emitters', *Physica Status Solidi (A)*, **188**, 943 (2001)

13. M. Saarinen, N. Xiang, M. Dumitrescu, M. Guina, I. Hirvonen, L. Toikkanen, and M. Pessa, 'Vertical cavity light emitters for plastic optical fibers', (Invited Paper), accepted for publication, 2002 issue, *Physica Scripta* (2002)

Other papers related to this work but not included in the Thesis:

1. P. Uusimaa, P. Sipilä, M. Saarinen, L. Toikkanen, A. Rinta-Möykky, and M. Pessa, 'Molecular beam epitaxy growth of MgZnSSe/ZnSSe/CdZnSe microcavity light-emitting diodes using in situ reflectance monitoring', *Journal of Crystal Growth*, **201-202**, 1032 (1999)

2. M. Saarinen, S. Orsila, M. Toivonen, P. Savolainen, T. Kuuslahti, V. Vilokkinen, P. Melanen, P. Sipilä, and M. Pessa, 'Solid source molecular beam epitaxy growth and characteristics of resonant cavity light-emitting diodes', *SPIE Proceedings*, **2621,** 230 (1999)

3. P. Savolainen, M. Toivonen, S. Orsila, M. Saarinen, P. Melanen, V. Vilokkinen, P. Sipilä, and M. Pessa, 'Solid-source molecular beam epitaxy of phosphide-based optoelectronic devices', *Recent Developments in Vacuum Science and Technology*, **1**, 1 (1999)

4. J. Dekker, A. Tukiainen, N. Xiang, S. Orsila, M. Saarinen, M. Toivonen, and M. Pessa, 'Annealing of the deep recombination center in GaInP/AlGaInP quantum wells grown by solid-source molecular beam epitaxy', *Journal of Applied Physics*, **86**, 3709 (1999)

5. S. Orsila, M. Toivonen, P. Savolainen, V. Vilokkinen, P. Melanen, M. Pessa, M. Saarinen, P. Uusimaa, P. Corvini, F. Fang, M. Jansen, and R. Nabiev, 'High power 600 nm range lasers grown by solid source molecular beam epitaxy', *SPIE Proceedings,* **3628**, 203 (1999)

6. P. Savolainen, M. Toivonen, S. Orsila, M. Saarinen, P. Melanen, V. Vilokkinen, M. Dumitrescu, T. Panarello, and M. Pessa, 'AlGaInAs/InP strained-layer quantum well lasers at 1.3 μm grown by solid source molecular beam epitaxy', *Journal of Electronics Materials*, **28**, 980 (1999)

7. M. Pessa, M. Toivonen, P. Savolainen, S. Orsila, P. Sipilä, M. Saarinen, P. Melanen, V. Vilokkinen, P. Uusimaa, and J. Haapamaa, 'Growth of resonant cavity quantum well light emitting diodes and two-junction solar cells by solid source molecular beam epitaxy', *Thin Solid Films*, **367**, 260 (2000)

8. P. Sipilä, M. Saarinen, V. Vilokkinen, S. Orsila, P. Melanen, P. Savolainen, M. Toivonen, M. Dumitrescu, and M. Pessa, 'Resonant cavity LEDs at 655 and 880 nm wavelengths', *SPIE Proceedings*, **3938**, 82 (2000)

9. V. Vilokkinen, P. Sipilä, P. Melanen, M. Saarinen, S. Orsila, M. Dumitrescu, P. Savolainen, M. Toivonen, and M. Pessa, 'Resonant cavity light-emitting diodes at 660 and 880 nm', *Materials Science & Engineering* B, **74**, 165 (2000)

10. M. Guina, T. Jouhti, M. Saarinen, P. Sipilä, A. Isomäki, P. Uusimaa, O. Okhotnikov, and M. Pessa, '622 Mbit/s data transmission using 650 nm resonant-cavity light-emitting diodes and plastic optical fiber', *POF2000 Proceedings*, **2000**, 49 (2000)

11. M. Dumitrescu, P. Sipilä, V. Vilokkinen, L. Toikkanen, P. Melanen, M. Saarinen, S. Orsila, P. Savolainen, M. Toivonen, and M. Pessa, 'Resonant cavity light-emitting diodes: modeling, design, and optimization', *SPIE Proceedings*, **4068**, 597 (2000)

12. N. Xiang, J. Likonen, J. Turpeinen, M. Saarinen, M. Toivonen, and M. Pessa, 'Influence of oxygen incorporation on beryllium- and silicon-doped InP grown by solid source molecular beam epitaxy', *SPIE Proceedings*, **4086**, 72 (2000)

13. M. Pessa, M. Dumitrescu, M. Guina, I. Hirvonen, M. Saarinen, P. Sipilä, L. Toikkanen, V. Vilokkinen, and N. Xiang, 'Progress in developing visible RC-LEDs for polymer optical fibre systems', (Invited Paper), *Compound Semiconductor Outlook 2001 Proceedings*, (2001)

14. S. Orsila, P. Uusimaa, M. Saarinen, M. Toivonen, P. Sipilä, V. Vilokkinen, P. Melanen, M. Guina, M. Dumitrescu, M. Pessa, 'Resonant cavity light-emitting diodes grown by solid source MBE', *Journal of Crystal Growth*, **227-228**, 346 (2001)

15. M. Dumitrescu, M. Saarinen, V. Vilokkinen, P. Sipilä, M. Guina, and M. Pessa, 'Visible-light emitting diodes based on microcavity concepts', *SPIE Proceedings,* **4278**, 50 (2001)

16. M. Dumitrescu, M. Pessa, M. Saarinen ja N. Xiang, 'Suuren hyötysuhteen omaava puolijohdevalolähde ja menetelmä sen valmistamiseksi'. Hakemusnumero FI20010878, patent application (2001)

17. N. Xiang, M. Guina, A. Vainionpää, J. Lyytikäinen, S. Suomalainen, M. Saarinen, O. Okhotnikov, T. Sajavaara, and J. Keinonen, 'Broadband semiconductor saturable absorber mirrors in the 1.55 μm wavelength range for pulse generation in fiber lasers', *IEEE Journal of Quantum Electronics*, **38**, 369 (2002)

Author’s contribution

This Thesis includes 13 papers published in the open literature. It is a result from my own work and co-operation with other researchers. During these years I have been working on the SSMBE technology and have been developing and maintaining the SSMBE reactors. I have prepared suitable procedures to manufacture complex epitaxial structures and grown the device structures using the technologies provided by Tampere University of Technology.

I have characterised structural, electrical, and optical properties of many of the materials presented here. The characterisation includes measurements of double-crystal X-ray diffraction rocking curves, photoluminescence, Hall effect properties, reflectivity properties *etc*. Simulation tools are nowadays essential part of characterisation processes. I have simulated, *e.g.,* the rocking curves and resonance component reflectivities and closely co-operated with simulation experts.

A list of my contribution to preparing the scientific papers and crystal growth related research work is given in the Table below.

Table. *Author’s contribution to the papers and related research work.*

Paper #	Author’s contribution in writing the paper	Author’s contribution in crystal growth and related research work
1	co-author (33 %)	group work (50 %)
2	co-author (33 %)	group work (33 %)
3	co-author (20 %)	group work (50 %)
4	co-author (20 %)	group work (50 %)
5	main author	main research work
6	co-author (50 %)	main research work
7	co-author (50 %)	main research work
8	main author	group work (33 %)
9	main author	group work (20 %)
10	main author	group work (33 %)
11	main author	group work (33 %)
12	co-author (33 %)	group work (50 %)
13	main author	group work (50 %)

Abbreviations

AR	antireflection
ATM	asynchronous transfer mode
CCD	charged coupled device
CD	compact disc
COD	catastrophic optical damage
CQED	cavity quantum electrodynamics
CRVCL	coupled resonator vertical cavity laser
CW	continuous wave
DBR	distributed Bragg reflector
DC	direct current
DFB	distributed feed-back
DLTS	deep level transmission spectroscopy
DOE	diffractive optical element
DVD	digital versatile disc, digital video disc
EEL	edge-emitting laser
F-P	Fabry-Perot
FWHM	full width of half maximum
GI	graded-index
GSMBE	gas-source MBE
HDTV	high definition television
HR	high reflection
ICTS	isothermal capacitance spectroscopy
IR	infra-red
IVBA	inter-valence band absorption
LAN	local area network
LED	light-emitting diode
LM	lattice-matched
MBE	molecular beam epitaxy
MCM	multi-chip module
MOCVD	metal organic chemical vapor deposition
MOST	media oriented system transport
MOVPE	metal organic vapor phase epitaxy
MTTF	mean time to failure
NA	numerical aperture
ORC	Optoelectronics Research Centre
PF	perfluorinated
PL	photoluminescence
PMMA	polymethyl methacrylate
POF	plastic optical fibre, polymer optical fibre
PR	photomodulated reflectance
PS	polarisation switching
QW	quantum well
RCLED	resonant cavity light-emitting diode
REA	recombination enhanced annealing
RT	room temperature
RTA	rapid thermal annealing

SEM	scanning electron microscopy
SI	step-index, semi-insulating
SIMS	secondary ion mass spectroscopy
SNOM	scanning near-field optical microscopy
SQW	single quantum well, strained quantum well
TBA	tertiarybutylarsine
TBP	tertiarybutylphosphide
TC	temperature coefficient
TEM	transmission electron microscopy
TIP	truncated-inverted-pyramid
TRPL	time-resolved PL
TUT	Tampere University of Technology
UD	undoped
UHV	ultra-high vacuum
VCSEL	vertical-cavity surface-emitting laser
XRD	X-ray diffraction

1. Introduction

The recent development in optical communication has lead to the birth of a whole new class of light sources and receivers with unprecedented performance characteristics tailored to meet the requirements of specific applications. For example, low-cost short-haul communications systems based on polymethyl methacrylate (PMMA) plastic optical fibres (POFs) require inexpensive light sources that would operate in the red wavelength range, where PMMA-POF exhibits a local attenuation minimum. Very promising light sources for these applications are resonant cavity light-emitting diodes (RCLEDs) and vertical-cavity surface-emitting lasers (VCSELs).

One of the main objectives of this Thesis has been to investigate the properties of novel light emitters grown by the molecular beam epitaxy (MBE) method and to study the capacity of these devices for optical communication applications. Another goal has been to explore new areas where the visible-light RCLEDs or VCSELs could possibly be used.

In this Thesis, state-of-the-art 650-nm resonant cavity light-emitting diodes, closely optimised for short-haul PMMA-POF based communication systems, and probably the first MBE-grown AlGaInP-based VCSELs at 690 nm are presented. Design concepts, modelling approaches, fabrication issues, and performance characteristics are discussed. In the introductory part, a history of vertical cavity emitters is outlined, followed by a discussion on basic concepts of device geometry. Both the layer structure variants and emitter topologies are considered. The material systems used are shortly described, too.

Emission characteristics of RCLEDs and VCSELs are the theme of the second chapter. Microcavity effects, figures of merit, and emission patterns of RCLEDs and to some extent those of VCSELs are presented. The emphasis is laid on RCLEDs because VCSELs are much better known components and are discussed in a number of textbooks. A modulation response is an important feature of light emitters. Both the modulation of spontaneous emission and stimulated emission are considered here, and their applications are discussed.

The third chapter is concerned with the actual design and fabrication of red vertical cavity components.

Experimental results are compiled in the end of the Thesis. Besides crystal growth, the Author has studied device characteristics, notably, optimisation of the external quantum efficiency of the RCLEDs, far-field distribution, small-signal modulation capabilities, and the fibre coupling efficiency. Regarding the VCSELs, the Author has paid much attention to finding out proper growth conditions and an internal layer structure.

The Thesis is concluded by final remarks and the summary of the results.

1.1 History of vertical cavity emitters

Since their first demonstration in 1962[1,2], semiconductor lasers have gone a long way to become part of our modern technology and consumer markets. Lasers are present in CD and DVD players, bar code scanners, printers, medical applications, optical communication, and many more. Semiconductor lasers are attractive due to their small dimensions, low cost, and ease of operation. Most of commercial diode lasers are edge-emitting lasers (EELs), whose cavity is in the plane of the *p*-*n* junction, and the output beam emerges from the edge of the chip. The cavity has cleaved mirror facets, which may be coated with high-reflection (HR) or antireflection (AR) layers. Optical gain is obtained in the active region, which usually consists of quantum wells (QWs), by injecting current to a *pn*-junction. Several improvements in device design have been introduced to achieve a low threshold current density, high efficiency, controlled emission mode, and reliable operation. Operation at long wavelengths, 1.3-1.55 µm, is required for fibre-optical communications applications, due to superior transmission characteristics of standard silica fibres at these wavelengths. For example, distributed Bragg reflector (DBR) EELs and distributed feed-back (DFB) EELs with high single-mode output power are widely used in commercial applications.

Vertical-cavity surface-emitting lasers, VCSELs, are promising alternatives to the EELs. In VCSELs the cavity is oriented perpendicular to the surface of a substrate to allow for emission in the vertical direction. The overall cavity length is much shorter for a VCSEL than for an in-plane edge-emitting laser, typically a few micrometers (µm) compared to some hundreds of µm of the in-plane lasers. The short cavity results in a short gain region and high mode selectivity, which means that the longitudinal mode spacing is large. Therefore, the mirror reflectivity must be high so that the round-trip gain can compensate all optical losses in the cavity and the mirrors.

The first VCSEL was pioneered by Soda and his co-workers in 1979[3]. This InGaAsP/InP device had metallic mirrors and it operated under pulsed mode at liquid nitrogen temperature (77 K) with a high threshold current. However, it was not until the late 1980's[4] that continuous-wave (CW) low-threshold-current VCSELs were demonstrated at room temperature (RT) and their practical viability for numerous applications began to be recognised. In the early years, researchers concentrated on GaAs-based devices operating in the wavelength range from 850 to 980 nm[5]. This was because the inherent properties of the GaAs material system provide good lattice matching and ease of making the DBRs and active regions. VCSELs oscillating at 850 nm[6] and 980 nm[7] are mature and they are now in the market. They are used, for example, in short-distance optical fibre datacom network applications (Local Area Network, ATM, Ethernet modules, Gigabit Fibre Channel Modules *etc*.). On the other hand, the laser performance of long wavelength VCSELs (1.3 or 1.55 µm) have been hampered by very substantial difficulties related to their fabrication. Auger recombination and inter-valence band absorption (IVBA) in addition to low refractive index contrast in InP/InGaAsP have been the main problems. Wafer fusion is used as a solution to manufacturing VCSELs for long wavelengths[8], but it is not ready to be implemented directly to high-yield mass production. After the demonstration of the first 1.3-µm GaInNAs-based EELs[9,10] it has become clear that the same active region design can be employed to VCSELs on GaAs substrate[11]. Of crucial importance for

the potential of long-wavelength nitride VCSELs will be their ability to compete with more matured in-plane lasers in terms of performance characteristics, fabrication costs, and reliability.

The first electrically injected visible VCSELs, which operated between 639 and 661 nm in pulsed mode, and launched a peak power of 3.3 mW from a $^{\varnothing}$20-μm device, were demonstrated in 1993[12]. The laser consisted of AlAs/AlGaAs DBRs and an extended AlGaInP optical cavity (8-λ) with three GaInP quantum wells that favoured n = 2 quantum well transitions[13]. In the same year, a 699-nm phosphorus-free VCSEL, having an AlAs/GaAs superlattice active region, was demonstrated[14], but poor carrier confinement and low optical efficiency yielded only modest device characteristics. Room temperature continuous wave (CW) operation of red VCSEL was achieved in 1993[15]. This $^{\varnothing}$15-μm *mesa* VCSEL had a threshold current of 5 mA and peak output power (P_{out}) of 25 μW at 670 nm. Soon Sandia National Laboratories fabricated a monolithic 676-nm 1-λ-cavity AlGaInP VCSEL with a record-high CW P_{out} of 2.9 mW[16] and a wall-plug efficiency (η_{wp}) of 10 %. The Sandia group also prepared a planar-implanted VCSEL operating at λ = 687 nm with P_{out} = 8.2 mW (CW) and power conversion (wall plug) efficiency of 11 %. This VCSEL had single-mode operation up to 1.9 mW[17]. Better material quality, optimised doping, graded interfaces, and a shorter optical cavity length (1-λ) have reduced optical losses in the vicinity of the gain region and improved thermal conductivity.

Large- and small-signal properties of visible VCSELs have been studied intensively. A small-signal bandwidth of 11 GHz with a bias current of 16 mA at 670 nm[18] and large-signal modulation speed up to 1.5 Gbit/s[19] have been demonstrated.

Light-emitting diodes (LEDs) are based on spontaneous emission from a *pn*-junction. A traditional LED is a simple component, which radiates in all directions from the recombination area. Recently, several new designs giving rise to high efficiency, high extraction power or directional output beam have been demonstrated. New design considerations with high extraction efficiency will be described in Section 1.2 of this Thesis. RCLEDs were introduced for the first time in 1992 by Schubert and his co-workers[20]. The device operated at 862 nm and consisted of AlAs/AlGaAs DBRs and an AlGaAs active region with GaAs quantum wells, all grown monolithically by MBE. CW operation of a monolithic visible RCLED was reported in 1993[21]. This MOCVD-grown device had AlAs/AlGaAs DBRs and an AlGaInP cavity with compressively strained GaInP quantum wells operating at 661 nm and launching peak power of 20 μW. A 670-nm RCLED with AlInP/AlGaInP DBRs was demonstrated by the same group in 1993[22]. Since then, various material systems have been used to fabricate RCLEDs: AlGaAs/GaInAs/GaAs for IR-RCLEDs[23], InGaAsP/InP for 1.3-μm RCLEDs[24] and numerous metal/semiconductor/dielectric hybrids[25]. Furthermore, RCLEDs made of II-VI semiconductors have been demonstrated in the 500-nm range[26,27].

Monolithic red RCLEDs with high P_{out}, external quantum efficiency (η_e)[28] and modulation speed[29] have been reported by Mitel Semiconductor (Zarlink Semiconductor). Recently, our group has demonstrated a state-of-the-art η_e of 9.5 %[30] and over 350 MHz modulation speed[31], achieved by 650-nm oxide-confined

RCLEDs. IR-RCLEDs with a 490-MHz modulation speed have been reported in 1996[32].

Milestones of vertical-cavity light emitters are listed below (Table 1-1).

Table 1-1. *Milestones of vertical-cavity light emitters.*

Year	Milestone
1962	Semiconductor laser[1,2,33]
1965	Perpendicular laser emission[34]
1973	Non-resonant LED[35]
1977	Light-emitting diode by MBE[36]
1979	Optically pumped VCSEL[3]
1984	Electrically injected VCSEL[37]
1985	CW red edge-emitting laser[38]
1986	AlGaInP QW laser[39]
1987	Electrically injected CW VCSEL[40]
1987	Deep-red (760 – 780 nm) photopumped VCSEL[41]
1989	Electrically injected low-threshold CW VCSEL at RT[4]
1991	Deep-red electrically injected VCSEL[42]
1992	RCLED[20]
1992	Red optically pumped VCSEL[43]
1993	Red electrically injected VCSEL[12,44]
1993	Low-temperature (-25 °C) CW AlGaInP VCSEL[45]
1993	CW RT red VCSEL[12]
1993	Red RCLED[21]
1996	GSMBE-grown red RCLED[46]
1997	SSMBE-grown red RCLED[47]
2000	MBE-grown red VCSEL[48]

Metalorganic chemical vapor deposition, MOCVD (also called metalorganic vapor phase epitaxy, MOVPE) has been the dominant growth method when manufacturing vertical-cavity emitters, in particular, in the red wavelength range. However, MBE has been developed for growth of P-containing devices on the red, too, and is used in this Thesis and other papers for growth of red-light components.

1.2 VCSEL and RCLED geometries

The VCSELs have many advantages over their edge-emitting counterparts. The optical field distribution is circular with a small divergence angle and no astigmatism. Such a light beam is much easier to focus or collimate and couple into an optical fibre than a non-circular beam produced from EELs. A very small active volume of VCSEL enables orders of magnitude lower threshold current to be achieved compared to the thresholds of EELs. Due to their geometry, mirror damages are minimised in VCSELs. The mirrors of EELs suffer from catastrophic optical damage (COD), which does not occur in VCSELs.

The structure of an RCLED is similar to that of a VCSEL. However, design tolerances are relaxed, because the reflectivities of the top (output) and bottom mirrors are relatively low (~40-90 % and >90 %, respectively), and cavity-gain adjustment allows for bigger tolerance than what is possible with VCSELs.

Figure 1-1 shows schematically several types of vertical-cavity emitters that have been introduced and investigated in recent years. The general structure is always the same: an active region is sandwiched in between two reflectors. The structures vary in details, *e.g*., the way the current and optical field are confined. Like in edge-emitting lasers, two main mechanisms for lateral light confinement are used, namely gain-guiding and index-guiding. The former confinement mechanism is due to lateral gain variations. In these structures, thermal lensing effects[49] and spatial hole burning significantly affect the transverse mode behaviour. The index-guiding mechanism is due to lateral refractive index variations that confine the optical mode. Real structures are usually a combination of these two lateral confinement methods. *Air-post design* [Figure 1-1a)] is a typical example of index-guiding devices whose lateral dimensions are defined by etching a mesa structure. The refractive index contrast between surrounding air (n = 1) and semiconductor material ($n \sim 3$) provides good optical confinement, while an etched mesa provides a restricted current path. However, usually the sidewalls of a mesa are not smooth, which causes optical losses. Regrowth improves the situation. *Regrown design* is shown in Figure 1-1b), representing a buried index-guided structure. *Proton-implanted design* in Figure 1-1c) is a typical gain-guided structure. The proton-implantation (~350 keV) causes structural defects forming a buried semi-insulating layer. The current confinement is, however, somewhat limited in this case because the implantation can damage the active region, too. Furthermore, implantation does not provide any optical waveguiding, except for the thermal lensing effect. An advantage of proton implantation is the planar structure that allows for most straightforward fabrication.

Oxide-confined design [Figure 1-1d)] is an example of index-guiding. It takes the advantage of highly selective oxidation of Al-containing alloys and a resultant reduction in refractive index when the Al-oxide is formed ($n \cong 1.55$ for Al_2O_3). In GaAs-based structures, the oxidation rate is the highest for AlAs and $Al_xGa_{1-x}As$ with x > 0.98, while a smaller Al-content AlGaAs does not oxidise effectively. A partially oxidised Al(Ga)As layer forms an efficient current aperture that can be placed close to the active region for the best effect, providing strong current confinement. Optical losses can be minimised if the mesa is made bigger than the actual current aperture and if the location, shape, and thickness of the oxide aperture are optimised. Very promising results have been obtained using a thin oxide aperture, which is placed in the node position of the extended standing-wave pattern close to the VCSEL cavity[50] or using tapered oxide apertures[51]. Wet thermal oxidation[52] is the most used process to prepare selective native oxides in Al-containing VCSELs. Wet thermal oxidation has been studied extensively for more than 10 years and its reaction kinetics and properties are now well known[53]. The remaining partly unsolved problems include non-uniformity in Al concentration of the layer to be oxidised, which causes variations in oxidation rate, and reduced layer thickness upon oxidisation (12-13 % for AlAs and 6–7 % for $Al_{0.97}Ga_{0.03}As$)[54,55]. These compositional variations cause additional strain in the structure, sometimes leading to filamentation of the mesa.

In the *intra-cavity contacted design* [Figure 1-1e)] the current is bypassing the most of the mirror layers, enabling a usage of dielectric or other non-conductive reflectors. Furthermore, it is possible to place a tunnel diode inside the structure, which makes it possible to employ *n*-type (or *p*-type) DBRs on both sides of the cavity. Despite some patent-related issues and difficulties in scaling to mass production, oxide-confined VCSELs are gaining ground in commercial markets[56] relative to more conventional ion implantation. The oxidised VCSELs exhibit equal or even better output characteristics and reliability than their implanted counterparts. The latest state-of-the-art emitters employ a combination of these two confinement methods[57] [Figure 1-1f)].

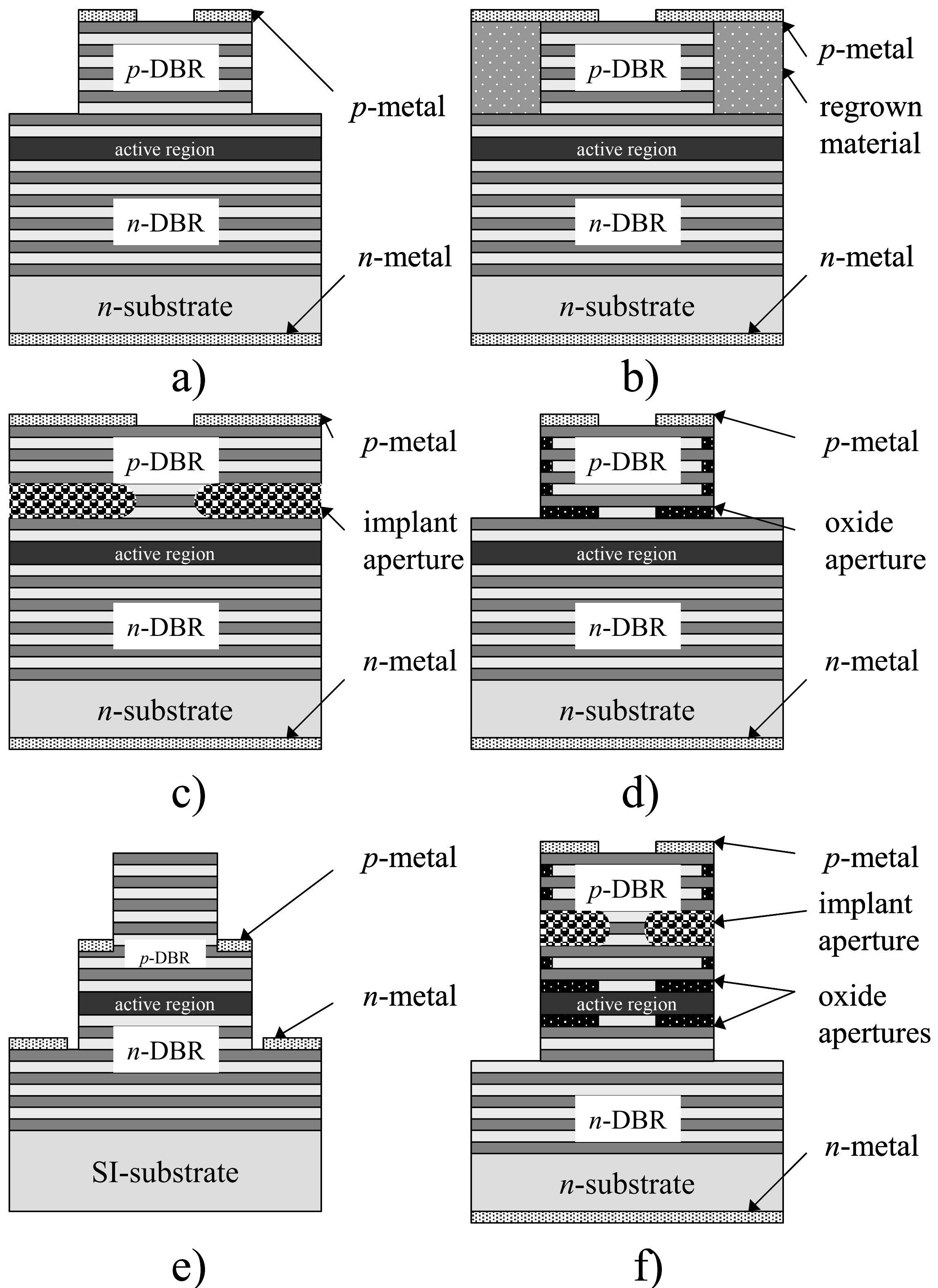

Figure 1-1. *Vertical-cavity light emitter structures. a) airpost, b) regrown, c) proton-implanted, d) oxide-confined, e) intra-cavity contacted, f) implanted and oxide-confined structures.*

Figure 1-2 illustrates a difference between surface-emitting and bottom-emitting structures. The bottom-emitting design is possible when the substrate is non-

absorbing. The bottom-emitting structure can be modified by etching an etched-well structure, which facilitates regrowth by which a new DBR stack into the etch-well can be deposited.

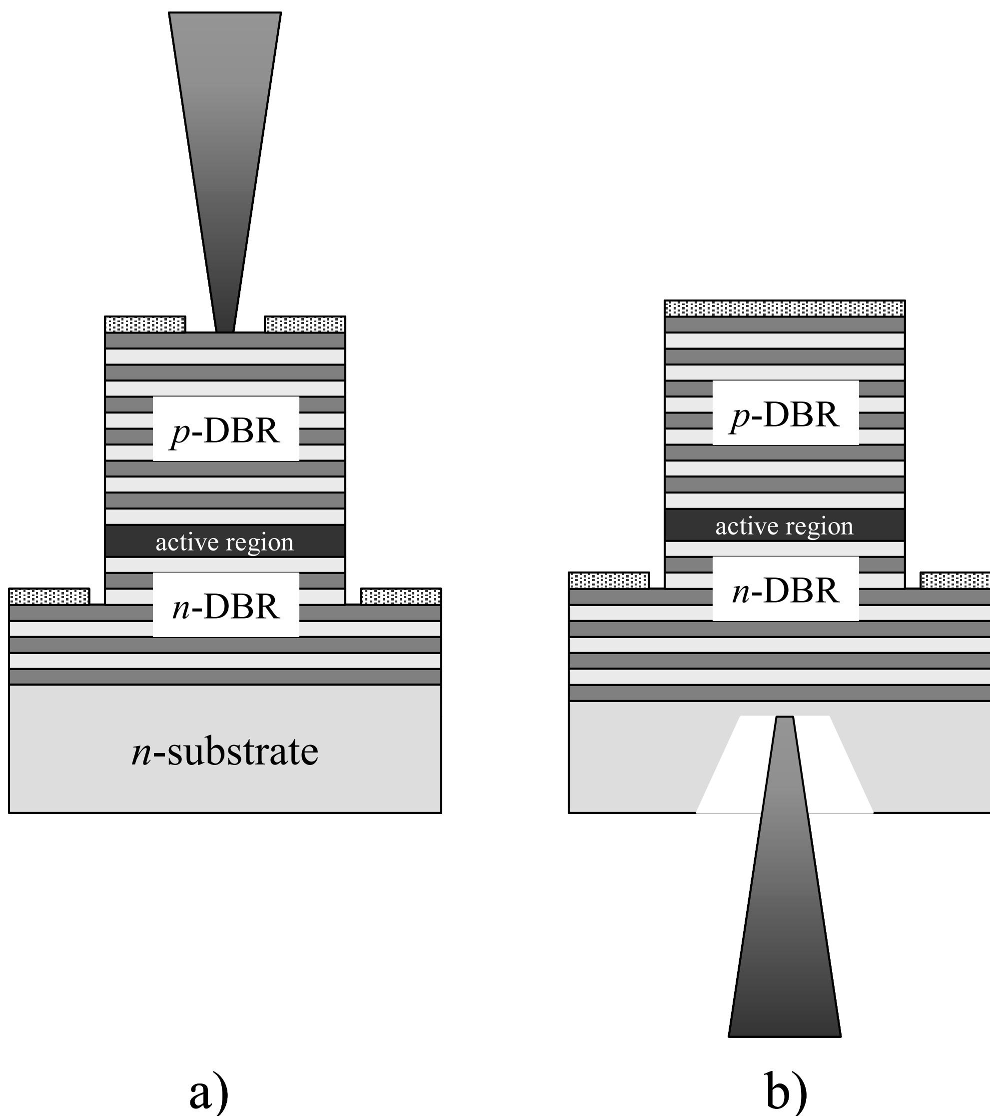

Figure 1-2. *a) Top-emitting and b) bottom-emitting structures.*

Vertical-cavity emitters offer a possibility of manufacturing 2-dimensional arrays. They also allow for on-wafer testing, because the cavity is formed during growth. Therefore, the wafer can be tested before starting device processing.

There are many non-destructive methods to characterise on-wafer VCSELs: X-ray diffraction (XRD), photoluminescence (PL), reflectivity measurement, and photomodulated reflectivity (PR) methods, to name a few. These methods will be introduced in Chapter 3 of this Thesis.

Recently, new LED designs improving the extraction efficiency (η_{ext}) have been presented. They include non-resonant cavity LEDs at λ = 875 nm having an external quantum efficiency (η_e) as high as 31 %. The enhanced efficiency has been achieved

using a roughened component surface, which reduces optical losses at the semiconductor/air interface[58]. The highest $\eta_e \approx 55$ % at 650 nm has been demonstrated using a so-called truncated-inverted-pyramid structure. In this TIP-LED the average free path of photons inside the crystal is minimised to decrease internal losses[59]. The sidewalls are cut to an angle to enhance total reflection from the walls, thus increasing η_e through the top window. Schematic structures of these components are shown in Figure 1-3. The latest LED designs rely on hemispheres[60], which yield optimal coupling into optical fibres[61] or they rely on glass balls that enhance output power.

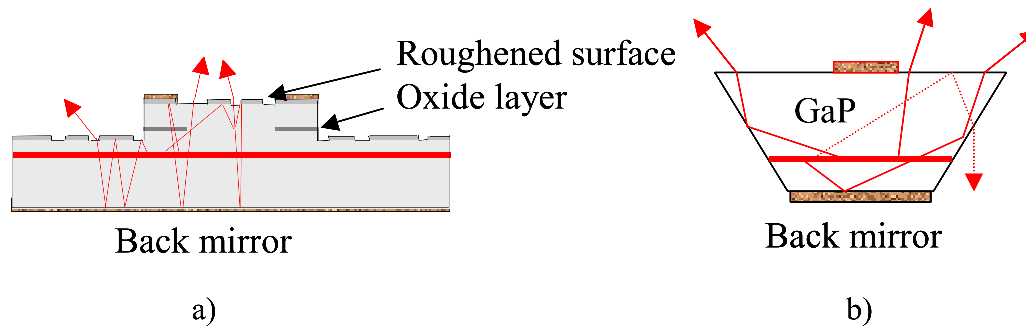

Figure 1-3. *Schematic structures of a) non-resonant cavity LED[58], b) truncated-inverted-pyramid LED[59].*

1.3 Material system

The material system used in the semiconductor emitter design not only determines the emission wavelength and other performance features but also influences device fabrication steps. Several alternatives of III-V (and II-VI) semiconductor materials have been shown to be suitable for surface emitters[62]. A direct bandgap in gain layers and closely lattice-matched composition to achieve high enough crystal quality are prerequisites. The material system employed in this Thesis is AlGaAs/AlGaInP/GaInP, which is deposited onto GaAs substrates. AlGaAs is used in DBR layers, too. $Al_xGa_{1-x}As$ has a direct bandgap, but at higher Al contents ($x >$ ~0.40) it turns indirect. We have used AlGaInP as barriers in the active region and GaInP in the quantum wells. Compressive (< 0.90 %) biaxial strain is applied to the quantum wells.

Heterostructure parameters are compiled in Table 1-2 for GaInAs/AlGaAs on the IR and GaInP/AlGaInP on the red. AlGaInP has high thermal resistivity, which causes heating problems resulting in internal temperature rise (up to 100 °C). Carrier leakage from the Γ point of the Brillouin zone to the indirect X-valley is a severe problem in $Al_xGa_{1-x}As$. AlGaInP heterostructures suffer from small quantum confinement potentials for electrons and holes[63], high effective masses, considerable electrical resistance, and low modal gain[64]. Carrier leakage accounts for ~20 % of the total threshold current (I_{th}) of a red-emitting laser at room temperature, rising to ~70 % of I_{th} at 80 °C[65]. The As-P interface, formed between the cavity and the DBRs, is a problem, too, because it leads to reversed valence band discontinuities[66].

The conduction and valence band edges for AlGaAs, AlGaInP and AlAsP are illustrated in Figure 1-4, and the band offsets between AlGaAs and AlGaInP are shown in Figure 1-5. It can be seen that the AlGaInP/AlGaAs interfaces between the DBR and the cavity are critical. In these plots, the direct-indirect bandgap cross-over compositions differ slightly: Y = 0.50[67] against Y = 0.66[68] in $(Al_YGa_{1-Y})_{0.50}In_{0.50}P$ in Figures 1-4 and 1-5, respectively. There has been some debate about the correct value of Y. An incomplete group-V switchover as well as In segregation[69] at the interface can lead to the formation of rough interfaces and other structural defects.

Table 1-2. *GaInAs/AlGaAs versus GaInP/AlGaInP lattice-matched (LM) and strained quantum well (SQW) heterostructure properties*[67].

Parameter	***$Ga_{1-x}In_xAs$ / $Al_{0.4}Ga_{0.6}As$***	***$Ga_{1-x}In_xP$ / $(Al_{0.5}Ga_{0.5})_{0.51}In_{0.49}P$***	***Impact on red-emitting device***
ΔE_c (meV)	350 @ x = 0 (LM) 480 @ x = 0.2 (SQW)	165 @ x = 0.5 (LM) 225 @ x = 0.6 (SQW)	Leakage, thermal sensitivity → low T_0
ΔE_v (meV)	220 @ x = 0 (LM) 290 @ x = 0.2 (SQW)	110 @ x = 0.5 (LM) 150 @ x = 0.6 (SQW)	Leakage, thermal sensitivity → low T_0
m_e^*/m_e	0.067 (GaAs)	0.11 (GaInP)	Higher J_{th}
m_{hh}^*	0.45 (GaAs)	0.62 (GaInP)	Higher J_{th}
σ (electrical)	Good for electrons and holes	Good for electrons, poor for holes	Leakage, heating effects
ρ (thermal) (cm °C/W)	2-10	>19	Heating effects
Peak gain @ 300 K (cm^{-1})	67 (@ 4 x 10^{12} cm^{-2})	17 (@ 4 x 10^{12} cm^{-2})	Higher J_{th}
Wavelength range (nm)	800 - 1000	620 – 700	

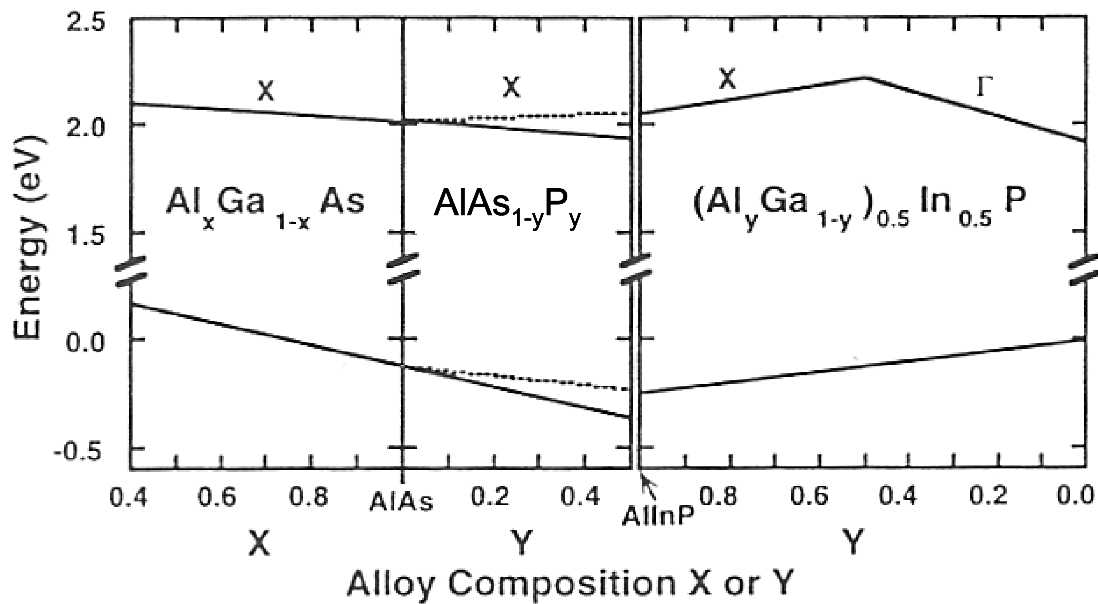

Figure 1-4. *Dependence of the conduction and valence band edges of $Al_xGa_{1-x}As$, $(Al_yGa_{1-y})_{0.5}In_{0.5}P$ and $AlAs_{1-y}P_y$ on alloy compositions X and Y*[67] *(reproduced by permission of World Scientific Publishing Ltd).*

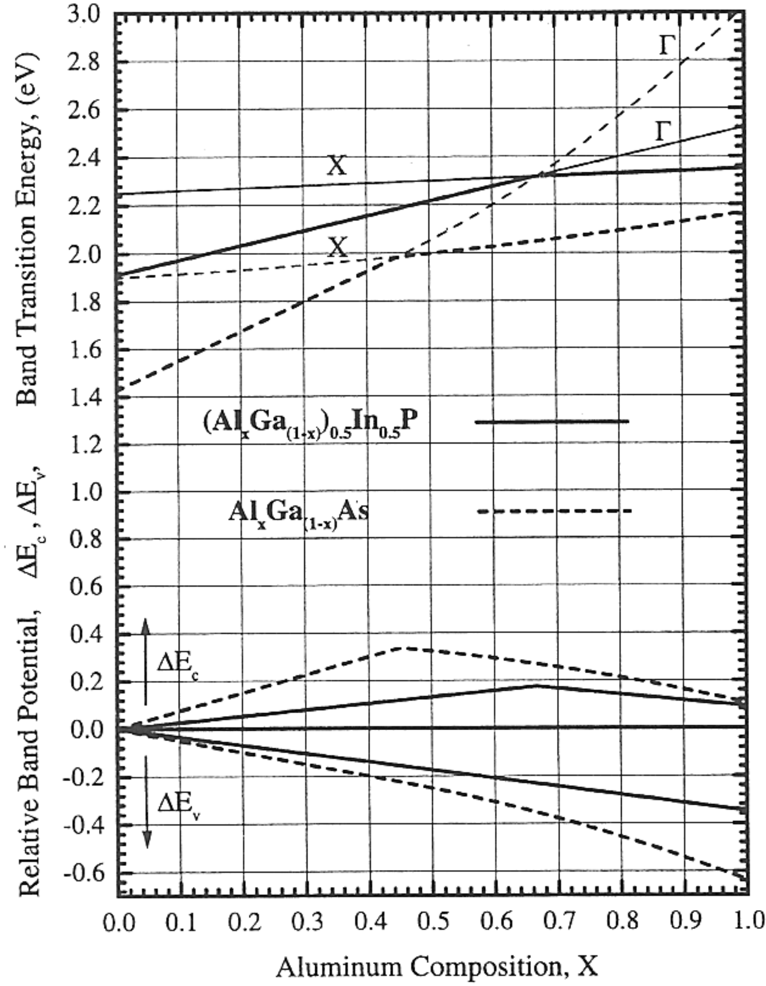

Figure 1-5. *Bandgaps and band-offsets for the AlGaAs and AlGaInP material plotted against Al composition. ΔE_c and ΔE_v refer to the conduction and valence band offsets, respectively, and E_Γ and E_X are the energy gaps with respect to the Γ and X conduction band minima, respectively*[68] *(reproduced by permission of Cambridge University Press).*

Under certain growth conditions AlGaInP tends to order spontaneously in the group-III $(GaP)_p(InP)_p$ sublattice[70]. Ordering increases the emission wavelength, reduces the optical efficiency by inhomogeneous broadening of the gain spectrum and degrades the crystal quality[71]. The most favoured ordering type is $(GaP)_p(InP)_p$ CuPt-like ordering with p = 1 and sublattice direction **G** = <111>. Other types of ordering are CuAu (p = 1, **G** = <001>) and Chalcopyrite (p = 2, **G** = <201>), but they are rare because they require very special growth conditions[72] to be formed. Higher growth temperatures[73], optimised III/V -ratio[74] and offcut (about 6-10°) substrates[75] have solved most of the ordering problems in MOCVD growth. MBE has by its nature a lower ordering tendency in AlGaInP[76], which has been confirmed by our experiments[77]. The ordering effects are particularly severe for vertical emitters because thickness of the optical cavity is usually 1-2 optical waves (λ_0/n) only, 200-600 nm, resulting in very small gain per pass. These pitfalls set stringent requirements on the DBR design, optical efficiency, and energy band engineering.

P-type doping of $Al_xGa_yIn_{1-x-y}P$ with high x is hard. Zn has been the most used dopant material (in MOCVD), but the number of activated acceptors remains quite low (~5 x 10^{17} cm^{-3})[78]. C is an extremely stable and controllable dopant in AlGaAs, but it is ineffective in AlGaInP. Mg can also be used, but it is difficult to control and its consumption is high[79]. Be is the most common *p*-dopant in MBE. Be has an ability to diffuse inside the structure, which may cause problems especially in the vicinity of the active region[80]. All these problems, hard to be avoided by any technique, suggest to us that the amount of *p*-type doped AlGaInP should be as small as possible in the device structures.

2. Emission characteristics

In this Chapter emission properties of RCLEDs and VCSELs will be presented. The Chapter is concluded by a discussion on plastic optical fibres and their use for optical data transmission in the visible spectral range.

2.1 RCLEDs

A drawback of conventional LEDs is a poor extraction efficiency, $\eta_{ext} \approx 2$ %, due to reflection losses in the semiconductor / air interface. One way to improve the extraction efficiency is to use a semiconductor microcavity[81]. A Fabry-Perot (F-P) microcavity is formed by placing an optically active region, the thickness (L) of which is about the same as the operation wavelength ($nL \approx \lambda$), between two parallel mirrors. This cavity is known to enhance spontaneous emission of the active region according to the theory of the cavity quantum electrodynamics (CQED). Certain emission angles are in resonance with the quantum well excitons enhancing emission by a factor determined by the cavity finesse. This cavity effect improves spectral power density, spectral purity, and modulation frequency.

2.1.1 Microcavity effects

Electronic confinement in low dimensional structures has been widely used to tailor materials to improve their optical and electrical properties. In bulk semiconductors, radiative recombination can occur over a wide range of momentum (**k**) states, which together with a thermal distribution of the carriers at room temperature result in broad emission bands. By confining electrons and holes in structures with reduced spatial dimensions the energy levels become quantised. The goal of electronic confinement is to make discrete atomic-like energy levels with energy separation much greater than kT (~ 26 meV at room temperature). *Optical confinement* is used to guide photons to desired areas of the structure. This can be achieved by using refractive index steps, microcavities or photonic bandgap structures. If the active material is placed in an optical cavity where only a single photon mode has a spectral overlap with the emission band, then radiative recombination can only take place in that photon mode. The emitted light has the spectral characteristics of the photon mode.

The confinement can be in 3, 2 or 1 dimensions. In this Thesis we consider carrier and photon confinement in one dimension. The de Broglie –wavelengths of carriers and photons indicate the order of magnitude of the physical dimensions needed for confinement.

The photon-matter interaction has two regimes: weak coupling and strong coupling. In the *weak coupling,* on which we concentrate in this Thesis, the photons are weakly coupled to the electronic states of the active medium. The energy of the allowed

optical modes does not influence the energy of the electronics states, but the free carrier recombination in the active medium takes on the spectral characteristics of the optical mode. The width of the emission spectrum can be narrower than in free space because it is determined by a long photon lifetime in the microcavity. Consequently, the spontaneous emission rate, inversely proportional to lifetime, is altered. It can be either enhanced or inhibited[82].

In *strong coupling*, instead, the coupling between the allowed cavity mode and an atomic-like transition in the active medium is so strong that the energy of atomic transitions and the energy of the allowed optical mode are no longer independent but are coupled. This coupling leads to a splitting of the energy levels into a doublet, called a Rabi-splitting[83]. In the strong coupling regime, the perturbation theory is no longer valid. Coherent behaviour of single atoms interacting with a single photon mode leads to vacuum-field Rabi oscillations[84], which have been observed experimentally in vertical-cavity semiconductor structures.

In semiconductor microcavities, the equivalent of both photon and atomic oscillators can be found. A planar Fabry-Perot (F-P) cavity utilising DBRs can be used for the photon mode selection, and therefore the excitons, the bound states of electrons and holes, have sharp atomic-like excitations. The coupled modes of exciton and the vacuum field are called polaritons. In order to achieve a strong coupling, high-Q cavities are needed. However, in vertical-cavity emitters at room temperature, free carrier recombination rather than exciton recombination always seems to dominate.

Spontaneous emission is the main recombination process in high-quality RCLEDs. This emission can be modified quite significantly by microcavity effects, which may affect the radiative transition rate, spectral purity, far-field emission pattern, and coherence properties (coherence is discussed in Section 4.1.1). A microcavity alters the zero point field, changing the matrix element of an electric dipole transition between the conduction and valence band. This change can be calculated assuming that the zero field inside the cavity is the sum of parts of the zero field outside that are penetrating through the mirrors and are circulating inside of the cavity[85]. Mathematically the spontaneous emission rate can be expressed using Fermi's golden rule[85]

$$W_{em} = \frac{2\pi}{\hbar^2} \langle u | \mathbf{d} \cdot \mathbf{E} | l \rangle^2 \rho(\omega) \tag{2.1}$$

where **d** is a dipole momentum operator, **E** is an electric field operator and $\rho(\omega)$ is the density of photon modes. In the matrix element, u corresponds to the upper energy level and l corresponds to the lower energy level.

In the following, we use the symbols:

λ	*wavelength detected outside the emitter*
λ_{qw}	*QW emission wavelength in a semiconductor*
λ_c	*optical cavity length (= nL)*
λ_o	*center wavelength of a DBR ($\lambda_o \approx \lambda_{qw}$)*
λ_{det}	*cavity detuning*

d	*thickness of the active region*
G_e	*emission mode density enhancement factor*
L	*cavity length*
L_{eff}	*effective cavity length*
L_p	*penetration depth to the DBR*
θ	*emission angle*
θ_c	*critical angle*
θ_{max}	*angle of maximum emission intensity*
ν	*frequency*
ω	*angular frequency*
W	*emission rate*

The average spontaneous emission rate calculated for free space is[85]

$$W_{em0} = \frac{2\omega^3 d_0^2}{3\pi\hbar\varepsilon_0 c^3}, \tag{2.2}$$

where d_0^2 is the total dipole moment coupling strength and ε_0 is relative permittivity of the vacuum. In a microcavity, the emission rate is different[85]:

$$W_{em} = \frac{3W_{em0}}{4}\int_0^{\pi/2} d\theta \sin\theta \frac{(1-R)\left[1+R-2\sqrt{R}\cos(kL\cos\theta)\right]\left[1+\cos^2\theta\right]}{(1-R)^2+4R\sin^2(kL\cos\theta)}. \tag{2.3}$$

Here R is the reflection coefficient of the mirrors ($R_1 = R_2 = R$ for identical mirrors) and L is the cavity length. θ is the emission angle and $k = 2\pi/\lambda_{qw}$ is the wave vector. Assuming that R is close to the unity, Eq. (2.3) approaches a sum[85]

$$W_{em} = \frac{3W_{em0}}{4}\frac{2\pi}{kL}\sum_{m=1}^{\mathrm{int}(kL/\pi)}\frac{1-(-1)^m}{2}\left(1+\left(\frac{m\pi}{kL}\right)^2\right), \tag{2.4}$$

where int(x) is the largest integer smaller or equal to x. At the upper limit, when $L\rightarrow\infty$, the value of the sum approaches to the free space case (Eq. 2.2). When the optical cavity length $\lambda_c = nL$ is approximately equal to one half of emission wavelength λ_{qw} of the source inside the cavity, a three-fold improvement of the free space emission rate is obtained for $R = 1$[85]. However, the improvement is significantly less for a real RCLED with DBR mirrors. Besides the field penetration into the DBR mirrors, which lowers W_{em}, the angle- and λ-dependent reflectivity leads to leaky modes that do not experience any cavity effects. Since W_{em} is calculated by integrating over all emission directions, the leaky modes reduce cavity enhancement[86]. Only about 20 % enhancement in W_{em} has been observed experimentally for a cavity with AlAs/GaAs Bragg reflectors[87].

Though cavity enhancement has a minor effect on W_{em}, and thus on the modulation bandwidth, the distribution of the optical mode density $\rho(\omega)$ in Eq. (2.1) is strongly modified[32]. The emission mode density enhancement factor (G_e) at the resonance wavelength can also be expressed by the ratio of the optical mode densities with and

without a cavity. The optical mode structure of the cavity is defined by the Airy function[88]

$$A(\phi) = \frac{2T_1}{\left|1 - r_1 r_2 e^{i2\phi}\right|^2}. \tag{2.5}$$

$A(\phi)$ determines in a complex plane, which angles are enhanced and which are inhibited. Here 2ϕ (= $\frac{4\pi nL}{\lambda}\cos\theta$) is a round-trip-phase, T_1 is a mirror transmission coefficient, r_1 and r_2 are reflectivity amplitudes of the mirrors, $|r_1|^2 = R_1, |r_2|^2 = R_2$. $A(\phi)$ is a periodic function with resonance peaks defined by the round-trip phase 2ϕ of the cavity mode. The width of resonance peaks is inversely proportional to the finesse (F) of the cavity, which, in turn, is a function of R_1 and R_2[88]:

$$A(\phi) = \frac{1 - R_1}{\left(1 - \sqrt{R_1 R_2}\right)^2} \frac{1}{1 + F\sin^2\phi}, \tag{2.6}$$

$$F = \frac{4\sqrt{R_1 R_2}}{\left(1 - R_1 R_2\right)^2}. \tag{2.7}$$

For the constructive interference, 2ϕ should be a multiple of 2π. This means that different wavelengths are favouring different angles for the cavity resonance. This phenomenon will be later discussed in greater detail.

A similar presentation can be introduced in the wavelength or angular frequency ($\omega = 2\pi\nu$) domain, which thus gives the distribution of the optical mode density $\rho(\omega)$.

The cavity finesse (F) can also be calculated in the frequency domain ($\nu = \omega / 2\pi$) using the optical mode density [$\rho(\omega)$ or $\rho(\nu)$] peak separation, called a free spectral range (ν_{FSR}), and the width of half maximum ($\Delta\nu$) of the mode density peak:

$$F = \frac{\nu_{FSR}}{\Delta\nu}. \tag{2.8}$$

Figure 2-1 illustrates an example of $\rho(\nu)$ of a one-dimensional planar microcavity compared to a homogeneous one-dimensional free-space optical mode density. G_e is given by the ratio of the maximum optical mode densities with and without the cavity.

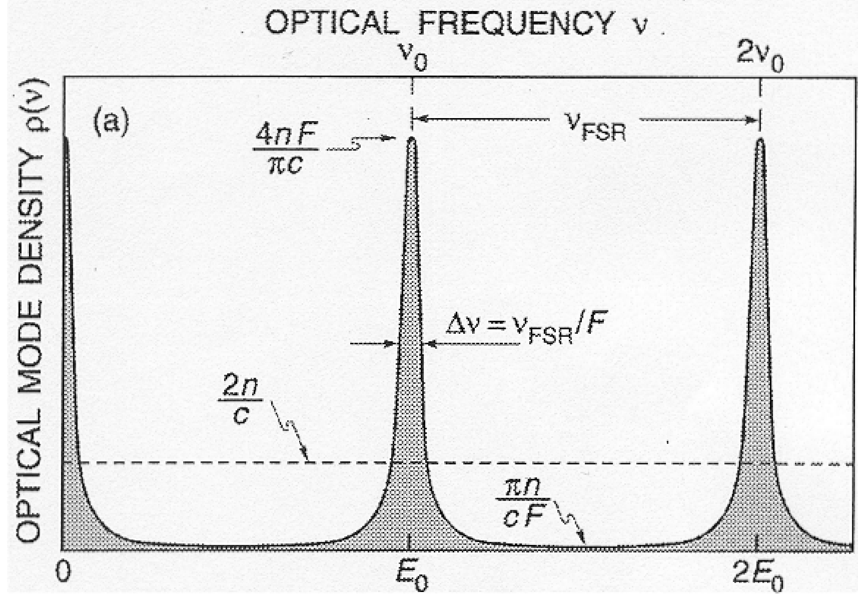

Figure 2-1. *Optical mode density of an one-dimensional planar microcavity (solid line) and of a homogeneous one-dimensional free-space (broken line). 4nF/πc and πn/cF are the calculated maximum and minimum values of ρ(ν), respectively*[89] *(reproduced by permission of Cambridge University Press).*

At the resonant wavelength outside the cavity with mirror reflectivities $R_1 < R_2$ we obtain G_e for a real microcavity (at $\theta = 0°$)[89]:

$$G_e = \xi \frac{(R_1 R_2)^{1/4}(1 - R_1)}{\left(1 - \sqrt{R_1 R_2}\right)^2} \frac{\tau_{cav}}{\tau}, \tag{2.9}$$

where the standing-wave effect and shortening of spontaneous emission lifetime in the cavity have been taken into account. ξ is an antinode enhancement factor, which has a value of 2, if the active region is located exactly at an antinode of the standing wave inside the cavity, and ξ = 0, if the active layer is located at a node. τ is the lifetime of photons in free space and τ_{cav} is the lifetime in the cavity. However, as mentioned above, the emission lifetime is reduced usually about 10-20 % or even less in planar microcavities[90], so this factor does not play an important role in determining G_e.

In many practical devices, it is more interesting to determine the total enhancement factor G_{int} obtained by integrating over all wavelengths rather than considering G_e at a given resonance wavelength. Assuming a Gaussian emission spectrum, the integrated enhancement ratio (or suppression ratio) is given by[91]

$$G_{\text{int}} = G_e \sqrt{\pi \ln 2} \frac{\Delta\lambda}{\Delta\lambda_n}, \tag{2.10}$$

where $\Delta\lambda$ (typically ~5-10 nm) is a cavity resonance bandwidth and $\Delta\lambda_n$ is the natural linewidth (~1.8 kT, ~0.7 kT for quantum wells). It can be seen that if the emission

spectrum is broad, or F is high, G_{int} is suppressed, since only a small part of the spectrum is in resonance.

As a concluding design rule, we may write G_{int} as[32]

$$G_{\text{int}} = \xi \sqrt{\frac{\ln 2}{\pi}} \frac{\lambda_{qw}}{L_{eff}} \frac{\lambda}{\Delta\lambda_n} \frac{2(1-R_1)}{(2-R_1-R_2)} \frac{\tau_{cav}}{\tau}, \tag{2.11}$$

where λ_{qw} is the photon wavelength in the cavity, λ is the wavelength in air, and L_{eff} is the effective cavity length ($L_{eff} = L + L_{p1} + L_{p2}$, where L is the cavity length, L_{p1} and L_{p2} are optical field penetration depths to the DBRs). Eq. (2.11) shows that a small L_{eff} maximises the integrated intensity. For the RCLEDs of this Thesis we have, *e.g.*, λ_{qw} = 645 nm, λ = 655 nm, λ_c = 655 nm, R_1 = 0.55, R_2 = 0.95, L_{eff} = 7 λ_c/n, $\Delta\lambda_n$ = 0.7 kT = 30 nm, ξ = 1.1, τ_{cav}/τ = 1, n = 3.4. Thus we obtain $G_{int} \approx 7$.

The cavity quality factor (Q) is related to F. It is defined as a ratio of transmittance peak frequency to the peak width:

$$Q = \frac{peak\ frequency}{peak\ width} = \frac{2nL_{eff}}{\lambda} F. \tag{2.12}$$

Typically, a top-emitting RCLED has the bottom mirror with reflectivity of $R_2 \approx 99$ %, whereas the top mirror has R_1 between 40 and 90 %. High R_1 (and $R_2 \approx 1$) yields high Q and strong enhancement of certain resonance wavelengths, narrowing resonance peaks. On the other hand, high R_1 also means that non-resonant wavelengths are more effectively inhibited, leading to a lower overall efficiency. Figure 2-2 shows schematically how the Airy function determines the characteristic modes that either amplify or suppress emission.

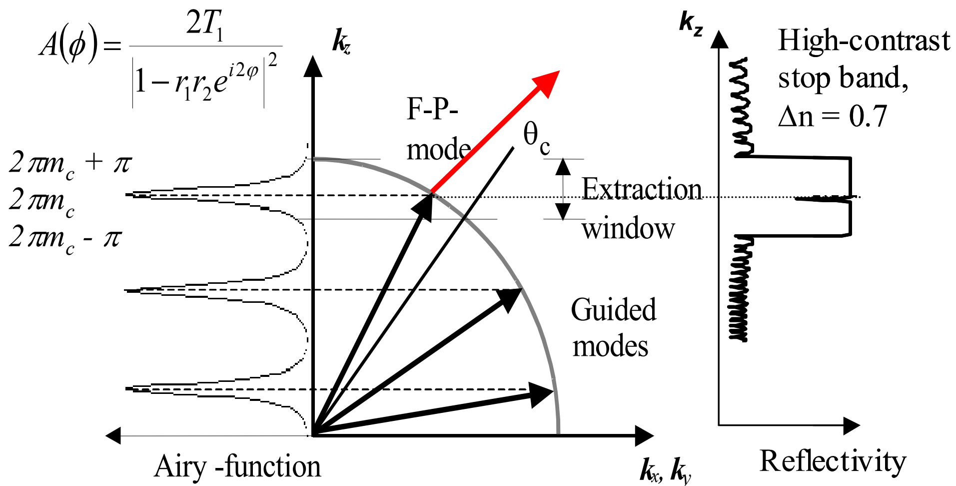

Figure 2-2. *Airy function determines the characteristic mode structure (m_c = 3).*

The number of resonance angles is given by the cavity order m_c and it is proportional to the cavity length L ($m_c = 2Ln/\lambda_c$)[92]. The extraction efficiency of an ideal RCLED with a monochromatic source is approximately $\eta_{ext} \approx 1/m_c$ and thus in order to have the highest possible η_{ext}, m_c should be as small as possible. However, in a real RCLED with relatively small Δn ($\approx$ 0.5-0.7) between the first DBR layer and the cavity material, reflection takes place at successive interfaces making L_{eff} long. According to the theory, small Δn increases m_c, so there will be more wavelength-angle pairs to fulfil the resonance conditions. However, a limited width of the DBR stopband enhances only those modes that overlap with the stopband (see Figure 2-2).

Another important factor determining η_{ext} is the cavity detuning, λ_{det}. It is defined as a difference between the cavity F-P resonance wavelength (λ_c) at normal incidence and the peak-emission wavelength of the quantum wells (λ_{qw}): $\lambda_{\mathrm{det}} = \lambda_c - \lambda_{qw}$. A positively detuned RCLED ($\lambda_{det} > 0$) has a higher efficiency than an RCLED with $\lambda_{det} \leq 0$ nm since the cavity mode(s) and the gain spectrum of the quantum wells are more overlapped. A positive detuning leads to a two-lobed far-field pattern with maximum intensities at off-normal polar angles ($\pm\theta_{max}$)[93]. The detuning factor can be calculated approximately from the equation

$$\lambda_{\mathrm{det}} \approx \lambda_{qw} \left(\frac{1}{\sqrt{1 - \frac{n_o^2}{n_{high}^2} \sin^2 \theta_{\mathrm{max}}}} - 1 \right) . \tag{2.13}$$

Here n_o and n_{high} are the refractive indices of the output medium and of the low-bandgap layer of the DBR, respectively. It can be seen from Figure 2-2 that $|\theta_{max}|$ of the F-P mode lies between 0° and θ_c. Modes oscillating at angles $\theta > \theta_c$ are not F-P modes and they cannot exit from the cavity via the emission window. However, they can be guided modes or inhibited modes.

In addition to the coupling of the cavity mode with QW emission, microcavity structures may have two cavities for coupling between two optical modes. The cavities are separated by a DBR mirror and the structure can comprise two *pn*-junctions allowing electrical pumping, and the cavities can be active or passive. Multisection VCSELs are also called BiVCSELs[94] or coupled resonator vertical-cavity lasers (CRVCLs). Coupling between the cavities depends on the middle-mirror reflectivity. When the coupling is strong, the modes are shifted to either side of the resonance wavelength. When the QWs are exactly in resonance with one of the cavity modes, it is possible to detect a third oscillator originated from quantum well excitons. The coupled cavity design can be exploited in special applications, like wavelength multiplexing, short pulse generation by *Q*-switching[95], terahertz frequency generation[96], bistable lasers[97], dual wavelength interferometry and high-power single-mode VCSELs[98]. These rather new applications cannot fully utilise the BiVCSELs yet, due to the problems related to complex fabrication steps of BiVCSELs and a lack of precise mode control.

2.1.2 Figures of merit

The figures of merit describe the capabilities of the devices and allow for the comparison of the devices with each other. They can be also used for control of production. Output power, series resistance, differential resistance, modulation speed, brightness, and efficiencies are the most studied figures of merit. Typical efficiencies of vertical cavity emitters are given in Table 2-1. External quantum efficiency (η_e) can be expressed in terms of η_{ext}, internal quantum efficiency (η_i), and injection efficiency (η_{inj}):

$$\eta_e = \eta_{ext}\eta_i\eta_{inj} \,. \tag{2.14}$$

The external quantum efficiency is a measure of how many photons are generated by the injected electrons and emitted into a medium. η_{ext} describes, how much of light generated in the active region fits in the critical angle and is extracted from the component. η_i gives the portion of the radiative recombination of the total recombination. η_{inj} describes how much of injected carriers are recombining within the active region. η_{inj} can be determined from the measured spontaneous emission spectra just below the threshold and the above-threshold slope efficiency of the semiconductor laser.

Table 2-1. *Definitions of various light / matter interaction efficiencies.*

Symbol	*Figure of merit*	*Formula*	*Notes*
η_{wp}	Wall-plug efficiency	$\frac{P_{opt}}{IV}$	P_{opt} optical power I current V voltage
η_e	External quantum efficiency	$\frac{P_{opt}/h\nu}{I/q}$	h Planck's constant ν frequency q elementary charge
η_{ext}	Extraction efficiency	$\frac{1}{1+\bar{\alpha}x_j/\bar{T}}$	$\bar{\alpha}$ average absorption coefficient x_j junction depth $\bar{T}$ light power which is extracted within the critical angle
η_i	Internal quantum efficiency	$\frac{1}{1+\tau_r/\tau_{nr}}$	τ_r radiative time constant τ_{nr} nonradiative time constant
η_{inj}	Injection efficiency	$\frac{I_n}{I_n+I_p+I_r}$	I_n electron current I_p hole current I_r radiative current

2.1.3 Emission pattern and fibre coupling

As noted above, for the constructive interference in the cavity, the round-trip-phase must be a multiple of 2π. This interference means that different wavelengths are favouring different angles for the cavity resonance. The longest extracted wavelength, corresponding to the longitudinal F-P mode, is emitted perpendicular to the grown

layers and shorter wavelengths are emitted at increasingly larger angles relative to the surface normal. As the angular position of the cavity mode changes with wavelength, each wavelength being extracted in a lobe oriented on a different angle[99]. Figure 2-3 presents the calculated emission lobes for (a) $\lambda = 652$ nm, (b) $\lambda = 651.5$ nm, (c) $\lambda = 650.5$ nm, (d) $\lambda = 648.5$ nm, (e) $\lambda = 646.5$ nm, (f) $\lambda = 644.5$ nm, (g) $\lambda = 642.5$ nm, (h) $\lambda = 652.5$ nm, (i) $\lambda = 653$ nm, (j) $\lambda = 653.5$ nm, (k) $\lambda = 653.7$ nm and (l) $\lambda = 654.5$ nm in an RCLED with the longitudinal cavity resonance at about 653 nm and the peak λ_{qw} at about 648 nm, thus $\lambda_{det} = 5$ nm.

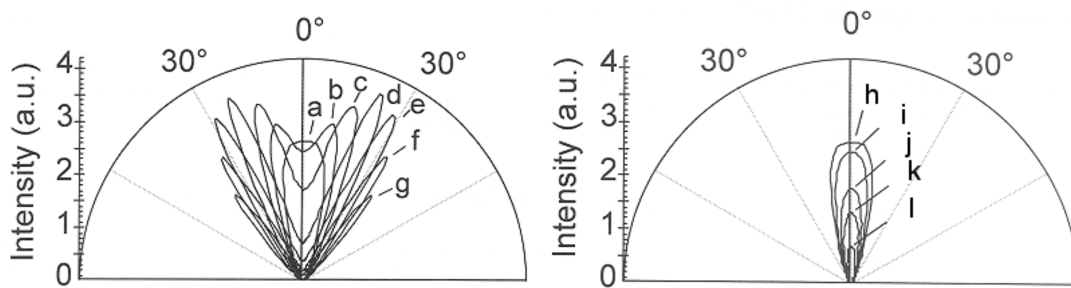

Figure 2-3. *Spectrally resolved angular emission profiles in an RCLED with 5 nm detuning (a) $\lambda = 652$ nm, (b) $\lambda = 651.5$ nm, (c) $\lambda = 650.5$ nm, (d) $\lambda = 648.5$ nm, (e) $\lambda = 646.5$ nm, (f) $\lambda = 644.5$ nm, (g) $\lambda = 642.5$ nm, (h) $\lambda = 652.5$ nm, (i) $\lambda = 653$ nm, (j) $\lambda = 653.5$ nm, (k) $\lambda = 653.7$ nm and (l) $\lambda = 654.5$ nm*[100].

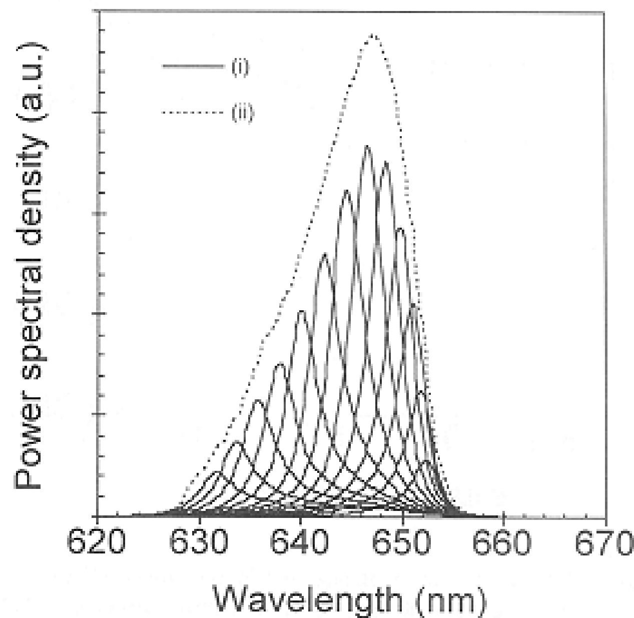

Figure 2-4. *(i) Angular components of Figure 2-2 after scaling (solid line), (ii) measured integrated intensity (dashed line)*[100].

In the spectral domain, as the position of the cavity mode dip changes with θ and since at particular θ only the wavelengths within the dip are extracted, the RCLED emission spectrum varies for different angular directions. Figure 2-4 shows the

emission spectra for a number of different directions for an RCLED of Figure 2-3 with the escape window fitted to the emission spectrum. The angular components were initially collected through a small pinhole of a monochromator and therefore they had to be scaled up by an appropriate factor to obtain the total emitted power. The overall extracted spectrum is obtained by integrating the intensity of the emission spectra for all the angles (corresponding NA =1). In this respect, when collecting the RCLED emission using a fibre, the limited numerical aperture ($0 < NA < 1$) of the fibre not only collects just a fraction of the emitted power but it also collects just a fraction of the emitted spectrum, resulting in small FWHM.

In order to achieve maximum η_{ext}, as much as possible from the emitted spectrum has to be placed inside the RCLED spectral escape window (Figure 2-2), which is limited by the longitudinal F-P resonance wavelength ($\lambda_{max} = \lambda_c$, the long wavelength limit) and by the cavity dip position for the critical angle at the highest contrast interface (roughly $\lambda_{min} = \lambda_c \cdot [1-(n_l/n_h)^2]^{1/2}$, the short wavelength limit, n_l and n_h being the low and high refraction indices at the interface with the highest contrast). Consequently, for high η_{ext}, the longitudinal mode cavity dip has to be detuned to a longer wavelength with respect to the peak λ_{qw}. The amount of this detuning influences both η_{ext} as a certain part of the QW emission fits into the RCLED spectral escape window, and the spectrally integrated far field pattern.

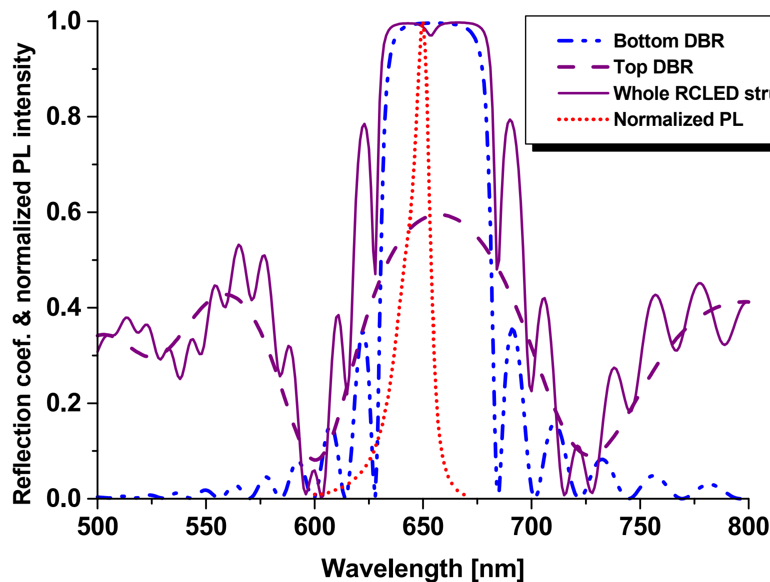

Figure 2-5. *Calculated spectral reflection coefficients for an RCLED structure and DBR mirrors together with a measured PL spectrum.*

Figure 2-5 displays the calculated spectral reflection coefficient (reflectivity) for the top DBR mirror, for the bottom DBR mirror, and for the whole RCLED structure at normal incidence in air from the top of the sample together with the measured photoluminescence (PL) spectrum. Actually, the detuning between λ_{qw} and λ_c is greater than apparent in Figure 2-5 since the PL spectrum is slightly red-shifted with respect to the electroluminescence spectrum. It can be seen that while R_2 is close to unity, R_1 is significantly lower so that the cavity modes over the whole emission spectrum occupy as much as possible of the escape window, thus improving η_{ext}.

When the whole emitted spectrum fits inside the escape window two separate emission lobes appear in the XOZ-plane. Then an optimum λ_{det} producing a maximum η_{ext} is roughly equal to the difference between the long wavelength edge and the peak emission wavelength of the spectrum. As λ_{det} is increased above the optimum value the emission lobes separate further apart (decreasing the fibre coupling efficiency η_{couple}) and η_{ext} is decreased, the shorter wavelengths exit the escape window. When λ_{det} is decreased below the optimum value the emission lobes come closer together (increasing η_{couple}) and η_{ext} is reduced, due to long wavelength emission exiting the escape window range. Finally, when $\lambda_{det} = 0$, a highly-directional single-lobe far-field normal to the surface of the device is obtained.

Figure 2-6 shows spectrally aggregated simulated and measured far-field lobes for three 650-nm RCLEDs for which λ_{det} was 0 nm (650RC012), 6 nm (650RC015), and 14 nm (650RC014). It is somewhat unclear to us how much of the disagreement (which is small) between our simulations and measurements is due to the applied model itself and how much is due to differences between the designed and the actual structures.

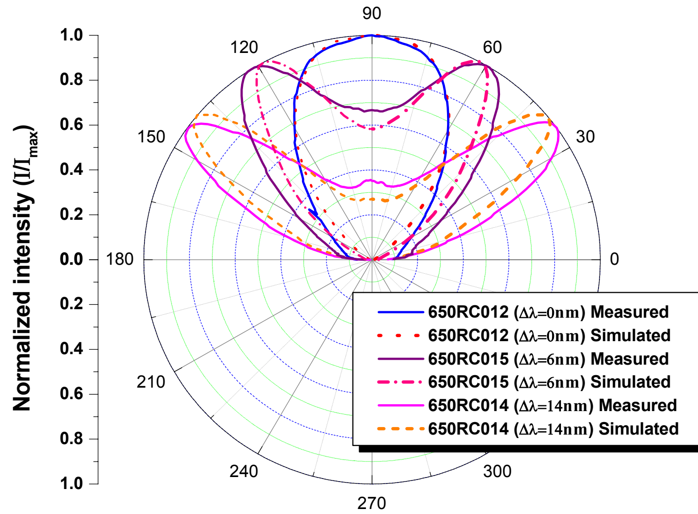

Figure 2-6. *Measured and simulated far-field distributions of three RCLEDs with different detuning factors λ_{det}. λ_{det} = 0 nm (650RC012), 6 nm (650RC015), and 14 nm (650RC014).*

The angle at which the maximum intensity occurs is

$$\theta_{\max} \approx \arcsin\left[\frac{n_{high}}{n_o}\sqrt{1-\left(\frac{\lambda_{qw}}{\lambda_c}\right)^2}\right], \tag{2.15}$$

where n_{high} and n_o are the refractive indices of the low-bandgap layer of the DBR and the output medium (often air, $n_o = 1$), respectively.

2.1.4 Modulation response of RCLED

A fundamental limit of the modulation speed is determined by the spontaneous recombination lifetime of free carriers. Two major factors can influence the modulation bandwidth: the nonradiative recombination lifetime and the carrier density in the active region. The carrier lifetime in quantum well structures is reduced compared to bulk semiconductors due to the larger overlap of the electron and hole wave functions. Consequently, it is expected that the QW-RCLEDs can be modulated at higher speeds than conventional LEDs, which do not consist of QWs. The small signal modulation bandwidth f_{-3dB} is a frequency at which the modulus squared of the normalised *optical* transfer function $H(\omega) = 1/(1 + j\omega\tau_c)$ is reduced by 3 dB. This frequency is related to the carrier lifetime τ_c

$$f_{-3dB} = \frac{1}{2\pi\tau_c} \tag{2.16}$$

where τ_c is

$$\frac{1}{\tau_c} = \frac{1}{\tau_r} + \frac{1}{\tau_{nr}} + \frac{1}{\tau_{leak}} = \frac{1}{\tau_r} + \frac{1}{\tau_{nrl}}. \tag{2.17}$$

Here, τ_{nr} refers to nonradiative recombination within the active region, but particularly for the red-emitting devices with relatively shallow QWs τ_c should also include the carrier leakage from the active region (τ_{leak}), which significantly affects the carrier lifetime and the carrier density. Thus we write in Eq. (2.17) $\frac{1}{\tau_{nr}} + \frac{1}{\tau_{leak}} = \frac{1}{\tau_{nrl}}$.

In the small signal modulation, when the voltage swing V_{ON}-V_{OFF} is small, f_{-3dB} depends upon nonradiative recombination, injected current (I) and active region volume (V) and can be written as[101]

$$f_{-3dB} = \frac{1}{2\pi}\left(\frac{1}{2\tau_{nrl}} + \sqrt{\left(\frac{1}{2\tau_{nrl}}\right)^2 + \frac{\beta I}{qV}}\right), \tag{2.18}$$

where q is the elementary charge and β is the band-to-band radiative recombination rate (the bimolecular recombination coefficient). Since the leaked carriers are finally lost by non-radiative recombination outside the active region and since it is difficult to discriminate the leakage lifetime, an overall non-radiative recombination lifetime (τ_{nrl}), including the leakage lifetime, should be considered. Eq. (2.18) suggests that by plotting f_{-3dB} against V, β is obtained as a slope of the curve and $1/\tau_{nrl}$ is given by an intercept. Eq. (2.18) also shows that a reduction in V (which is possible by lateral carrier confinement) increases f_{-3dB} without significant penalty in light power P_{out}. Alternatively, higher f_{-3dB} can be obtained by increasing $1/\tau_{nrl}$. This can be done by incorporating point defects into the active region[102]. Typically f_{-3dB} is 30-80 MHz for infrared LEDs[103]. For LEDs emitting in the visible spectrum, f_{-3dB} up to 65 MHz have been reported[104].

The bandwidth of the device is directly related to τ_{nrl} of carriers in the active region. This, in turn, is affected by changes in concentration of carrier traps that act as recombination centres. A detailed deep level analysis has revealed that annealing away so-called N3 traps inside the QW is mainly responsible for increased P_{out} and reduced f_{-3dB} due to increase in τ_{nrl}. This dominant N3 centre is situated 0.83 eV below the GaInP conduction band. It can, indeed, be partly or fully removed by rapid thermal annealing (up to ~ 900 °C) or by burn-in, *i.e.*, injecting current while maintaining the device at elevated temperature[105]. N3 is believed to be due to a phosphorus vacancy or an associated complex[106]. Previously, we have reported on effects of rapid thermal annealing on GaInP/AlGaInP red edge-emitting lasers[107]. Because the active region studied in those experiments closely resembled that of the RCLEDs and VCSELs of the present work, it is very likely that similar annealing effects take place in our vertical cavity devices.

f_{-3dB} variation with I having submount temperature (T_{sub}) as a parameter has been examined in Appendix 7. Increased T_{sub} speeds up the device primarily by enhancing $1/\tau_{nrl}$.

In the large-signal modulation regime, where V_{ON}-V_{OFF} is large, considerable asymmetry in rise and fall times can occur. The rise time can be more than twice as long as the fall time in RCLEDs. The shorter fall time is related to a remaining built-in electric field at the *pn*-junction after current injection has been switched off. As a result, free carriers are swept out of the quantum wells into the neutral regions of the semiconductor[88]. Normally this is completed by the time the emission intensity has dropped down to the value of 1/e. Thus, the fall time is not determined by the spontaneous recombination lifetime (~ ns range), but by a much shorter sweep-out time (~ ps range). In the small-signal region, the rise and fall times are usually reversed.

The f_{-3dB} value can be increased by pulse-shaping. A parallel RC or more complex circuit can be used to pulse-shape the square-wave drive voltage signal. The RC time constant is adjusted to coincide with the RCLED rise time. A typical increase in modulation speed is 10-30 %[89]. These kinds of peaking circuits were not employed in our experiments.

2.1.5 Applications of visible RCLEDs

The surface-emitting geometry of an RCLED with forward-directed radiation pattern displays its strength in applications such as photosensors or scanners that require a lot of light inside a small solid angle. It is possible to manufacture a 2-D matrix array using individually addressed RCLEDs. Red RCLEDs will most likely find their high-volume application as emitters, in particular, for data transfer through plastic optical fibres (POFs). The step-index (SI) fibres of about 1 mm in diameter are the choice for low-cost networks in consumer markets. Low-cost, robust POF systems have already initiated some applications in digital video, HDTV, robotics communications and automotive industry. Several companies have jointly developed a new data bus standard for cars, called MOST (*Media Oriented System Transport*)[108]. The current requirement of the standard for the data transfer is only 25 Mbit/s[109], but an increasing

number of functions inside the car require higher and higher bandwidths. RCLEDs provide a POF system with the data rate up to 500-700 Mbit/s for short distances (< 20 m). We shall discuss the results of our RCLED / POF experiments later in this Thesis in much greater details.

2.2 VCSELs

2.2.1 Lasing action

One of the most fundamental processes in optoelectronics devices is radiative recombination of charge carriers. Two distinct emission processes, spontaneous and stimulated, were postulated by Einstein in 1917[110]. He used two proportionality constants A and B to calculate the spontaneous and stimulated recombination rates, respectively, in a two-level system. In semiconductors, these levels should be replaced with two groups of energy levels, namely, the conduction and valence bands. The bimolecular recombination coefficient β corresponds to Einstein's coefficient A.

Self-absorption needs to be minimised in the active region of an RCLED: the reabsorption probability of photons emitted from the QWs into the cavity should be much smaller than the escape probability of photons through one of the reflectors. Assuming $R_2 = 1$, this condition is achieved if[89]

$$2\xi\alpha d << (1 - R_1), \tag{2.19}$$

where α and d are the absorption coefficient and the length of the active region, respectively. ξ is the antinode enhancement factor ($0 \le \xi \le 2$). Eq. (2.19) implies that RCLEDs cannot lase. This is because the magnitude of the maximum gain (g) in semiconductors is always lower than the magnitude of the absorption coefficient in an unpumped semiconductor ($|g| < |\alpha|$), so that mirror loss (1-R_1) is always larger than the maximum achievable round-trip gain ($2\xi gd$)[89]. However, a VCSEL can lase because it is possible to make $2\xi gd$ greater than all the losses combined, by properly designing the layer structure and choosing operational conditions. Spontaneous emission in a VCSEL is low, and it must remain low for lasing, at any drive current above threshold.

Material threshold gain in a VCSEL lies in the range between hundreds to thousands of inverse centimetres. VCSEL is characterised by a very short high-Q cavity, whose optical modes are well defined and widely spaced in frequency. There is often only one longitudinal mode within the gain spectrum. Consequently, threshold properties are sensitive to the lasing mode and mutual alignment of the gain peak[111]. Scaling down the dimensions of oxide-confined VCSELs leads to a decrease of the active region area, and if the same threshold current density is maintained, the threshold current will be reduced accordingly. However, this phenomenon is valid down to emitter cross-section areas of about 10 μm^2, beyond which the threshold current rapidly increases. This increase in threshold for very small devices is due to diffraction losses mainly from the oxide apertures[62].

Several gain models are needed when predicting the carrier density and band structure dependences of the gain spectrum[112,113]. The models are based on a semiclassical theory, where the laser field is treated classically and the active medium quantum mechanically[114]. Modelling starts with a Hamiltonian containing the dipole interaction and many-body Coulomb interactions among carriers. Using the Bloch equations, rate-equation approximation, perturbation theory, and *k·p*-theory, the gain equations can be written. Threshold gain (g_{th}) is expressed in terms of the threshold carrier density (N_{th}) and the transparency carrier density (N_t)[115]

$$g_{th} = A_0(N_{th} - N_t) \quad , \tag{2.20}$$

where A_0 is the differential gain dg/dN near the threshold. With $g_{th} = \frac{1}{\gamma}(\alpha_a + \alpha_d + \alpha_m)$, N_{th} can be written as

$$N_{th} = N_t + \frac{1}{\gamma A_0}(\alpha_a + \alpha_d + \alpha_m) \quad , \tag{2.21}$$

where γ is the optical energy confinement factor, which includes ξ. α_a is a average absorption loss coefficient per unit length, α_d is diffraction loss, and α_m is mirror loss:

$$\alpha_m = \frac{1}{L}\ln\left(\frac{1}{\sqrt{R_1 R_2}}\right) \quad . \tag{2.22}$$

Defining the carrier lifetime τ_c and the total active layer thickness d, the threshold current density in general can be expressed as

$$J_{th} = \frac{ed}{\eta_{inj}\tau_c} N_{th} \quad . \tag{2.23}$$

Usually τ_c can be given as

$$\frac{1}{\tau_c} \approx A + BN + CN^2 \quad . \tag{2.24}$$

The first term is a nonradiative (monomolecular) recombination independent of carrier density, the second term denotes radiative recombination, and the last term represents a non-linear process such as an Auger effect.

The differential quantum efficiency (η_d) is defined as

$$\eta_d = \eta_{inj} \frac{\frac{1}{L}\ln\left(\frac{1}{\sqrt{R_1}}\right)}{\alpha + \frac{1}{L}\ln\left(\frac{1}{\sqrt{R_1 R_2}}\right)} \quad , \tag{2.25}$$

where $\alpha = \alpha_a + \alpha_d$.

VCSELs exhibit predominantly single longitudinal lasing mode due to the short cavity. On the other hand, VCSELs tend to lase in multiple transverse modes as a result of effects of index-guided confinement in the plane of epitaxial layers. High-power single transverse mode operation is desired for a number of applications, such as optical imaging and data communication. Single-mode VCSELs can be obtained either by reducing the cavity cross-section area to decrease the number of transverse modes, or by increasing absorption loss of higher order modes. However, these actions tend to limit the output power of the fundamental mode[116]. A good way of reducing multiple transverse modes has turned out to be a combination of ion implantation and wet thermal oxidation[57]. Ion implantation is applied to form a small aperture to confine current flow, while oxidation is employed to form a large aperture for the optical mode.

2.2.2 Polarisation

VCSELs emit linearly polarised light, which may not be expected at first sight because they possess quasi-cylindar symmetry. Sometimes polarisation is random in the transverse plane. Usually, however, the polarisation vector has the preferential directions [110] and [1-10] when the VCSELs are grown on GaAs (100) substrates, but even VCSELs grown on the same wafer do not necessarily all have the same polarisation direction.

Polarisation switching (PS) from one state to the orthogonal state is a well-known phenomenon in VCSELs, as drive current is changed. PS is attributed to birefringence introduced by unintentional stress and by the electro-optical effects in the cavity and mirrors[117] or by an intentional uniaxial strain in QWs, which strain breaks heavy hole / light hole degeneracy at the Γ-point[118]. Higher order modes are polarised orthogonally to the fundamental mode. This effect is attributed to spatial hole burning, which causes the higher order mode to have the least overlap with the fundamental mode[119,120], and on it is assigned to thermal waveguiding[121]. One distinctively different model to describe the polarisation switch is a so-called spin flip model, which is based on conservation of angular momentum[122]. Experiments have proved that the PS occurs in all kinds of VCSELs. Depending on the diameter of the VCSEL, PS can appear in the fundamental mode or in higher order modes. It can also happen from a higher to lower frequency mode (called a type I PS) or from lower to higher frequency mode (type II PS). Both types of PS can even occur consecutively in one device. A theory that takes into account photon energy and temperature dependence of the modal gain and total losses and their impact on the type I and type II PS, has been introduced recently[123,124].

VCSELs exhibit dramatic variations in the partitioning of P_{out} between the two fundamental polarisations, arising from the relative spectral alignment of gain and polarisation-related cavity resonances. For infrared VCSELs, higher-order modes are typically polarised orthogonally with respect to the fundamental mode. However, red AlGaInP VCSELs exhibit very different polarisation properties. The two linear orthogonal polarisations are found to be aligned along the <110> crystal axes. The

dominant fundamental polarisation is always along one particular <110> crystal axis for all the lasers in the wafer[125]. In contrast to infrared VCSELs[126], this polarisation is maintained over the entire temperature and operation current range, although at low temperatures there is some power distributed into the orthogonal polarisation. Substrate misorientation, thickness nonuniformity or the quantum well strain are not believed to affect polarisation of the red AlGaInP VCSELs. Strict orientation of the polarisations and the absence of gain-dependent polarisation partitioning are unique properties of red VCSELs. It is likely that inherent material properties of the active region contribute to polarisation, but this contribution is not entirely clear at the moment.

2.2.3 Thermal model

In the oxide confined VCSELs, an additional function of the selective oxidation layer is to provide a lateral path for dissipation of heat from the gain region. The selective oxidation permits a wider diameter mesa to be made and simultaneously provides a narrow current aperture; the bulk of the mesa can then act as a heat sink for the active region. Thermal conduction needs to be improved for the red VCSELs; *i.e.*, obtaining P_{out} >500 μW at temperatures up to 70 °C[127] should be made achievable.

The temperature effects can be quantified using a simple finite element thermal model to calculate temperature profiles of the device for a given drive current. A phenomenological approach developed in the European BREDSELS project includes heating effects that originate from contact resistance, resistive losses in the DBRs, non-radiative recombination, and photons re-absorbed in the DBRs. The heat generated is assumed to be dissipated by conduction to the substrate. This model is used to calculate temperature profile for a 665-nm device with a 15-μm diameter aperture in a ∅49-μm mesa, biased at 10 mA and 3 V (Figure 2-7)[128]. Heat is diffused towards the substrate via the unpumped regions in the mesa.

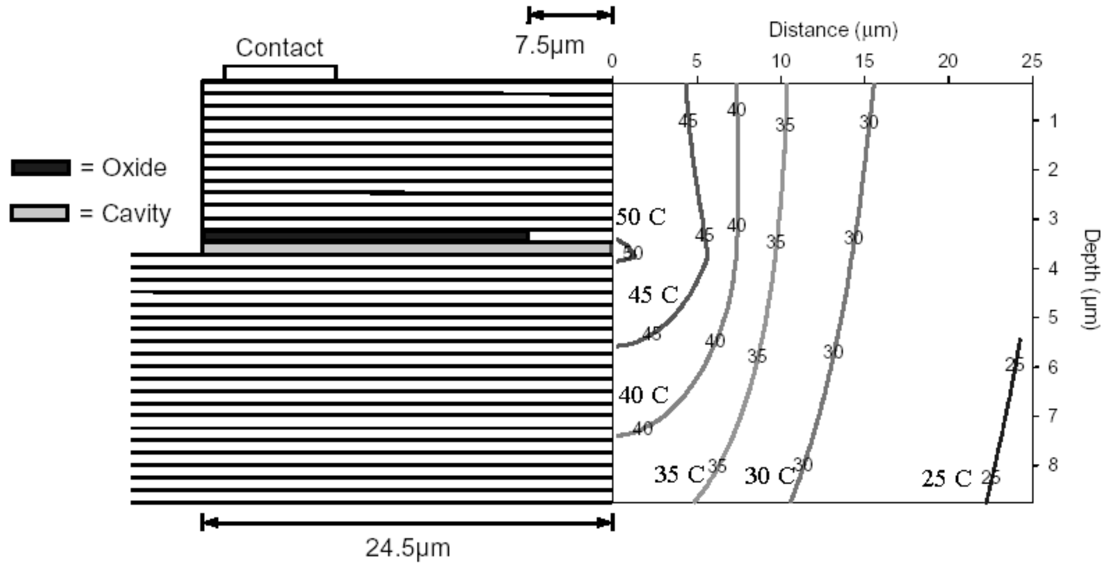

Figure 2-7. *Calculated thermal profile of a 665-nm oxide confined VCSEL[128].*

Based on these calculations, the maximum temperature in the active region is 50 °C (Figure 2-7), and a mesa diameter greater than 50 µm will no longer provide any further heat sinking benefit. Calculations also revealed that the same structure without the oxidation layer gives a temperature rise in excess of 100 °C[128]. Thermal resistance is a strong function of both current aperture and bonding pad size[129]. However, active region heating has been observed to be useful in weakly optically confined VCSELs having a very thin thermally oxidised aperture placed in the local minimum of the optical field intensity. Under CW injection, the optical confinement is improved by the formation of a thermal lens due to an increase of the refractive index in the centre of the VCSEL[49]. Although the thermal impedance tends to increase as the device size shrinks, the temperature rise for a given current density becomes smaller, as the device size is reduced. Consequently, smaller VCSELs can be driven to higher current densities before thermal roll-over takes place[68].

VCSEL arrays suffer from thermal crosstalk especially in planar proton-implanted structures. The best configuration for low thermal crosstalk is an etched-mesa design, which is flip-chip bonded in order to obtain a good heat sink[129].

2.2.4 Modulation response of VCSELs

Modulation properties of VCSELs can be predicted from the relaxation resonance (f_R). For bias currents sufficiently far above threshold, f_R depends on the differential gain ($\partial g/\partial N$) and a photon confinement factor (Γ)[68]:

$$f_R = \frac{1}{2\pi}\sqrt{\eta_i \frac{\Gamma v_g}{qV}\frac{\partial g}{\partial N}(I - I_{th})} = \frac{1}{2\pi}\sqrt{\eta_i \frac{\Gamma_{xy}\xi v_g}{qL_{eff}}\frac{\partial g}{\partial N}(J - J_{th})} \quad , \tag{2.26}$$

where v_g is the group velocity, V is the modal volume and L_{eff} is the effective cavity length. If parasitics are not too large, the –3 dB modulation bandwidth f_{-3dB} is about 1.55 f_R[129]. f_{-3dB} is proportional to $\sqrt{P_{out}}$[19].

The small active volume of VCSELs implies that f_{-3dB} may be quite high. If the operating parameters were similar to those of edge-emitting lasers, the VCSEL modulation bandwidth would be much higher than that of an edge-emitter. However, it is not possible to apply the same conditions for the VCSELs because of the high thermal impedance and series resistance of VCSELs. Nevertheless, for the same small bias current, VCSELs have a much higher modulation bandwidth. Theoretically, the modulation bandwidth of oxide-confined IR-VCSELs is as high as about 50 GHz. Gain compression due to heating, spatial or spectral hole burning, and parasitic capacitance decrease the maximum small-signal modulation response to around 15 GHz at 2.1 mA[130]. Typical commercial infrared VCSELs are operating up to 12 GHz (at I = 10 mA)[131], sufficient for 10- and 12.5-Gbit/s data communications applications[132].

Red VCSELs have been demonstrated to have a maximum f_{-3dB} response up to 11 GHz[18] at 16 mA. The maximum intrinsic f_{-3dB} of the same VCSEL was estimated to be 25.2 GHz. Limited thermal properties and optical losses caused by the current apertures are the main reasons for the decreased extrinsic bandwidth. A typical modulation bandwidth of commercial red (670 nm) VCSELs is 2 GHz (I = 2 mA)[133] at room temperature.

f_{-3dB} degrades at high T_{sub}, due to reduced gain for a given current injection, $\partial g/\partial N$ decreases due to both the temperature and the increased carrier density required for threshold[6].

2.3 Plastic optical fibres

Light attenuation in PMMA (polymethyl methacrylate) POF has local minima at 520 nm, 570 nm and 650 nm (Figure 2-8). Since any light emitter at 520 and 570 nm is very difficult to be made of III-V semiconductors, most of work in the literature is focused on the 650-nm devices as far as POF applications are concerned. The first demonstrations of optical data transmission (2.5 Gbit/s) at 650 nm with a 100-m-long POF were made in 1994[134].

Domestic office-based POF networks probably offer the greatest commercial potential for 650-nm vertical-cavity emitters. Standard PMMA-POFs seem to be very promising for automotive applications and intra-building multimedia applications[135] and may gradually replace twisted pair and coaxial cables. Two main types of consumer market applications can be distinguished: narrow-band services like phones and home automation, and broadband services, like digital TV or internet, based on the POF IEEE-1394b (so-called 'firewire' or 'i-link') and ATM standards[136]. Step-index (SI) fibres have an abrupt refractive index change between a cladding and a core, having bandwidth-distance product typically less than 10 MHz·km. Graded-index (GI) fibres have an optimised index profile to minimise modal dispersion, and

their bandwidth-distance product is on an order of 1 GHz·km. POFs are large-core fibres with core diameter of 100-3000 µm. A large numerical aperture:

$$NA = \sin\theta_A = \sqrt{n_0^2 - n_c^2} \quad , \tag{2.27}$$

where θ_A is a fibre acceptance angle, n_0 and n_c are the refractive indices of the core centre and cladding, respectively, is one of the main advantages of POF. Large NA provides a good η_{couple} and reduces bending losses[137]. On the other hand, large NA will excite more guided modes in the fibre, resulting in greater pulse broadening[138]. Furthermore, large NA causes geometrical problems at the detector end of the fibre: high-speed optical links require small detectors, which are difficult to align to the fibre output.

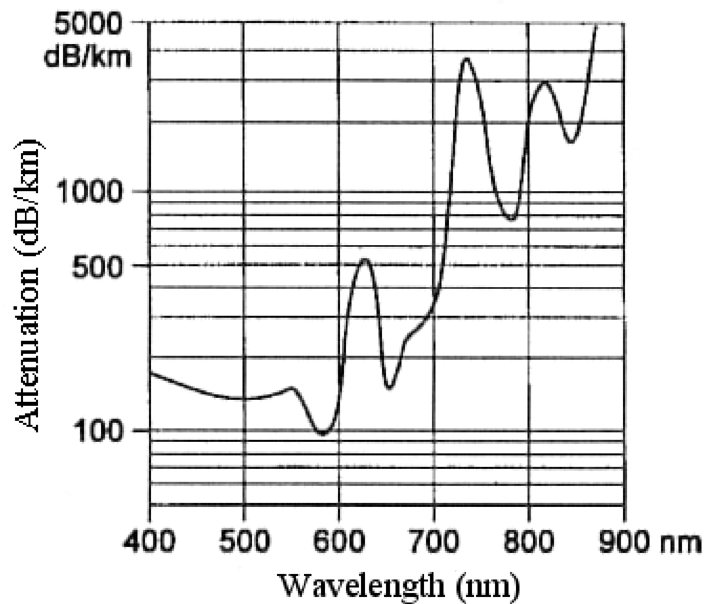

Figure 2-8. *Attenuation of light in a SI PMMA-POF as a function of wavelength. Minimum attenuation at 650 nm is about 150 dB/km.*

Low-cost POF-systems require inexpensive fibre coupling methods. To reduce the costs of butt-coupled packaging, several passive alignment schemes have been studied, such as V-grooved silicon substrates with guide pins[139], a micro-optical bench[140], hole etching, and a thick epoxy-based photoresist[141]. Relatively high coupling efficiencies (> 50 %) can be achieved using these lens-less coupling techniques.

It is important to know how the fibre properties affect the power budget of an optical link. Fibre attenuation and chromatic dispersion increase with a decrease in wavelength due to enhanced Rayleigh scattering. Scattering due to thermal fluctuations in the fibre, electrical transition absorption, and carbon-hydrogen (C-H) vibration absorption increase the attenuation. While lasers are capable of very high modulation speeds, the mode dispersion in SI PMMA-POFs limits the useful bandwidth to around 500 Mbit/s[142] for the fibres not much longer than 10 m. Up to the

link distance of 10-20 m the RCLEDs as medium-speed devices have clear advantage over slower LEDs. Newer perfluorinated (PF) polymer fibres are based on a polymer, which eliminates the intrinsic C-H absorption loss[143]. GI PF-POF offers high stability over wide temperature and air humidity range and low absorption (~40 dB/km) from red wavelength to 1.3 µm[144]. It is expected that VCSELs emitting 650-1050 nm together with low modal dispersion multimode GI PF-POF provide adequate performance for applications over distances of the order of 100 m[145,146]. POFs have an enormous market growth potential for example in vehicle industry, data communication and consumer electronics, but until now, a lack of standards, viable low-cost fibres and strong commitment by major suppliers have hindered the growth.

3. Design and development of visible RCLEDs and VCSELs

3.1 Design and simulation

Upon selecting the material system to be used, the particularities of vertical-cavity light emitters need be considered. Most of the mirror and cavity analysis relies on the determination of the reflectivity-dependence upon wavelength, incidence angle, polarisation, and layer contrast and layer thickness. The usable refractive index contrast Δn for DBR is limited by the availability of semiconductors lattice-matched to a substrate and by the requirement of low-resistivity carrier flow through the device. In order to reduce series resistance, we employed an intermediate composition layer deposited before the high bandgap layer in the direction of majority carrier flow. The composition and thickness of this intermediate layer was adjusted by analysing the heterointerface bandstructure profile under bias. To keep the optical properties of the mirrors unaffected the intermediate layer was made narrow and the thickness of the high bandgap layer was determined in such a way that the optical thickness of the combined intermediate composition and high bandgap layer was $\lambda_0/4$.

The basic principle of DBRs is the constructive reflection of light at a series of subsequent interfaces, each having $\Delta n = n_{high} - n_{low}$, where n_{high} and n_{low} are the higher and lower refractive indices of the DBR layers, respectively. Constructive interference, as shown schematically in Figure 3-1, leads to the formation of a stopband. A simulated reflectivity *versus* wavelength for 15 pairs of AlAs/ $Al_{0.50}Ga_{0.50}As$ DBR layers (λ_0 = 690 nm) is shown in Figure 3-2.

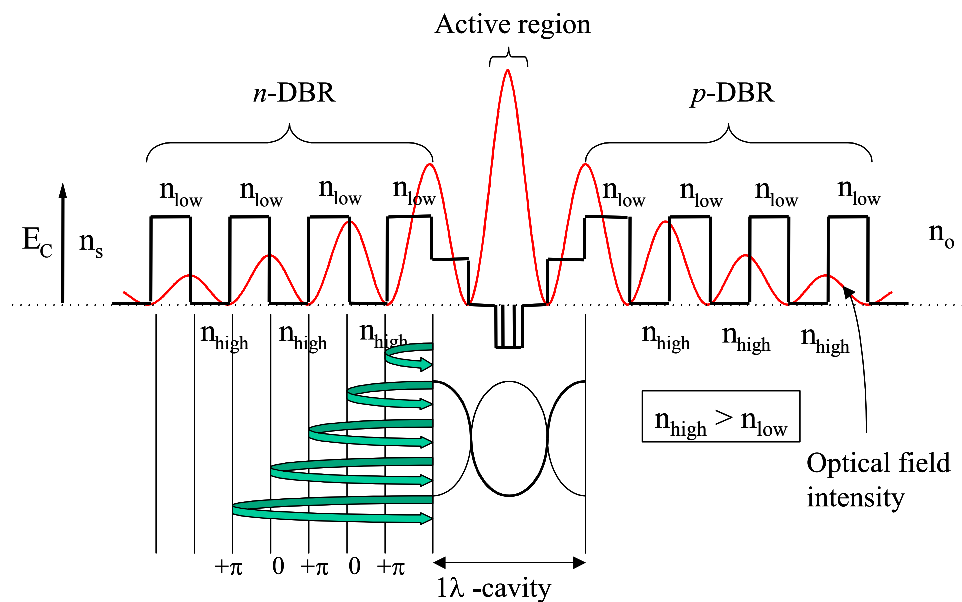

Figure 3-1. *DBRs in the 1λ-microcavity structure.*

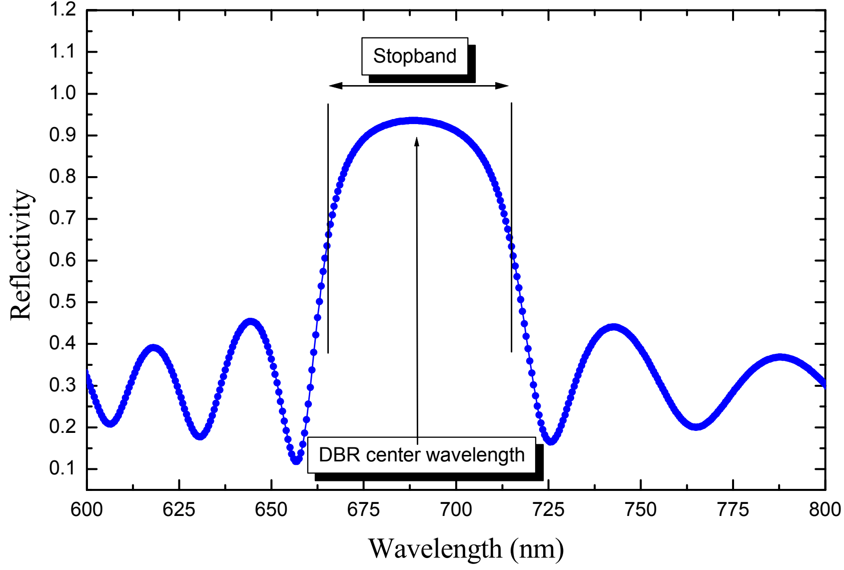

Figure 3-2. *Simulated reflectivity of 15 pairs of AlAs/$Al_{0.50}Ga_{0.50}As$. The central wavelength of the stop-band is 690 nm. The width of the stopband is about 50 nm.*

For a DBR stack having a large number of layers, a transfer matrix method was used to calculate reflection and transmission of electromagnetic radiation through the stack. A detailed description has been presented in textbooks on optics and is not repeated here.

The calculations lead to a DBR (consists of N pairs of alternating $\lambda_0/4$ layers: $n_{low}d_1 = n_{high}d_2 = \lambda_0/4$) reflectivity of[147]

$$R = \left(\frac{1 - \frac{n_s}{n_0}\left(\frac{n_{low}}{n_{high}}\right)^{2N}}{1 + \frac{n_s}{n_0}\left(\frac{n_{low}}{n_{high}}\right)^{2N}} \right)^2 \qquad (3.1)$$

for $\theta = 0°$. In Eq. (3.1) n_s is the refractive index of the substrate and n_0 of the incident medium.

In the frequency domain the stopband width $\Delta\omega$ depends on Δn and can be written as[147]

$$\Delta\omega = \frac{4}{\pi}\omega_0 \sin^{-1}\left(\frac{n_{high} - n_{low}}{n_{high} + n_{low}}\right). \qquad (3.2)$$

The argument of $\sin^{-1}$ is a so-called Fresnel reflectivity coefficient, *i.e.*, the amplitude of the reflected electric field.

In a real structure, $\Delta\omega << \omega$ and the $\sin^{-1}$ argument ≈ 0. Then Eq. (3.2) becomes

$$\Delta\lambda \cong \frac{4}{\pi}\lambda_0\left(\frac{n_{high}-n_{low}}{n_{high}+n_{low}}\right). \quad (3.3)$$

The amount of losses in DBR depends on α and L_p. The reflected intensity I is thus

$$I = I_0 e^{-2\alpha L_p}, \quad (3.4)$$

where I_0 is the intensity of incident light from the QWs. A further reduction in I is due to diffraction, because the emitter has finite dimensions.

The optical wave penetrates into the semiconductor reflector. Only a finite number of all of the layer pairs effectively reflect light. This number of pairs is given by[148]

$$m_{eff} \approx \frac{1}{2}\frac{n_{high}+n_{low}}{n_{high}-n_{low}}\tanh\left(2N\frac{n_{high}-n_{low}}{n_{high}+n_{low}}\right), \quad (3.5)$$

where N is the number of DBR pairs in the layer stack. Using m_{eff}, L_p becomes

$$L_p \approx \frac{1}{2}m_{eff}\left(d_1+d_2\right), \quad (3.6)$$

where d_1 and d_2 are the individual $\lambda_0/4n$ DBR layer thicknesses for the top or bottom DBRs. Thus, L_{eff} is the physical thickness of the cavity (L) plus the two effective penetration lengths (L_{p1}, L_{p2}) into the DBRs.

The extraction efficiency, η_{ext}, is an important design parameter. Assuming a monochromatic source and placing no limit on the collection angle (θ) the optimum η_{ext} is obtained when the cavity mode is centred in the middle of the escape window, corresponding to an emission lobe maximum at θ = 45° assuming that the cavity finesse is low enough so that the cavity mode fills the whole escape window. Figure 2-5 showed the calculated reflectivity of the top and bottom DBR mirrors together with the calculated reflectivity of a whole RCLED structure at normal incidence. Besides the cavity mode position it can be seen that while R_2 is close to unity, R_1 was chosen to have a significantly lower value. In this way, the cavity modes over the whole emission spectrum occupy as much as possible of the escape window thus increasing η_{ext}.

Like the emitted spectrum, the centre of the DBR stopband and the cavity resonance wavelength depend on temperature and bias voltage. The optimum detuning regime is achieved at a specific bias and temperature of the active region. Temperature influences both the emission spectrum, which is red-shifted with increased temperature, and the cavity resonance, which is also red-shifted, but to a less extent, due to thermal expansion and the temperature dependence of n. As a consequence, increased temperature brings the emission lobes closer together, improving η_{couple} into an optical fibre.

In order to optimise η_e and f_{-3dB}, we have analysed various cavity designs and doping profiles. The study of the optical field longitudinal distribution enabled us to compare sin- and cos-type cavities with each other, analyse the QW placement and evaluate doping profiles to reduce the free carrier absorption and to optimise the electron barrier locations to reduce carrier leakage out of the active region. Since only one of the QWs can be placed exactly at the antinode in a 1-λ cosine cavity, the additional QWs being less effectively coupled with the cavity mode, the optimum number of QWs is odd (3 or 5 per antinode) depending on the QW and barrier thickness. One supplementary antinode – for the same cavity length – is obtained when a sine cavity is used. With a sine cavity one would expect to obtain a higher modulation speed than with a cosine cavity, because the total photon density at antinodes is increased. On the other hand, the carrier injection efficiency is lowered because of a tendency of spatial hole burning and because Δn between the cavity and the first DBR layer is decreased.

Refractive indices were calculated using the formula of Afromovitz[149]. Reflectivity measurements of DBRs grown showed good agreement with simulations. Cavity detuning was achieved by adjusting the optical thickness of the microcavity 1-5 % longer than λ_{qw}. Microcavities with various designs, including 1-λ and 2-λ sine and cosine configurations, and a different number QWs and barrier widths, were grown. Structures exhibiting good photoluminescence were employed in the final RCLED growths. VCSELs were grown by making use of experience acquired in RCLED design.

3.2 Material growth

All epitaxial structures of this Thesis were grown by Molecular Beam Epitaxy (MBE). The progress since 1970, when MBE was introduced[150], has been impressive. Today it is possible to grow high-performance electronic and optoelectronic devices with an extremely high purity and precise doping concentration and layer thickness. In MBE, the substrate is placed in an ultra-high vacuum (UHV) chamber with direct line of sight to several elemental species, each of which is in an evaporation source commonly referred to as an effusion cell. By using shutters and controlling effusion cell temperatures, almost any material composition and doping profile can be achieved.

Until the last few years, phosphorus-based III-V epitaxy was only possible by metal organic chemical vapor deposition (MOCVD) or by gas-source MBE. MOCVD exhibits certain advantages over MBE for VCSEL growth, for example ease of continuous compositional grading[151], effective carbon doping[152] for low-resistance *p*-type DBRs, versatility in the source materials, and higher growth rates in manufacturing environments. Both MOCVD and gas-source MBE have the ability to produce controlled group-V fluxes needed in the growth of arsenide/phosphide heterostructures and mixed group-V compounds. These methods rely on the availability of high-purity phosphine (PH_3) and arsine (AsH_3) to supply the group-V fluxes. Both gases are extremely toxic and expensive. Furthermore, these gases (especially AsH_3) might contain some residual impurities (*e.g.* water vapour), which may cause difficulties in growing aluminium-containing materials. In addition, quite

complicated gas-handling and safety systems are needed for gaseous source epitaxy. However, a remarkable progress in the use of alternative and less toxic precursors, such as tertiarybutylarsine (TBA)[153] and tertiarybutylphosphide (TBP)[154], has been made in the recent few years.

We have employed in this work a rather novel variant of MBE, namely, Solid-Source MBE (SSMBE), developed to some extent by our group[155,156,157]. In SSMBE, valved crackers containing solid source materials (P, As) produce stable and closely controlled group-V ($As_{2/4}$, P_2) fluxes. Valved two-zone arsenic and three-zone phosphorus cracking cells have replaced the conventional elemental solid group-V sources. Group-III fluxes are generated using conventional Knudsen-type effusion cells. The use of this toxic-gas-free growth method simplifies the system requirements and reduces operating costs. With SSMBE it is possible to grow $Al_xGa_yIn_{(1-x-y)}As_zP_{(1-z)}$ alloys with a high crystal quality and composition control both on gallium arsenide (GaAs) and indium phosphide (InP) substrates[158]. In the visible wavelength region, especially high optical quality AlGaInP/GaAs alloys are needed to fabricate high-performance emitters[159]. It should be noted in passing that while lattice matching is usually needed for high-quality epitaxy, lattice strain is always preferred for the quantum wells. Unfortunately, it is not possible to make highly strained quantum wells at 650 nm ($Ga_{0.47}In_{0.53}P$ is almost lattice-matched to GaAs); higher strain would further lift the degeneracy of the heavy-hole and light-hole bands in the Brillouin zone centre and help suppress non-radiative Auger transitions.

Several possibilities exist to make DBRs of the III-V's. These possibilities include AlGaAs/GaAs, InGaAsP/InP, AlGaInP/AlInP[160], GaP/AlGaP[161] and hybrid mirrors that have an aluminium oxide $\lambda_0/4n$-layer (*e.g.* AlGaInP/Al_2O_3 or AlInP/Al_2O_3)[162]. The oxide layers are of particular interest. They can be made by a wet thermal oxidation process[163], where $Al_x(Ga_{1-x})As$ is oxidised in water vapour at ~400 °C. The low refractive index of Al-ox (n ~1.55) enables a high-reflectivity DBR to be fabricated with just a few pairs of layers. Since in some applications both light and current must go through the DBRs, the material choices are restricted by the optical absorption, electrical conduction, and energy band offsets of a DBR. A major advantage of monolithic DBRs over hybrid DBRs is that the entire device structure can be grown in a single growth step, and usually fabrication of the diode is straightforward and amenable to batch processing on the wafer. The first epitaxial DBRs were demonstrated well before monolithic VCSELs. They were made using both MOCVD[164] and MBE[165].

State-of-the-art red vertical-cavity emitters have AlGaAs/AlGaAs DBRs with Al-content of 90-100 % in low-index layers and 45-60 % in high-index layers to maintain transparency. Poor electrical properties of AlAs and absorption edge of AlGaAs at low-Al-content restrict the design of monolithic DBRs with any greater Δn on the red[166]. However, a reduced composition difference of AlGaAs in DBRs of red VCSELs compared to DBRs of IR-VCSELs does not lead as large reflectivity degradation, which could be assumed in comparison to IR-VCSELs, for which a maximum $\Delta n \cong 0.9$ given by GaAs/AlAs DBR is achievable. Due to an improved refractive index dispersion at wavelengths near the band edge of the quarter-wave layers, $\Delta n/n$ ~12 % is obtained at λ ~ 670 nm for $Al_{0.50}Ga_{0.50}As$/AlAs DBR, which is about 50 % greater than $\Delta n/n$ for the same stack at a wavelength of 980 nm[67]. Though $\Delta n/n$ is small, it still facilitates the preparation of DBRs with high enough reflectivity

and a reasonable stop-band width. In addition to fully monolithic designs, partial dielectric DBR stacks have been employed for red VCSELs[167], but such devices require intra-cavity contacts.

DBRs serve as pathways for the injected current. Mirror design is a compromise between good optical characteristics and low electrical resistance. Heterobarrier offsets in the DBR layer cause high resistance especially in the *p*-side[168]. Several modifications reducing the offsets have been introduced, including for example composition grading and/or doping profiling in the interfaces and reduced composition steps between constituent layers. To illustrate the problems associated with interfaces, we show calculated valence band profiles[67,169] in Figure 3-3A) for 20-period $Al_{0.50}Ga_{0.50}As/AlAs$ DBRs with varying composition profiles. Square-type, step-graded, linearly graded, and biparabolically-graded profiles show how the undesired spiking in the valence band edge may be reduced. Figure 3-3B) illustrates theoretical reflectances of square-shape and parabolically graded DBRs as a function of wavelength. No difference in reflectance of the two types of mirrors can be seen.

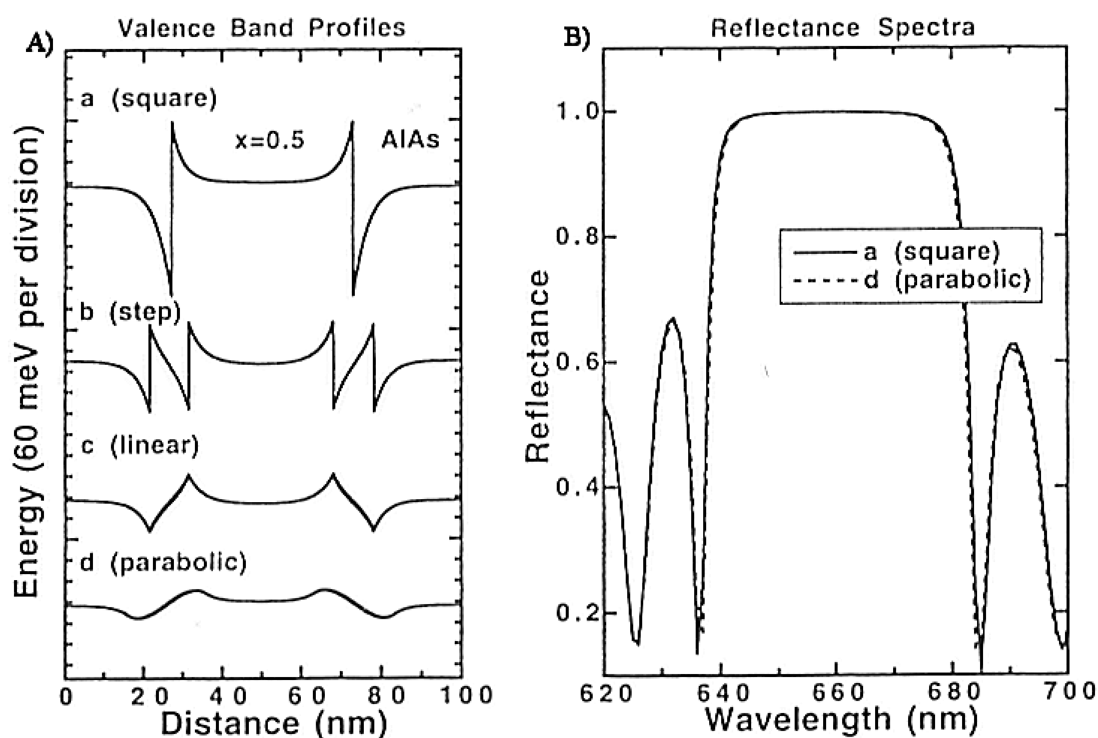

Figure 3-3. *A) Square-type, step-graded, linearly graded and parabolically-graded valence band profiles. B) Calculated reflectance spectra of squared and parabolically graded DBRs*[67] *(reproduced by permission of World Scientific Publishing Ltd).*

Doping the layers in the vicinity of a heterojunction affects the band profile[170]. Figure 3-4 shows the band discontinuities, as modified by doping either on the *n*-side or *p*-side of the structure (*e.g.* in DBRs). High doping of the low-bandgap layer near the heterointerface decreases the spiking and enhances majority carrier flow across the interface. However, it can be seen that the relative doping levels needed to reduce the

spiking are actually increasing the potential barrier (ΔE) between the layers far from the heterointerface. Thus, a changing doping profile within the DBR layers is necessary for achieving an optimum majority carrier flow.

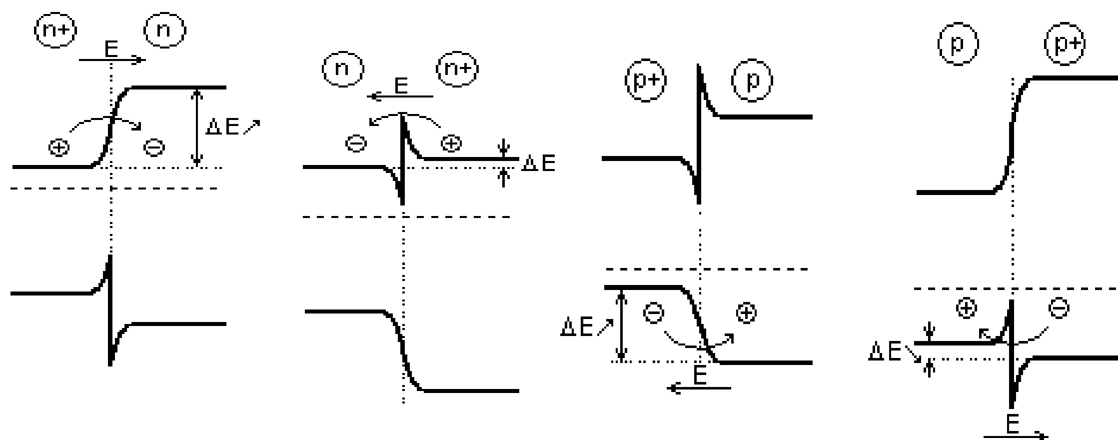

Figure 3-4. *Doping influence on the band profile in n-type and p-type heterobarriers. Arrows show the majority carrier diffusion, E is an electric field induced by the space charges, ΔE indicates the potential barrier between the layers.*

The layer structure of a closely optimised 650-nm RCLED is given in Table 3-1. These RCLEDs were grown on n^+-GaAs (100)-0° wafers. The optical 1-λ cavity was made of $(Al_{0.50}Ga_{0.50})_{0.51}In_{0.49}P$ containing from 3 to 9 compressively strained $Ga_xIn_{1-x}P$ QWs separated by 5-nm $(Al_{0.50}Ga_{0.50})_{0.51}In_{0.49}P$ barrier layers. In some experiments the cavity also comprised one or two very thin high-bandgap barrier layers ($Al_{0.51}In_{0.49}P$), which were placed on both sides or on the *p*-side of the active region to enhance carrier confinement. An $Al_{0.50}Ga_{0.50}As$ phase-matching layer ($\lambda_0/2n$) was inserted next to the GaAs substrate to avoid forming of an asymmetric structure and to satisfy the optical phase condition of the reflector. This layer also decreased the potential barrier between the substrate and the *n*-DBR. Cavity materials with larger bandgaps, such as $(Al_{0.70}Ga_{0.30})_{0.51}In_{0.49}P$, would yield a desired step-like conduction band structure, but due to increased complexity and additional interrupts needed for growth of the AlGaInP cavities, we usually omitted them.

The cavities had various detuning values ranging from $\lambda_{det} \cong 20$ nm to $\lambda_{det} < 0$ nm.

The 650-nm *n*-type (bottom) and *p*-type (top) DBRs were made of pairs of $Al_{0.50}Ga_{0.50}As$ / $Al_{0.95}Ga_{0.05}As$ with additional intermediate $Al_{0.75}Ga_{0.25}As$ layers that reduced the potential energy barriers for majority carriers (Table 3-1). *n*-DBR and *p*-DBR consisted of 32 and 4 pairs of $\lambda_0/4n$ layers, respectively, resulting in $R_2 \cong 99$ % and $R_1 \cong 60$ %. The top mirror contained two extra layers, namely, an AlAs current confinement oxidation layer placed near the cavity and a $7\lambda/4n$ p^{++}-$Al_{0.50}Ga_{0.50}As$ current spreading layer on top of the DBR. To keep free-carrier absorption low, the doping levels of DBRs were graded downwards in the vicinity of the cavity. A p^{++}-GaAs contact layer concluded the structure.

Table 3-1. *A detailed 650-nm RCLED structure.*

Layer	Material	Doping (cm^{-3})	Thickness (nm)	Note	n @ 655	Optical Path	
Buffer	GaAs	n = 9E+18	~100		3.819		
DBR_layer_H	$Al_{0.50}Ga_{0.50}As$	n = 5E+18	94.30	Phase matching	3.473	≈0.50*λ (asym.border)	
DBR_layer_I	$Al_{0.75}Ga_{0.25}As$	n = 3E+18	10.02		3.268	≈0.05*λ	
DBR_layer_L	$Al_{0.95}Ga_{0.05}As$	n = 4E+18	41.84		3.131	≈0.20*λ	
DBR_layer_H	$Al_{0.50}Ga_{0.50}As$	n = 5E+18	47.15	*30	3.473	≈0.25*λ	
DBR_layer_I	$Al_{0.75}Ga_{0.25}As$	n = 3E+18	10.02		3.268	≈0.05*λ	
DBR_layer_L	$Al_{0.95}Ga_{0.05}As$	n = 4E+18	41.84		3.131	≈0.20*λ	
DBR_layer_H	$Al_{0.50}Ga_{0.50}As$	n = 5→4E+18	47.15	*1	3.473	≈0.25*λ	
DBR_layer_I	$Al_{0.75}Ga_{0.25}As$	n = 2E+18	10.02		3.268	≈0.05*λ	
DBR_layer_L	$Al_{0.95}Ga_{0.05}As$	n = 3E+18	41.84		3.131	≈0.20*λ	
DBR_layer_H	$Al_{0.50}Ga_{0.50}As$	n = 4→1E+18	47.15	*1	3.473	≈0.25*λ	
DBR_layer_I	$Al_{0.75}Ga_{0.25}As$	n = 7E+17	10.02		3.268	≈0.05*λ	
DBR_layer_L	$Al_{0.95}Ga_{0.05}As$	n = 9E+17	41.84		3.131	≈0.20*λ	
Semicavity 1	$(Al_{0.50}Ga_{0.50})_{0.51}In_{0.49}P$	UD	42.51		3.405	≈0.221*λ	
Thin barrier	$Al_{0.51}In_{0.49}P$	UD	5.0		3.249	≈0.025*λ	
Semicavity 2	$(Al_{0.50}Ga_{0.50})_{0.51}In_{0.49}P$	UD	37.43		3.405	≈0.194*λ	
QW	$Ga_{0.47}In_{0.53}P$	UD	5.065		3.518	≈0.027*λ	
Barrier	$(Al_{0.50}Ga_{0.50})_{0.51}In_{0.49}P$	UD	5.0		3.405	≈0.026*λ	1.014 * λ
QW	$Ga_{0.47}In_{0.53}P$	UD	5.065		3.518	≈0.027*λ	
Barrier	$(Al_{0.50}Ga_{0.50})_{0.51}In_{0.49}P$	UD	5.0		3.405	≈0.026*λ	
QW	$Ga_{0.47}In_{0.53}P$	UD	5.065		3.518	≈0.027*λ	
Semicavity 2	$(Al_{0.50}Ga_{0.50})_{0.51}In_{0.49}P$	UD	37.43		3.405	≈0.194*λ	
Thin barrier	$Al_{0.51}In_{0.49}P$	UD	5.0		3.249	≈0.025*λ	
Semicavity 1	$(Al_{0.50}Ga_{0.50})_{0.51}In_{0.49}P$	UD	42.51		3.405	≈0.221*λ	
DBR_layer_L	$Al_{0.95}Ga_{0.05}As$	p = 9E+17	41.84		3.131	≈0.20*λ	
DBR_layer_I	$Al_{0.75}Ga_{0.25}As$	p = 7E+17	10.02		3.268	≈0.05*λ	
DBR_layer_H	$Al_{0.50}Ga_{0.50}As$	p = 1E+18	47.15		3.473	≈0.25*λ	
DBR_layer_LO	AlAs	p = 4E+18	42.27	Oxidized	3.099	≈0.20*λ	
DBR_layer_I	$Al_{0.75}Ga_{0.25}As$	p = 7E+17	10.02		3.268	≈0.05*λ	
DBR_layer_H	$Al_{0.50}Ga_{0.50}As$	p = 1→4E+18	47.15		3.473	≈0.25*λ	
DBR_layer_L	$Al_{0.95}Ga_{0.05}As$	p = 3E+18	41.84		3.131	≈0.20*λ	
DBR_layer_I	$Al_{0.75}Ga_{0.25}As$	p = 2E+18	10.00	* 1	3.268	≈0.05*λ	
DBR_layer_H	$Al_{0.50}Ga_{0.50}As$	p = 4E+18	47.15		3.473	≈0.25*λ	
DBR_layer_L	$Al_{0.95}Ga_{0.05}As$	p = 3E+18	41.84		3.131	≈0.20*λ	
DBR_layer_I	$Al_{0.75}Ga_{0.25}As$	p = 2E+18	10.00		3.268	≈0.05*λ	
DBR_layer_H	$Al_{0.50}Ga_{0.50}As$	p = 4E+18→2E+19	330.05		3.473	≈7*0.25*λ	
Cap layer	GaAs	p = 3E+19→7E+19	42.88		3.819	≈0.5*λ	

The red VCSELs were even more complex than the 650-nm RCLEDs. Their layer structure is depicted schematically in Figure 3-5. The longer wavelength (690 nm) was achieved by increasing the amount of indium in GaInP QWs, which increased the compressive strain to 0.86 % from 0.34 % of the QWs of RCLEDs. The optimised growth temperature (T_{gr}) was 510 °C for the active region and 590 °C and 530 °C for the *n*- and *p*- mirrors, respectively. Growth rates were 1.5 μm/h for the DBR layers and 1.8 μm/h for the AlGaInP active layers.

The VCSEL consisted of $Al_{0.95}Ga_{0.05}As$ / $Al_{0.75}Ga_{0.25}As$ / $Al_{0.50}Ga_{0.50}As$ DBRs and an $(Al_{0.3}Ga_{0.7})_{0.51}In_{0.49}P$ active region, which contained 3 or 5 compressively strained $Ga_xIn_{1-x}P$ QWs placed at the antinode of the cosine 1-λ cavity mode. The barriers were kept nominally unstrained. It appeared that the 3-QW system had a higher PL efficiency than did the 5-QW system likely due to partial relaxation of the 5-QW active region under too high net strain. The bottom *n*-DBR had 55.5 pairs of $\lambda_0/4n$

layers, and the top p-DBR had 38 pairs of $\lambda_0/4n$ layers. An asymmetric $Al_{0.75}Ga_{0.25}As$ intermediate layer was added to reduce series resistance. To improve the current confinement, an AlAs layer for later wet thermal oxidation was grown close to the cavity. The doping profile was graded for the DBRs from 1 x 10^{18} to 5 x 10^{17} cm^{-3} near the cavity to reduce optical losses to free carriers in the region where the optical field was high. The cavity was positively detuned ($\lambda_c > \lambda_{qw}$) to align cavity length with the gain peak that is red-shifted, as current injection is increased (heating effect).

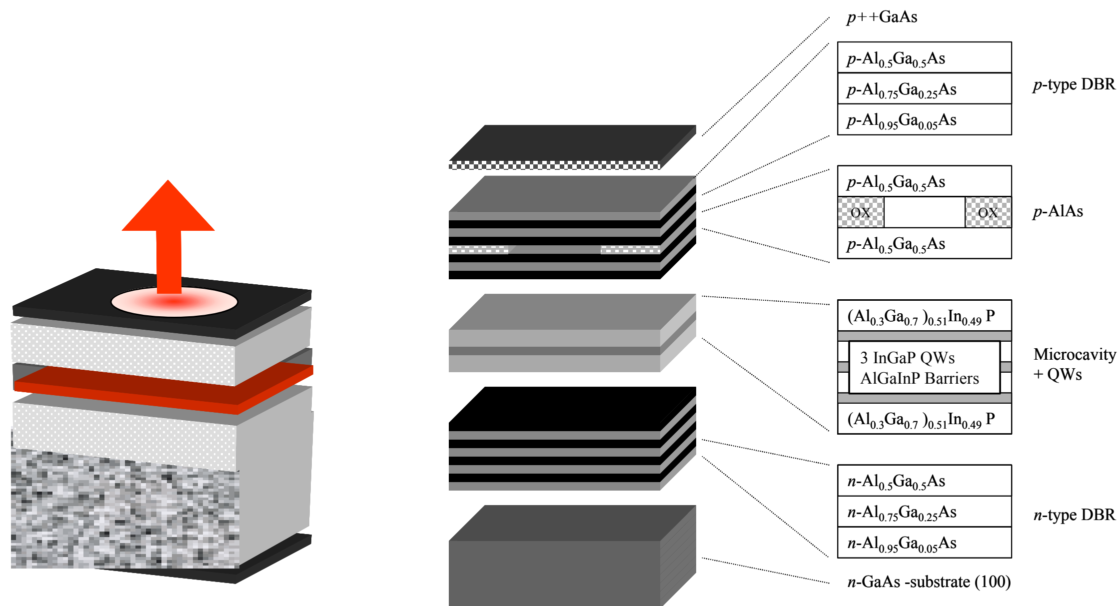

Figure 3-5. *690-nm VCSEL structure.*

3.3 Device processing

Processing the RCLED and VCSEL structures followed standard lithographic procedures. SiO_2 films were deposited onto the epiwafers, followed by a rapid thermal annealing (RTA) at 880 °C. Then the SiO_2 layer was removed, and a SiN layer was grown. A circular mesa was formed by $SiCl_4$ dry etching. Mesas had window diameters of 10, 12, 15 and 20 μm and 40, 84, 150, 300, and 500 μm for VCSELs and RCLEDs, respectively. Next, the $Al_x(Ga_{1-x})As$ layer was oxidised by wet thermal oxidation, which yielded a current aperture of approximately the same size as the window diameter. Then, a ring-type top *p*-metal of Ti/Pt/Au and bonding pads were prepared by e-beam evaporation. For the RCLEDs, the top metal pattern had current spreading fingers across the window area to reduce current crowding (see Figure 3-6). Finally, an *n*-metal of Ni/Au/Ge/Au was evaporated on a thinned backside of the substrate. The whole structure was then annealed at 420 °C to form good ohmic contacts.

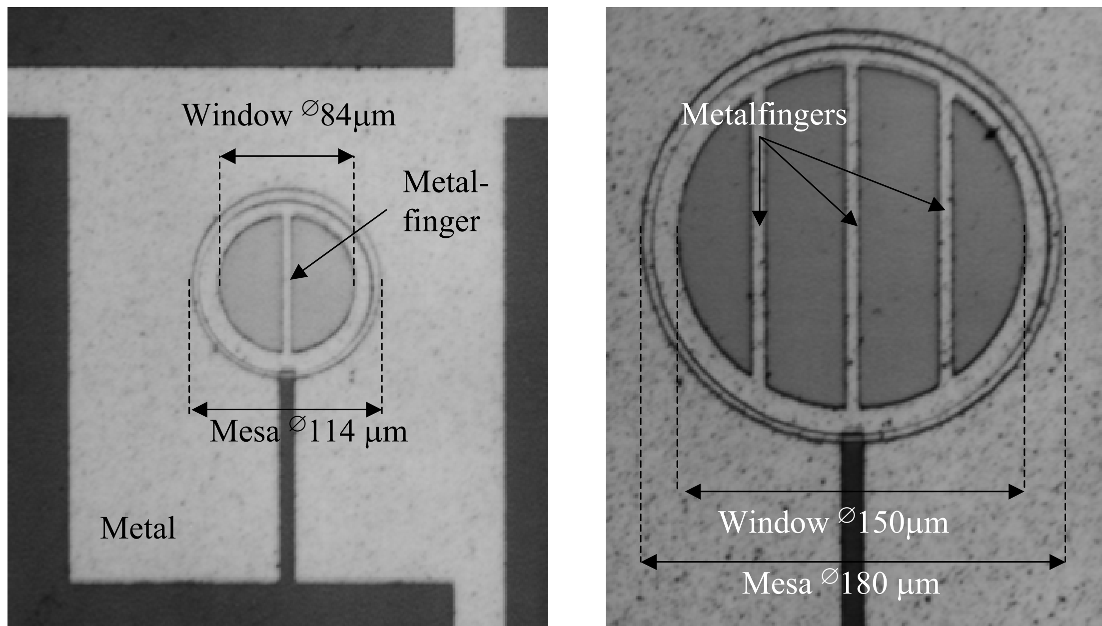

Figure 3-6. *Top metal finger patterns for RCLEDs with ∅84-μm and ∅150-μm emission windows to reduce current crowding.*

Processed samples were diced into single devices, which were bonded on TO-46 cans with conductive silver filled epoxy. Some devices were encapsulated with a transparent epoxy cap to protect the surface of the device and to reduce losses caused by total reflection in the semiconductor/air interface.

3.4 Characterisation

Crystal quality, lattice matching, active region layer thicknesses, and average strain were studied using double-crystal X-ray diffraction (XRD). XRD simulation programs were used for interpreting of the results. PL measurements were made on an optical table, which enabled us to use various laser wavelengths and optical set-ups. Argon-ion laser (488 nm) and Si-photodetector with a chopper, a computer-controlled locking amplifier and a monochromator were used. Of course, the peak wavelength of QW emission of the final devices could not be determined from the PL measurement on unprocessed RCLED or VCSEL wafers, due to modulation by the Bragg mirror reflectivity spectrum. Reflectivity *versus* wavelength plots of the DBRs and device structures were made by a commercial measurement station. Simulation tools and databases of material parameters were used for analysing and planning the DBRs and complete device structures.

An optical pyrometer was used for *in-situ* monitoring of T_{gr}. During device growth, combined reflectivity assisted pyrometry and reflectivity measurements were employed with a Pyritte-RS monitoring system. An example of the measurement data is given in Figure 3-7. The device grown in this example was a 9-QW 650-nm RCLED. The light source was a 650-nm LED, and a CCD-camera was used to align

the optics during the growth. Reflectivity shows clear oscillations.

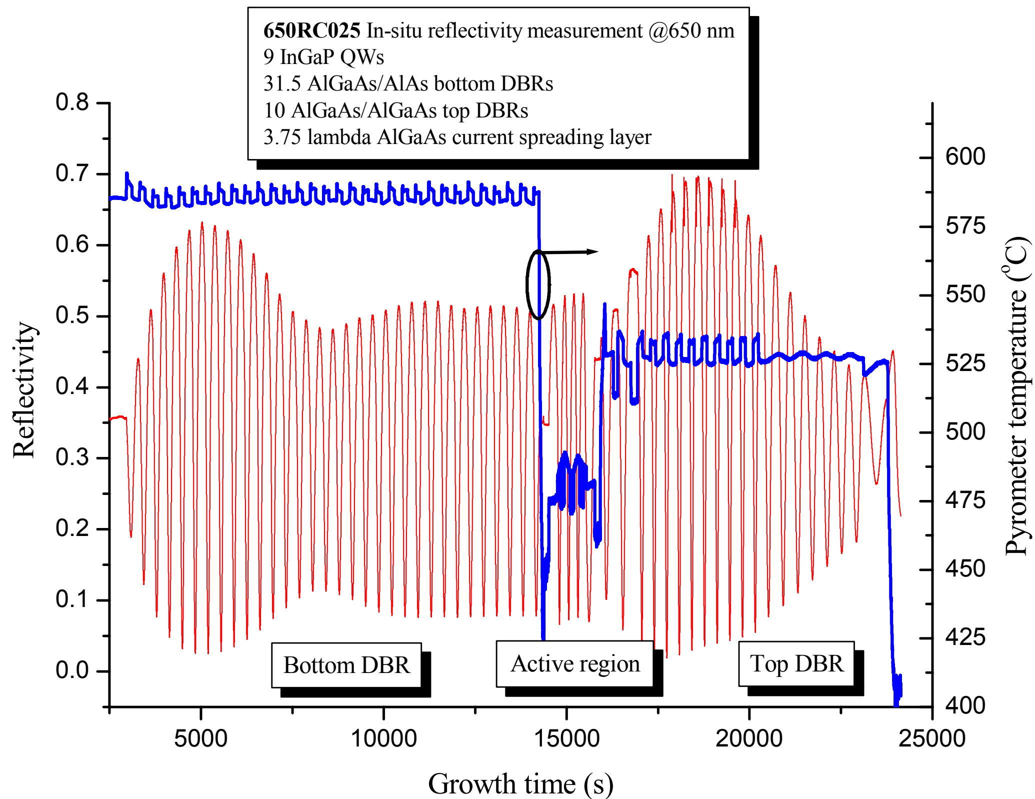

Figure 3-7. *In-situ reflectivity and pyrometer temperature measurements of an RCLED. The device contained 9 QWs. Every quarter-wave layer is revealed by this technique.*

P_{out}-V-I curves, wavelength, and far-field distribution were studied. For the measurements we employed a device parameter analyser and a special angle-resolved rotation stage system.

Scanning Near-field Optical Microscopy (SNOM) was utilised for studies of near-field distribution which provided valuable information of uniformity of emission across the exit window. SNOM results are presented in Appendix 2.

The burn-in tests were performed under constant temperature and current conditions. Upon burn-in, *Deep Level Transmission Spectroscopy* (DLTS), *Isothermal Capacitance Spectroscopy* (ICTS), and *Time-resolved PL* (TRPL) measurements were made. Accelerated ageing of the devices was performed in a computer-controlled life-tester.

Scanning Electron Microscopy (SEM) was used to evaluate different technological approaches regarding wet thermal oxidation and device processing. *Transmission Electron Microscopy* (TEM) was employed in basic material analysis and interface quality optimisation. *Secondary Ion Mass Spectroscopy* (SIMS) measurements provided information about doping species, and unintentional impurities, such as C

and O. SIMS information was particularly useful in attempts to optimise growth interrupts and monitoring purity of the P source.

Small-signal modulation properties and data transmission rates were studied using a network analyser, a 3-GHz bias-tee, and a calibrated 1-GHz Si photodetector equipped with a low-noise amplifier and free-space optics.

Photomodulated Reflectance (PR)[103,171] is a method where a small spot of the sample is illuminated with light focussed from a monochromator. Simultaneously a chopped laser source is incident on the same spot, which modulates R. Both λ_{qw} and λ_c can be determined from the measured reflectance spectra for varying θ. PR was not employed in this work.

4. Experimental results

4.1 RCLEDs

4.1.1 Output characteristics

Before growth of the vertical-cavity emitters, we made sure that good results were obtained for corresponding edge-emitting devices. It turned out that the properties of our lasers were very comparable to those exhibited by the best MOCVD-grown lasers[172]. Record-high quantum efficiencies of ridge-waveguide lasers were demonstrated at 650 nm[173] and 680 nm[174].

Our first SSMBE-grown 670-nm RCLEDs were reported in 1997[47]. They had a 1-λ cavity and Al-ox aperture and they exhibited P_{out}(CW) = 1.1 mW and $\eta_e \approx 2.0$ %. Fibre coupling experiments and further device optimisation results followed soon after that[175]. More systematic work was possible when the development of the visible vertical cavity emitters could be included in several domestic and international research programs, which we participated in.

Our main goal was to improve P_{out} and η_e of the RCLEDs. As a result, we could develop RCLEDs that exhibited very high η_e up to 9.5 % [Figure 4-1a)]. This η_e is almost the theoretical maximum, which is about 11 %. Theoretically $\eta_e \approx \eta_{ext}\eta_i$ (neglecting Fresnel reflection and contact shadowing), where $\eta_{ext} \approx 1/m_c \approx 1/(2+n/2\Delta n)$. Assuming that η_i is 90-100 %, η_e is about 11 %. The P_{out}-I curves level off, as the injection current is increased, due to saturation mechanisms via thermal and carrier band filling processes. The $^{\varnothing}$84-μm devices launch $P_{out} \approx 2.5$ mW at drive current I = 25-30 mA with $\eta_e \approx 5$-6 %. Larger devices ($^{\varnothing}$500 μm) are better heat sinks. They emit high power, up to 15 mW at $I \approx 150$ mA with η_e of 5 % [Figure 4-1b)]. Lower η_e in the larger emitters is believed to be due to non-optimised top metal contact and too thin a current spreading layer, which cause current crowding and non-uniformity in light distribution across the exit window.

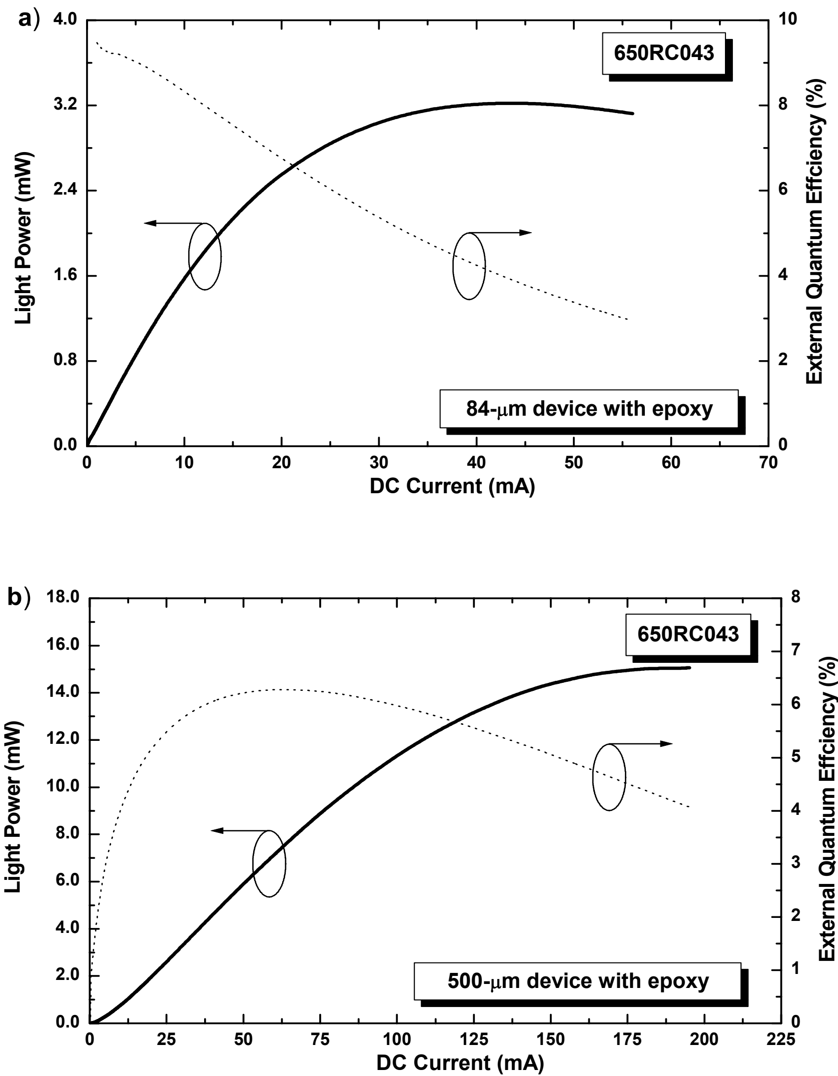

Figure 4-1. *Light power and external quantum efficiency for closely optimised a) $^{\varnothing}$84-μm RCLEDs and b) $^{\varnothing}$500-μm RCLEDs. Devices are capped with transparent epoxy, and they have had a short burn-in treatment.*

Table 4-1 summarises 10 different RCLED designs and their key characteristics. In 650RC004, higher cavity finesse was achieved, which resulted in narrow emission lobes tilted 48° from the surface normal. 650RC032 had slightly negative detuning, and this device achieved good fibre coupling efficiency (η_{couple}) but poor P_{max}. 650RCT05 had exceptionally high doping and a slightly smaller oxide aperture than did the other RCLEDs, which resulted in better modulation performance. The highest P_{out} and η_e were obtained for 650RC043. The detuning in this device was close to 45°, which yielded high η_e of 9.5 % in accordance with theory. Relatively low modulation speed f_{-3dB} = 135 MHz at I = 40 mA suggests us that non-radiative recombinations in the active region were reduced due to good crystal quality.

Table 4-1. *Summary of 10 RCLEDs (* = no data available). Top/Bottom DBR: number of DBR layer pairs, λ: emission wavelength, λ_{det}: detuning, θ: angle of the emission lobe with respect to surface normal.*

20 °C	*Top DBR*	*Bottom DBR*	*λ (nm)*	*λ_{det} (nm)*	*θ (°)*	*P_{max} (mW)*		*η_e (%) peak*		*f_{-3dB} (MHz) 10 mA*		*f_{-3dB} (MHz) 40 mA*	
Structure						*84 µm*	*150 µm*	*84 µm*	*150 µm*	*84 µm*	*150 µm*	*84 µm*	*150 µm*
650RC004	12	32	652	14	48	1.9	2.0	3.3	2.5	115	*	145	*
650RC012	6	32	652	0	0	0.3	0.3	0.2	0.2	*	*	*	*
650RC014	6	32	654	14	50	*	0.6	*	0.4	*	*	*	*
650RC015	6	32	653	6	30	0.3	0.5	0.3	0.4	*	*	*	*
650RC017	6	32	652	6	30	1.7	3.5	2.6	2.8	70	*	120	*
650RC032	6	35	645	-5	0	0.5	1.5	1.0	0.9	80	*	140	*
650RC042	4	35	656	10	38	1.9	2.2	3.3	3.0	*	*	*	*
650RC043	4	35	655	12	40	3.0	6.3	9.5	7.8	75	50	135	85
650RC046	4	35	646	15	43	0.6	0.7	1.0	0.6	*	*	*	*
650RCT05	5	32	650	7	32	1.4	3.3	3.2	3.8	110	60	225	110

Results achieved are comparable to the best ones reported in the literature by other groups, but no straightforward comparison with those is possible because we do not know their interior structures, especially their cavity detuning, emitter and oxide aperture sizes, and top mirror reflectivities. Anyway, Table 4-2 shows approximately at what level the technology of state-of-the-art RCLEDs is today. We should note in passing that we have co-operated in the development of RCLEDs with several partners over a few past years, notably with an IMEC group (Belgium), Osram Opto (Germany), Zarlink Ltd. (Sweden), and Imperial College London (U. K.). Our partners have demonstrated high P_{out} at 640-660 nm, as well (see Table 4-2). In particular, Osram Opto has reported fully comparable results to those of ours, sometimes even marginally better[176]. We should also note that the team at the University of Surrey (U. K.) has developed novel, very useful characterisation methods for RCLEDs and VCSELs[177].

Table 4-2. *Overview of the latest red RCLED results (* = no data available).*

20 °C, CW Group/company	*Year*	*Method*	*λ (nm)*	*φ (µm)*	*P_{max} (mW)*	*η_e (%) peak*	*η_{wp} (%) peak*	*Remarks*	*Ref.*
FireComms	2001	*	650	*	0.4	*	*	Typical values	178
IMEC	2000	MOCVD	650	200	4.0	4.4	*	Ge-substrate, 5 µm current spreading	179
	2001	MOCVD	640	200	7.0	5.2	*	Ge-substrate, cobweb mask, 3 µm current spreading	180
Imperial College of Science	2000	MOCVD	650	400	1.4	6.0	*	*	181
ORC/TUT	**2001**	**SSMBE**	**655**	**84**	**3.0**	**9.5**	**9.6**	**Ox-aperture**	182
Osram Opto	2001	MOCVD	640	80	2.9	9.2	9.5	Ion implanted	176
Sandia National Laboratories	1993	MOCVD	661	10	0.02	*	*	*	21
	1993	MOCVD	670	35	*	*	*	Ion implanted, all-AlGaInP	22
University of Surrey	2001	MOCVD	652	75	0.35	1.25	*	Ion implanted	103
Zarlink Semiconductor	1998	MOCVD	660	84	2.3	4.8	*	Ion implanted	28

The coherence length ($\Delta l_c = c\Delta\tau_c$) of an RCLED has been very little studied until now. Knowing Δl_c helps to estimate the overall emission linewidth for arbitrary NA

values of a receiver (*e.g.* a fibre). A research group in England[100] carried out calculations and measurements of Δl_c. They calculated Δl_c by obtaining the frequency spectrum $\nu = c/\lambda$ of an integrated wavelength spectrum for an appropriate NA of the fibre, and then Fourier transforming the spectrum $I(\nu, \mathrm{NA})$ to produce a time-domain self-coherence function $\Gamma(\tau)$:

$$\Gamma(\tau) = F^{-1}\{I(\nu, NA)\}. \tag{4.1}$$

From Eq. (4.1) $\Delta\tau_c$ was found by using the Born-Wolf approximation[183] for a normalised r.m.s. width of the squared modulus of $\Gamma(\tau)$[100]:

$$(\Delta\tau_c)^2 = \frac{\int_{-\infty}^{\infty} \tau^2 |\Gamma(\tau)|^2 d\tau}{\int_{-\infty}^{\infty} |\Gamma(\tau)|^2 d\tau}. \tag{4.2}$$

The results from Eq. (4.2) are shown in Figure 4-2. Δl_c appears to be 30 µm when NA = 0 and 20 µm at standard PMMA-POF NA = 0.50. The calculations are in good agreement with direct interferometric measurements carried out with a Michelson interferometer in the time domain, confirming a similar trend of decreasing Δl_c with increasing NA. It is noteworthy that the NA-dependent Δl_c ($\approx$ 30 µm at best) lies between the coherence length of an ordinary LED with typical $\Delta l_c \leq 8$ µm, and a laser diode, which has $\Delta l_c \geq 200$ µm, indicating that emission from the RCLED is an intermediate form of emission from LEDs and VCSELs.

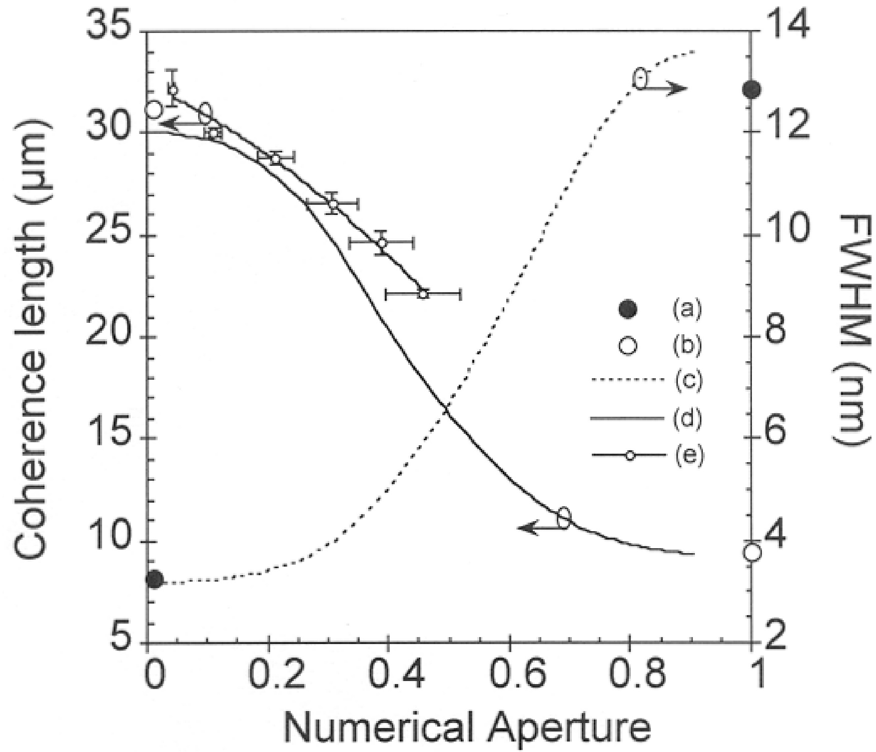

Figure 4-2. *(a) Experimental spectral line widths (•) for NA ≈ 0 and 1. (b) Experimental coherence lengths (o). (c) Semi-empirical calculation of emission line width for a continuous range NA = 0 → 1 (----). (d) Semi-empirical calculation of coherence length for continuous range of NA (—). (e) Coherence length obtained by direct interferometric measurements (—o—)* [100].

It is also seen from Figure 4-2, that the line width (FWHM) is very much smaller for the low-NA than for high-NA. This is because the larger acceptance cone of the high NA-fibre allows for more modes to be transmitted. On the other hand, the FWHM of 13 nm of the envelope spectrum even for the high-NA is remarkably narrower than what is observed for an ordinary LED (FWHM ≥ 20 nm).

4.1.2 Modulation response

It has been shown that f_{-3dB} and P_{out} of visible RCLEDs and VCSELs are directly affected by the nonradiative lifetime of charge carriers in the GaInP active region. After burn-in for about 60 hours[184] of a ∅40-μm RCLED f_{-3dB} decreased about 30 %, and while P_{out} increased 150 %. Meanwhile, the band-to-band recombination rate (β) was found to be in the range 0.9-1.8 m^3s^{-1}. τ_{nrl} increased from 1.63 ns for the as-grown devices down to 3.75 ns for the 60-h burnt-in devices. In order to identify the source of the observed annealing behaviour, deep level transient spectroscopy (DLTS), time-resolved photoluminescence, and isothermal capacitance spectroscopy (ICTS) measurements were carried out. Our aim was to seek signs of recombination enhanced annealing (REA) in the active material. The DLTS revealed that annealing N3 electron traps away from the QWs was mainly responsible for increased optical

output power and reduced modulation speed, due to increase in overall τ_c. According the Arrhenius data, this dominant recombination centre is located 0.83 eV below the GaInP conduction band and it is partly or fully removed by rapid thermal annealing (up to ~ 900 °C) or by current injection (burn-in) at elevated temperatures. A capture cross section of the trap was determined[105] to be 4 x 10^{-14} cm^2, and trap concentration in an undoped GaInP sample was found to be about 1 x 10^{14} cm^{-3}.

The N_3 deep levels and other point defects are typical of MBE-grown semiconductors. As seen above, the number of these defects can be reduced quite effectively by annealing.

Figure 4-3 shows small-signal modulation bandwidths for RCLEDs (650RCT05) with different emitter window sizes. A small device (∅40 μm) exhibited a bandwidth in excess of 300 MHz with low drive current. This high bandwidth was achieved by decreasing the aperture diameter, which increased the current density in the active region [see Eq. (2.18)]. As mentioned in Chapter 2, the microcavity effect does not affect modulation response significantly (20 % at most). P_{max} is reduced for RCLEDs with small windows thus indicating that there is a trade-off for the power-bandwidth product.

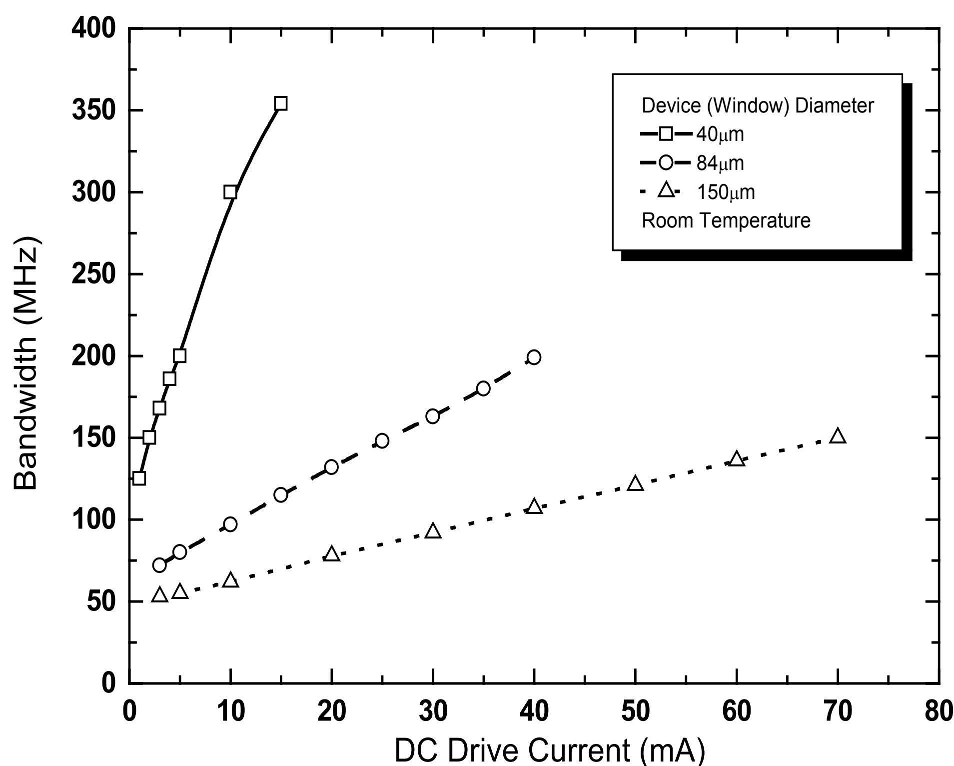

Figure 4-3. *Modulation bandwidths of 650-nm oxide-aperture RCLEDs with exit window sizes of ∅40, ∅84, and ∅150 μm, measured at room temperature.*

Back-to-back transmission experiments (no fibre) provided information about the dynamic properties. Figure 4-4 shows eye diagram of an 1-Gbit/s transmission rate for an ∅84-μm RCLED biased at I = 40 mA and modulated with V_{mod} = -0.6V. This transmission rate should be regarded very high, indeed, bearing in mind that it was achieved by using a spontaneous light source.

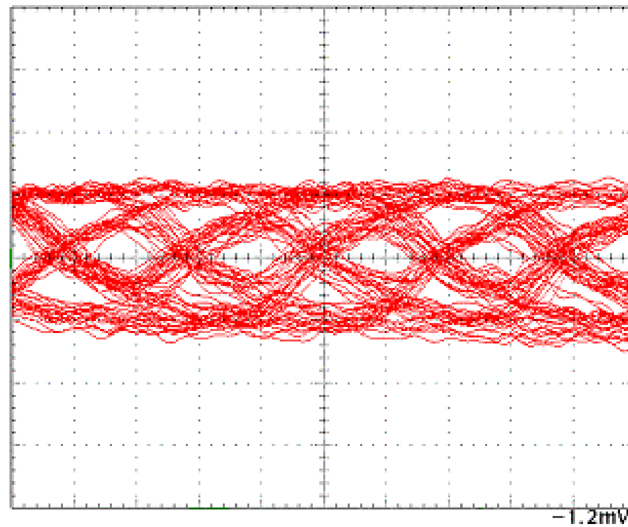

Figure 4-4. *Eye diagram for a 1-Gbit/s back-to-back transmission experiment with an ∅84-µm RCLED biased at I = 40 mA and modulated with* V_{mod} *= -0.6 V.*

Error-free transmission at 622 Mbit/s over a 1-m SI POF (NA = 0.5) was obtained for an ∅84-µm device without any auxilary optics or special electronic circuitry. Figure 4-5 shows comparison between 622 Mbit/s data transmission experiment without a fibre and with a 1-m SI PMMA-POF (NA = 0.50).

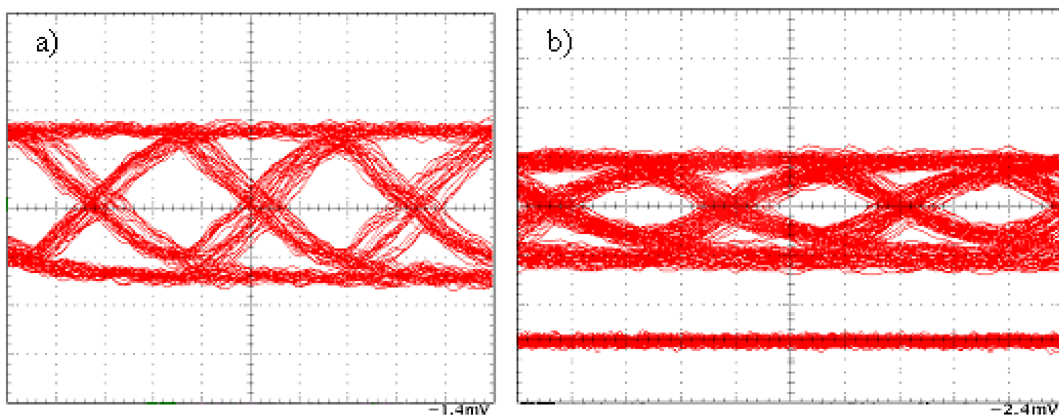

Figure 4-5. *Eye diagram for a 622-Mbit/s transmission experiment using an ∅84-µm RCLED light source a) back-to-back coupled, b) 1-m SI PMMA-POF (NA = 0.50) (the lower trace is a receiver noise floor).*

A bandwidth dependence on the launching angle and fibre length were examined, too. It was observed that mode coupling comes strongly into play, as fibre length is increased, and over 20-m distances the SI PMMA-POF itself limits the bandwidth. These measurements are described in more detail in Appendices 6 and 7.

4.1.3 Temperature coefficient

Most of the RCLED characteristics experience changes with temperature. In order to isolate the temperature effects from other factors we made a series of measurements where the only changing parameter was the submount temperature T_{sub}. The resonance wavelength of the F-P cavity shifted with temperature, due to a change in n[185] and in layer thicknesses. The cavity modes shifted to longer wavelengths and the QW emission broadened, as temperature was increased, due to carrier bandfilling and changes in Fermi-Dirac distribution. The shift of the cavity resonance mode (~0.04 nm/°C) was much smaller than the shift of the peak wavelength (~0.14 nm/°C) emitted from the AlGaInP/GaInP system.

Although temperature-related changes in performance characteristics of red RCLEDs are minor compared to those of red VCSELs, there is still room for improvement. The most severe drawback in high-temperature behaviour of the RCLED is power saturation at high current injection. Main problems at 50-90 °C are the carrier leakage out of the QWs, photon absorption to free carriers in the DBRs, and increased τ_{nrl} in AlGaInP.

We have determined the temperature coefficient (TC) in an attempt to quantity the thermal effects:

$$TC = 100\% \frac{P - P_0}{P_0 (T - T_0)} , \tag{4.3}$$

where P_0 and P are the power levels at initial temperature T_0 and final temperature T, respectively. TC was found to vary from –0.72 %K^{-1} for I = 10 mA to –0.89 %K^{-1} for I = 40 mA in the range $10 < T_{sub} < 85$ °C for free-space emission. When P was measured from the end of a 1-m long SI PMMA-POF (NA = 0.5), the devices having wider far-fields ($\theta \sim 50°$) yielded somewhat smaller TC, –0.50 and –0.83 %K^{-1} at the aforementioned currents and temperatures, respectively[186], but due to the wider far-field η_{couple} was poorer. The results are comparable to those presented by other groups[28,103], but considerably higher than TC for a conventional LED ($|TC| < 0.3$ %K^{-1}). The deterioration of TC at higher temperatures is attributable to several factors: 1) η_e is decreased as the detuning is reduced; 2) η_e is reduced by QW emission broadening; 3) carrier leakage and nonradiative recombination are thermally enhanced. Furthermore, a small active volume leads to rapid heating, as I is increased. High TC is an inherent problem of all the present 650-nm RCLEDs. A new AlGaInP active region for obtaining lower TC is under development, but not much improvement is expected. Stable and reliable operation of the emitter over a wide temperature range is needed for many applications, in particular, in the automotive industry.

4.1.4 Reliability

At this writing, our red RCLEDs have been on aging tests for about 100,000 device-hours. No degradation in P_{out} is observed so far. The group of 7 devices have been operating over 14,000 hours at constant I corresponding to P_{out} = 0.4 mW in the

beginning of the test. The devices are packaged in TO-46 cans and held at 60 °C (4 devices) and 90 °C (3 devices)[187] (Figure 4-6). All these tests are planned to continue indefinitely.

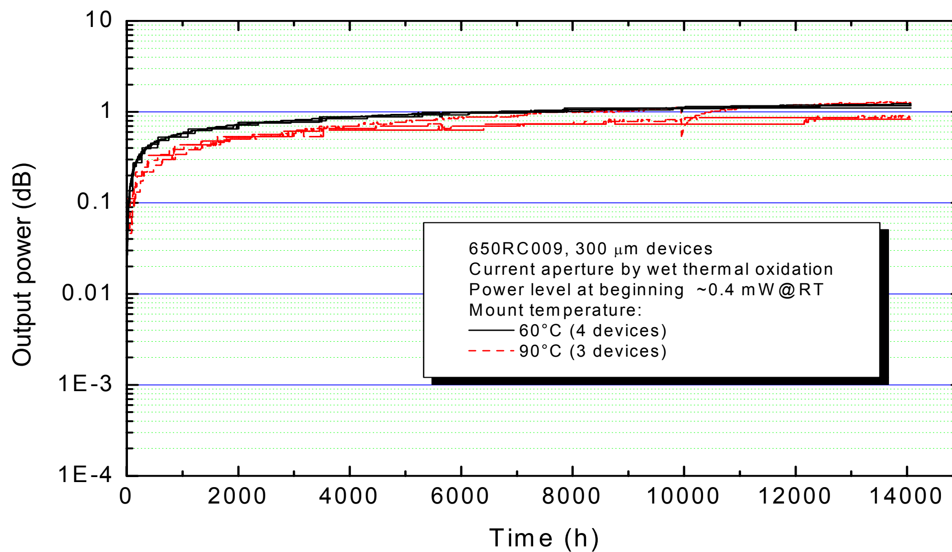

Figure 4-6. *Ageing test for seven 650-nm RCLEDs performed in automated injection current controlled mode at 60 and 90 °C.*

No MTTF can be estimated for these devices, because if the MTTF analysis were applied to our data, it would essentially predict indefinite lifetimes regardless of the chosen functional form. In any case, it remains a major achievement to accumulate this large quantity of device-hours at high ambient temperature without having incurred a single unexpected failure or even gradual decrease in light power, providing clear-cut evidence that the RCLEDs are extremely reliable devices.

4.1.5 Plastic optical fibre coupling

Installation costs and maintainability of fibre-optic communication systems are strongly affected by the required alignment tolerances of the emitters and fibres. We have fabricated devices with different far-field profiles to determine η_{couple}. Figure 4-7 presents lens-less coupling efficiency experiments on 0.32 NA and 0.5 NA SI PMMA-POFs. Coupling efficiencies are about 40 %, 30 % and 20 % with θ_{max} of 0°, 30° and 45°, respectively. It can be seen in Figure 4-7 that for the initial dual-lobed emission, η_{couple} improves, as I is increased. This is due to the narrowing of the far-field when λ_{det} decreases. In the single-lobed case the overall emitted power is smaller than that of a high-divergent beam. Therefore, in order to maximise the output power at the fibre end, the emission angle must be properly adjusted according the NA of the fibre.

Furthermore, we investigated the alignment tolerance of bare RCLEDs with a ∅0.9-mm SI PMMA-POF as a function of longitudinal and lateral displacement. It was found that misalignment as high as ±0.5 mm still resulted in a relatively good η_{couple}[188], which indicated that our RCLED / POF concept works well without any auxilary optics. The coupling tolerances for smaller than ∅100-µm emitters were determined mostly by the fibre, because the results were not much affected by the emitter size. To further enhance η_{couple}, diffractive optical elements or advanced device packages could be used to tailor the beam shape to fit better to NA of the fibre.

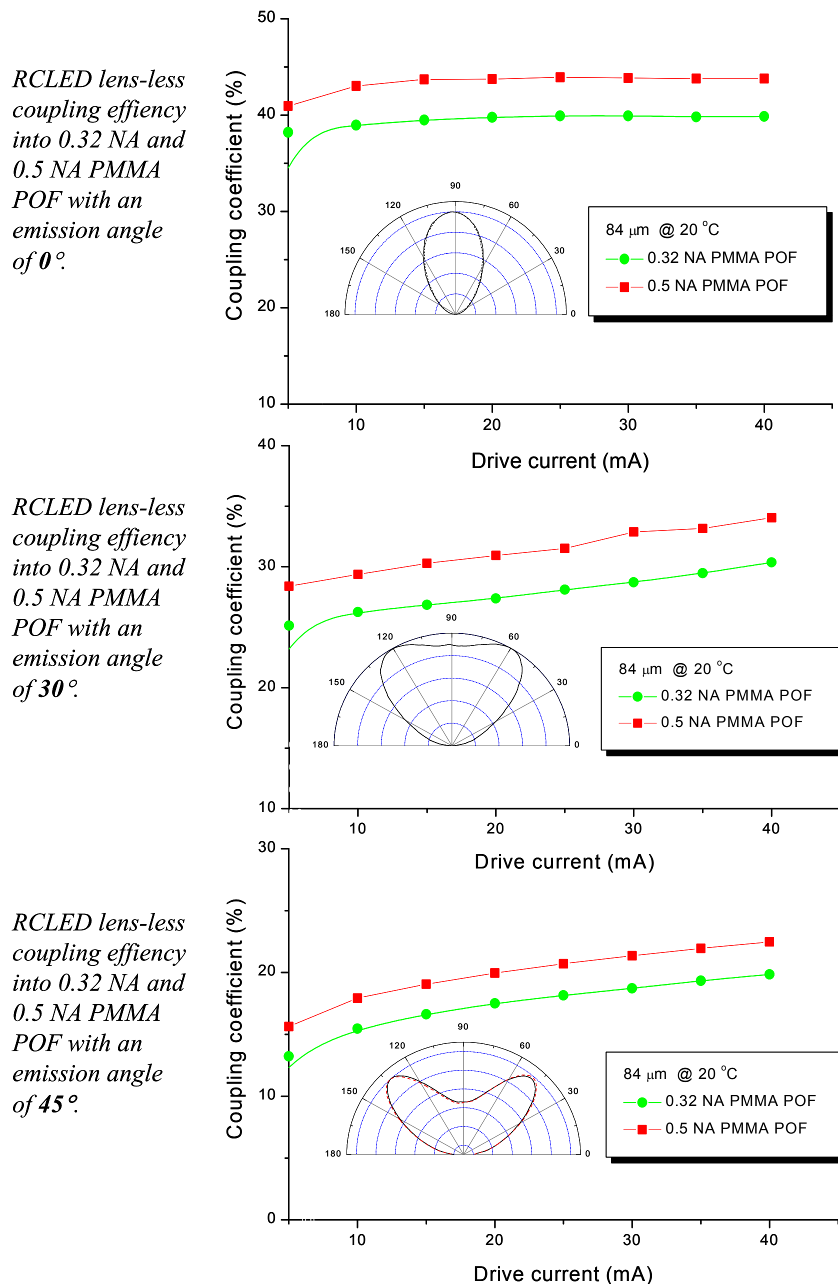

Figure 4-7. *RCLED lens-less coupling efficiency experiment for 0.32 NA and 0.5 NA PMMA-POF. Insets show far-field patterns of the RCLEDs.*

For controlling the light beam, one should be able to focus it, collimate, split, *etc*. Integrating a diffractive optical element (DOE)[189] with the VCSEL or RCLED would be the most elegant way of lens-less beam controlling. DOE can be used to convert the light beam into a spot array in the diffraction plane and be exploited in many applications, for example, in fan-outs of an optoelectronic multi-chip module (MCM)[190].

The beam control of an RCLED is particularly challenging. This is because the shape of the beam varies as a function of drive current and temperature and the coherence length is short. A detail optical characterisation of the device and evolution of a beam distribution from a near-field pattern to a far-field pattern is mandatory for an appropriate design of DOE. Utilisation of DOEs in our RCLEDs is being investigated currently.

4.2 VCSELs

Our preliminary VCSEL operated at 665 nm and had about 15-mA threshold current in pulsed mode, launching $P_{out} \approx 0.2$ mW in RT. CW operation was obtained for VCSELs at somewhat longer wavelength. In the following we summarise our main observations.

4.2.1 Output characteristics

A 690-nm VCSEL having a 10-µm window diameter exhibited a threshold current of 1.3 mA and P_{out}(CW) = 0.56 mW taken at 5.0 mA at RT. A peak value of η_e was 6.4 %. Figure 4-8 shows the forward voltage and light output curves for $^{\varnothing}$8-µm, $^{\varnothing}$10-µm and $^{\varnothing}$15-µm devices as well as spectra of a $^{\varnothing}$15-µm VCSEL. After certain injection currents, output power saturates and starts to decrease, due to thermal roll-over. The spectra are multimodal, even if their fine structures are not perceptible due to the measurement optics.

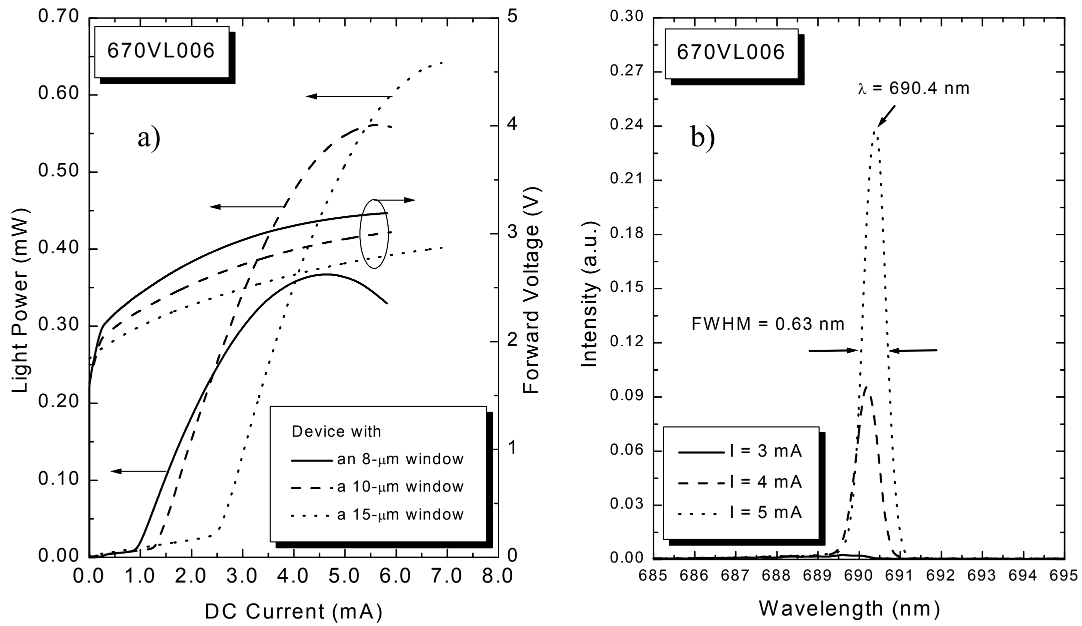

Figure 4-8. *a) Forward voltages and output light power graphs for different emitter window sizes of a 690-nm VCSEL (sample code 670VL006) at RT. b) Emission spectra of a ∅15-µm device taken at 3, 4, and 5 mA (CW, RT).*

Output characteristics were investigated as a function of ambient temperature in CW operation mode. The ∅10-µm device showed a lasing action up to 45 °C[191], and threshold current changed from 0.9 mA at 5 °C to 3.4 mA at 45 °C, which corresponded to characteristics temperature (T_0) of 30 K, which is low compared to AlGaInP EELs with T_0 in excess of 100 K[192].

P_{out} of our VCSEL was limited most likely by the very high reflectivity of the output-coupling DBR, which also contributed to the relatively low threshold current observed. An increase in Al-content of the spacer layers in a cavity with x up to, say, 70 % in $(Al_xGa_{1-x})_{0.51}In_{0.49}P$ would almost certainly improve the performance, but we have not attempted experiments on so high x.

Thickness of the oxide-aperture layer was $\lambda_0/4n$. The aperture was not optimised[193,194] in terms of thickness, location, and shape, which likely caused diffractive and scattering losses. Instead, a thin parabolically tapered aperture (like an ideal lens) could compensate the diffraction of the mode and eliminate scattering loss. Results obtained lately by other authors have shown that the oxide aperture significantly influences the overall device behaviour[195]. Improvement from rather poor pulsed operation to excellent CW operation by adding a properly designed oxide-aperture has been impressive[196,197]. The latest red VCSEL results from various research groups are compiled in Table 4-3.

It was mentioned above in Section 4.1.3 that several mechanisms occurring in RCLEDs cause a degradation of performance characteristics at elevated temperatures. Yet, temperature variations are smaller for RCLEDs than for VCSELs at the same

wavelength. This is because the RCLED escape window has a broad overlap with the QW emission spectrum, in sharp contrast to the case of a VCSEL; giving rise to a weaker dependence of P_{out} on temperature.

Table 4-3. *Compilation of characteristics of red VCSELs (* = no data available).*

20 °C, CW Group/company	*Year*	*Method*	*λ (nm)*	*ϕ (μm)*	*I_{th} (mA)*	*V_{op} (V)*	*P_{max} (mW)*	*η_e (%) peak*	*Remarks*	*Ref.*
BREDSELS	2000	MOCVD	665	18	5.2	2.4	1.1	14	Ox. aperture	194
Chalmers University of Technology	2001	*	670	10	1.1	2.2	1.5	*	Ox. aperture	135
Chiao Tung University	1993	MOCVD	670	15	12¤	*	*	*	Implanted ¤ pulsed current	198
Ferdinand-Braun-Institute	2000	MOCVD	654	*	*	*	*	*	Lowest J_{th} = 2.8 kA/cm^2, pulsed	199
	2001	MOCVD	650	13	3	*	3.1	14	Ox. aperture	197
FireComms	2001	*	670	*	0.3	2.9	1.0	*	Typical values	133
	2002	*	670	4	0.25	2.9	1.0	*	Single-mode, ox-aperture	200
Hewlett-Packard/Agilent	2000	MOCVD	670	*	*	*	0.55	*	Ox. aperture	201
Honeywell	2002	*	673	*	1.5	2.4	1.5	*	Preliminary	202
ORC/TUT	**2000**	**SSMBE**	**690**	**10**	**1.3**	**2.4**	**0.56**	**6.4**	**Ox. aperture**	203
Sandia National Laboratories	1995	MOCVD	676	20	4.2	2.4	2.9	9.0	Implanted	204
	1995	MOCVD	688	30	11.7	2.4	8.2	11	Implanted, planar	205
	1995	MOCVD	687	10	2.3	2.5	1.9	9.6	Implanted, planar	204
	2000	MOCVD	652	*	*	*	0.4	*	Single-mode	206
Toshiba	2001	MOCVD	666	15	2.5	2.7	1.0	*	Implanted	207
University of Sheffield	1996	MOCVD	646	26	60¤	*	1.0¤	*	¤pulsed current	208
University of Stuttgart	2000	MOCVD	675	40	9	*	0.15	*	No aperture	209
Zarlink Semiconductor	2000	MOCVD	670	*	*	2.3	1.8	*	Ox. aperture	210

4.2.2 Reliability

We have not yet studied reliability features of red VCSELs in any great detail, but it is known in general that lasing features degrade rapidly during the first 100 hours[211]. In the very beginning of aging tests P_{out} is improved, due to bias-induced burn-in[211], but the overall performance remains unacceptable for high-T operations above $T \approx 80$ °C. Lately, rather stable operation of 675-nm VCSELs over 3000 hours has been demonstrated[129].

Aging of our preliminary VCSEL is described in Appendix 10. Though only one laser has been studied so far at relatively low $P_{out} \sim 0.5$ mW at RT set in the beginning of the aging test (Figure 4-9), and no reasonable prediction for lifetime can be given, we are inclined to believe that useful lifetime of our 690-nm VCSELs driven at $0.5 \leq P_{out} \leq 1$ mW at RT would be thousands of hours.

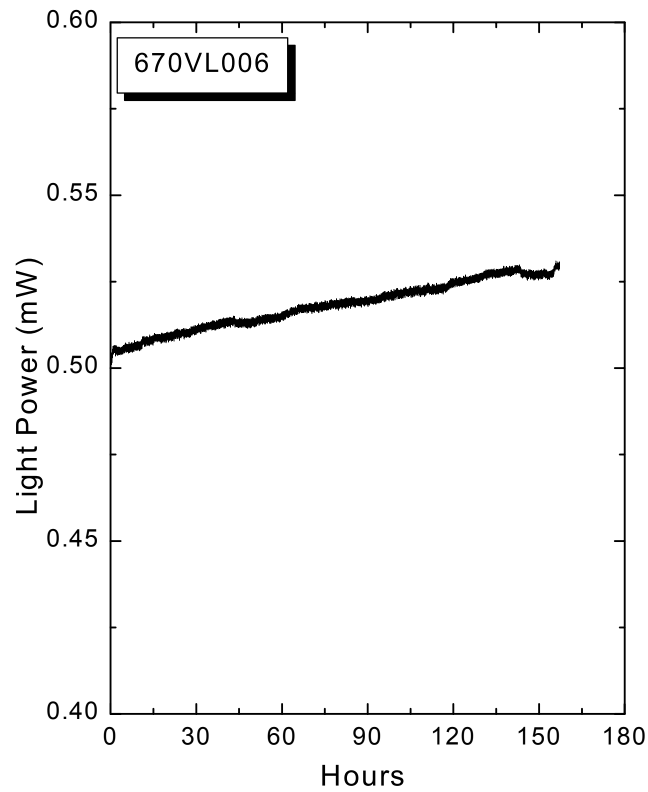

Figure 4-9. *Behaviour of our 690-nm VCSEL (sample code 670VL006) under continuous wave operation for 150 hours.*

5. Final remarks

This Thesis is concerned with the research and development of vertical-cavity light emitters, RCLEDs and VCSELs, in the visible spectral range.

Our main objectives were to develop high-quality short-wavelength (red) light sources grown by SSMBE, and to assess the device performance features. The Author's impression is that the goals were achieved to a large extent. This research also played a seminal role in generating RCLED-related industrial activities in Finland.

My work focussed on epitaxial crystal growth and characterisation of short-wavelength RCLEDs and VCSELs. I believe that this work is among the first ones that provided clear-cut evidence that preparing state-of-the-art phosphorus-containing devices with vertical geometry is feasible by SSMBE. It should also be noted that issues on thermal properties and operational reliability of red RCLEDs were not addressed to any extent at the beginning of this work.

The fibre coupling efficiency was also studied. We found that if the output beam shape of an RCLED is designed properly the alignment tolerances are very wide allowing for low-cost coupling of an RCLED with a standard SI PMMA-POF.

Consumer electronics markets, data transmission over short distances in domestic data handling, and vehicle industry possess an enormous growth potential for POFs. However, for example the 'fibre-to-the-home' concept has been the question at issue for years and it has not been realised as yet. On the other hand, fibre-based data buses in cars are recognised to be an obvious choice and they are about to enter the volume production market.

The big open question concerning a success of the POF technology is how soon the advanced perfluorinated (PF) POFs enter the market. If their pricing were competitive with silica fibres, their usage would likely reduce the importance of the red light emitters, because PF-POFs are operational over a wide spectral range, in particular, on the IR for which RCLEDs and VCSELs can be prepared relatively simply.

To the best of my knowledge, our VCSEL (λ = 690 nm) may be the first ever grown by SSMBE at this wavelength. There is no serious fundamental problem, in principle, that would prevent pushing the lasing wavelength of VCSELs grown by SSMBE down to 630 nm or so.

Achieving conditions for the QW exciton / F-P cavity resonance as well as closely controlling wet thermal oxidation of AlGaAs to form current apertures are seen to be critical issues when considering mass production of red RCLEDs and VCSELs.

In any case, the possibility of on-wafer-testing of RCLEDs and VCSELs is a very

attractive feature. Many non-destructive methods of wafer characterisation exist today to allow for assessment and further improvement of the material quality of the light sources studied in this Thesis.

References

[1] R. N. Hall, G. E. Fenner, J. Kingsley, T. J. Soltys, and R. O. Carlson, 'Coherent light emission from GaAs junctions', *Phys. Rev. Lett.*, **9**, 366 (1962)

[2] T. M. Quist, R. H. Rediker, R. J. Keyes, W. E. Krag, B. Lax, A. L. McWhorter, and H. J. Zeiger, 'Semiconductor maser of GaAs', *Appl. Phys. Lett.*, **1**, 62 (1962)

[3] H. Soda, K. Iga, C, Kitahara, and Y. Suematsu, 'GaInAsP/InP surface emitting lasers', *Jpn. J. Appl. Phys.*, **18**, 2329 (1979)

[4] A. Ibaraki, K. Kawahima, K. Furusawa, T. Ishikawa, T. Yamaguchi, and T. Niina, 'Buried heterostructure GaAs/GaAlAs distributed Bragg reflector surface emitting laser with very low threshold (5.2 mA) under room temperature CW conditions', *Jpn. J. Appl. Phys.*, **28**, 667 (1989)

[5] J. L. Jewell, J. P. Harbison, A. Scherer, Y. H. Lee, and L. T. Florez, 'Vertical-cavity surface-emitting lasers: design, growth, fabrication, characterization', *IEEE J. Quantum Electron.*, **27**, 1332 (1991)

[6] F. H. Peters and M. H. MacDougal, 'High-speed high-temperature operation of vertical-cavity surface-emitting lasers', *IEEE Photon. Technol. Lett.*, **13**, 645 (2001)

[7] K. D. Choquette and H. Q. Hou, 'Vertical-cavity surface emitting lasers: moving from research to manufacturing', *IEEE Proceedings*, **85**, 1730 (1997)

[8] Y. Ohiso, C. Amano, Y. Itoh, K. Tateno, T. Tadokoro, H. Takenouchi, and T. Kurokawa, '1.55 μm vertical-cavity surface-emitting lasers with wafer-fused GaInAsP/InP-GaAs/AlGaAs DBRs', *Electron. Lett.*, **32**, 1483 (1996)

[9] M. Kondow, S. Nakatsuka, T. Kitatani, Y. Yazawa, and M. Okai, 'Room-temperature pulsed operation of GaInNAs laser diodes with excellent high-temperature performance', *Jpn. J. Appl. Phys.*, **35**, 5711 (1996)

[10] K. Nakahara, K. Kondow, T. Kitatani, Y. Yazawa, and K. Uomi, 'Continuous-wave operation of long-wavelength GaInNAs/GaAs quantum well laser', *Electron. Lett.*, **32**, 1585 (1996)

[11] M. C. Larson, M. Kondow, T. Kitatani, K. Nakahara, K. Tanura, H. Inoue, and K. Uomi, 'GaInNAs-GaAs long wavelength vertical-cavity surface-emitting laser diodes', *IEEE Photon. Technol. Lett.*, **10**, 188 (1998)

[12] J. A. Lott and R. P. Schneider, Jr., 'Electrically injected visible (639-661 nm) vertical-cavity surface-emitting lasers', *Electron. Lett.*, **29**, 830 (1993)

[13] J. A. Lott, R. P. Schneider, Jr., J. C. Zolper, and K. J. Malloy, 'AlGaInP visible vertical-cavity surface-emitting lasers operating with gain contributions from the n=2 quantum well transition', *Appl. Phys. Lett.*, **63**, 3485 (1993)

[14] B. Tell, R. E. Leibenguth, K. F. Brown-Goebeler, and G. Livescu, 'Short wavelength (699 nm) electrically pumped vertical-cavity surface-emitting lasers', *IEEE Photon. Technol. Lett.,* **4**, 1195 (1992)

[15] J. A. Lott, R. P. Schneider, Jr., K. D. Choquette, S. P. Kilcoyne, and J. J. Figiel, 'Room temperature continuous wave operation of red vertical cavity surface emitting laser diodes', *Electron. Lett.*, **29**, 1693 (1993)

[16] M. Hagerott Crawford, R. P. Schneider, Jr., K. D. Choquette, K. L. Lear, S. P. Kilcoyne, and J. J. Figiel, 'High efficiency AlGaInP-based 660-680 nm vertical-cavity surface emitting lasers', *Electron. Lett.*, **31**, 196 (1995)

[17] M. Hagerott Crawford, R. P. Schneider, Jr., K. D. Choquette, and K. L Lear, 'Temperature-dependent characteristics and single-mode performance of AlGaInP-based 670-690 nm vertical-cavity surface-emitting lasers', *IEEE Photon. Technol. Lett,* **7**, 724 (1995)

[18] J. A. Lehman, R. A. Morgan, D. Carlson, M. Hagerott Crawford, and K. D. Choquette, 'High-frequency modulation characteristics of red VCSELs', *Electron. Lett*., **33**, 298 (1997)

[19] D. M. Kuchta, R. P. Schneider, Jr., K. D. Choquette, and S. Kilcoyne, 'Large- and small-signal modulation properties of red (670 nm) VCSELs', *IEEE Photon. Technol. Lett,* **8**, 307 (1996)

[20] E. F. Schubert, Y. -H. Wang, A. Y. Cho, L. -W. Tu, and G. J. Zydzik, 'Resonant cavity light-emitting diode', *Appl. Phys. Lett.*, **60**, 921 (1992)

[21] J. A. Lott, R. P. Schneider, Jr., G. A. Vawter, J. C. Zolper, and K. J. Malloy, 'Visible (660 nm) resonant cavity light-emitting diodes', *Electron. Lett*., **29**, 328 (1993)

[22] J. A. Lott, R. P. Schneider, Jr., J. C. Zolper, and K. J. Malloy, 'AlGaInP visible resonant cavity light-emitting diodes', *IEEE Photon. Technol. Lett.,* **5**, 631 (1993)

[23] R. Bockstaele, C. Sys, J. Blondelle, B. Dhoedt, I. Moerman, P. van Daele, P. Demeester, and R. Baets, 'Resonant cavity LED's optimized for coupling to polymer optical fibres', *IEEE Photon. Technol. Lett.,* **11**, 158 (1999)

[24] M. Jalonen, J. Köngäs, M. Toivonen, P. Savolainen, S. Orsila, A. Salokatve, and M. Pessa, 'Monolithic 1.3 μm resonant cavity light emitting diode grown by solid source molecular beam epitaxy', *Electron. Lett*., **34**, 1519 (1998)

[25] D. L. Huffaker, C. C. Lin, J. Shin, and D. G. Deppe, 'Resonant cavity light emitting diode with an Al_xO_y/GaAs reflector', *Appl. Phys. Lett*., **66**, 3096 (1995)

[26] H. Jeon, V. Kozlov, P. Kelkar, A. V. Nurmikko, C. –C. Chu, D. C. Grillo, J. Han, G. C. Hua, and R. L. Gunshor, 'Room-temperature optically pumped blue-green vertical cavity surface emitting laser', *Appl. Phys. Lett*., **67**, 1668 (1995)

[27] P. Uusimaa, P. Sipilä, M. Saarinen, L. Toikkanen, A. Rinta-Möykky, and M. Pessa, 'Molecular beam epitaxy growth of MgZnSSe/ZnSSe/CdZnSe microcavity light-emitting diodes using *in situ* reflectance monitoring', *J. Crystal Growth*, **201/202**, 1032 (1999)

[28] K. Streubel, U. Helin, V. Oskarsson, E. Bäcklin, and Å. Johansson, 'High brightness visible (660 nm) resonant-cavity light-emitting diode', *IEEE Photon. Technol. Lett.,* **10**, 1685 (1998)

[29] K. Streubel, and R. Stevens, '250 Mbit/s plastic fibre transmission using 660 nm resonant cavity light emitting diode', *Electron. Lett*., **34**, 1862 (1998)

[30] Appendix 13

[31] Appendix 7

[32] E. F. Schubert, N. E. J. Hunt, R. J. Malik, M. Micovic, and D. L. Miller, 'Temperature and modulation characteristics of resonant-cavity light-emitting diodes', *J. Lightwave Technol*., **14**, 1721 (1996)

[33] M. I. Nathan, W. P. Dumke, G. Burns, F. H. Dill, Jr., and G. Lasher, 'Stimulated emission of radiation from GaAs *p-n* junctions', *Appl. Phys. Lett*., **1**, 62 (1962)

[34] I. Melngailis, 'Longitudinal injection-plasma laser of InSb', *Appl. Phys. Lett*., **6**, 59 (1965)

[35] A. Bergh and H. Saul, U.S. Patent No. 3, 217 (1973)

[36] A. Cho, H. C. Casey, Jr., and P. W. Foy, 'Back-surface emitting $GaAs_xSb_{1-x}$ LEDs (λ = 1.0 μm) prepared by molecular beam epitaxy', *Appl. Phys. Lett.*, **30**, 397 (1977)

[37] K. Iga, S. Ishikawa, S. Ohkouchi, and T. T. Nishimura, 'Room-temperature pulsed oscillation of GaAlAs/GaAs surface-emitting injection laser', *Appl. Phys. Lett.*, **45**, 348 (1984)

[38] K. Kobayashi, S. Kawata, A. Gomyo, I. Hino, and T. Suzuki, 'Room-temperature CW operation of AlGaInP double-heterostructure visible lasers', *Electron. Lett.*, **21**, 931 (1985)

[39] H. Tanaka, Y. Kawamura, and H. Asahi, 'Room-temperature operation of MBE-grown InGaP/InGaAlP MQW visible laser diodes', *Electron. Lett.*, **22**, 707 (1986)

[40] K. Iga, S. Kinoshita, and F. Koyama, 'Microcavity GaAlAs/GaAs surface emitting laser with I_{th} = 6 mA', *Electron. Lett.*, **23**, 134 (1987)

[41] P. L. Gourley and T. J. Drummond, 'Visible, room temperature, surface-emitting laser using an epitaxial Fabry-Perot resonator with AlGaAs/AlAs quarter-wave high-reflectors and AlGaAs/GaAs quantum wells', *Appl. Phys. Lett.*, **50**, 1225 (1987)

[42] Y. H. Lee, B. Tell, K. F. Brown-Goebeler, R. E. Leibenguth, and V. D. Mattera, 'Deep red continuous-wave top-surface-emitting vertical-cavity AlGaAs superlattice lasers', *IEEE Photon. Technol. Lett.*, **3**, 108 (1991)

[43] R. P. Schneider, Jr., R. P. Bryan, J. A. Lott, and E. D. Jones, 'MOVPE growth of AlGaInP/AlGaAs visible vertical-cavity emitting lasers', *J. Crystal Growth*, **124**, 763 (1992)

[44] B. Tell, K. F. Brown-Goebeler, and R. E. Leibenguth, 'Low temperature continuous operation of vertical-cavity surface-emitting lasers with wavelength below 700 nm', *IEEE Photon. Technol. Lett.*, **5**, 637 (1993)

[45] K. F. Huang, K. Tai, C. C. Wu, and J. D. Winn, 'Continuous wave visible InGaP/InAlGaP quantum well surface-emitting laser diodes', *Electron. Lett.*, **29**, 1314 (1993)

[46] S. P. Najda, A. H. Kean, M. D. Dawson, T. Bestwick, and G. Duggan, 'An all phosphide 625 nm surface emitting resonant cavity LED', *Sharp Tech. J.*, **65**, 31 (1996)

[47] M. Jalonen, M. Toivonen, J. Köngäs, A. Salokatve, and M. Pessa, 'Oxide-confined resonant cavity red light-emitting diode grown by solid source molecular beam epitaxy', *Electron. Lett.*, **33**, 1989 (1997)

[48] Appendix 8

[49] M. Brunner, K. Gulden, R. Hövel, M. Moser, and M. Ilegems, 'Thermal lensing effects in small oxide confined vertical-cavity surface-emitting lasers', *Appl. Phys. Lett.*, **76**, 7 (2000)

[50] B. J. Thibeault, E. R. Hegblom, Y. A. Akulova, J. Ko, R. Naone, L. A. Coldren, and D. Floyd, 'Electrical and optical losses in dielectrically apertured vertical lasers', *SPIE Proc.*, **3003**, 86 (1997)

[51] E. R. Hegblom, N. M. Margalit, A. Fiore, and L. A. Coldren, 'Small efficient vertical cavity lasers with tapered oxide apertures', *Electron. Lett.*, **34**, 895 (1998)

[52] K. D. Choquette, K. M. Geib, C. I. H. Ashby, R. D. Twesten, O. Blum, H. Q. Hou, D. M. Follstaedt, B. E. Hammons, D. Mathes, and R. Hull, 'Advances in Selective Wet Oxidation of AlGaAs Alloys**'**, *IEEE J. Selected Topics in Quantum Electron.*, **3**, 916 (1997)

[53] H. Nickel, 'A detailed experimental study of the wet oxidation kinetics of $Al_xGa_{1-x}As$ layers', *J. Appl. Phys.*, **78**, 5201 (1995)

[54] M. H. MacDougal, and P. D. Dapkus, 'Wavelength shift of selectively oxidized Al_xO_y-AlGaAs-GaAs distributed Bragg reflectors', *IEEE Photon. Technol. Lett.*, **9**, 884 (1997)

[55] R. D. Twesten, D. M. Follstaedt, K. D. Choquette, and R. P. Schneider, Jr., 'Microstructure of laterally oxidized $Al_xGa_{1-x}As$ layers in vertical-cavity lasers', *Appl. Phys. Lett.*, **69**, 19 (1996)

[56] M. Miller, M. Grabherr, R. Jäger, and K. J. Ebeling, 'High-power VCSEL arrays for emission in the watt regime at room temperature', *IEEE Photon. Technol. Lett.*, **13**, 173 (2001)

[57] E. W. Young, K. D. Choquette, S. L. Chuang, K. M. Geib, A. J. Fischer, and A. A. Allerman, 'Single-transverse-mode vertical-cavity lasers under continuous and pulsed operation', *IEEE Photon. Technol. Lett.*, **13**, 927 (2001)

[58] R. Windisch, P. Heremans, A. Knobloch, P. Kiesel, G. H. Döhler, B. Dutta, and G. Borghs, 'Light-emitting diodes with 31% external quantum efficiency by outcoupling of lateral waveguide modes', *Appl. Phys. Lett.*, **74**, 2256 (1999)

[59] M. R. Krames, M. Ochiai-Holcomb, G. E. Höfler, C. Carter-Coman, E. I. Chen, I.-H. Tan, P. Grillot, N. F. Gardner, H. C. Chui, J. -W. Huang, S. A. Stockman, F. A. Kish, M. G. Craford, T. -S. Tan, C. P. Kocot, M. Hueschen, J. Posselt, B. Loh, G. Sasser, and D. Collins, 'High-power truncated-inverted-pyramid $(Al_xGa_{1-x})_{0.5}In_{0.5}P$/GaP light-emitting diodes exhibiting >50% external quantum efficiency', *Appl. Phys. Lett.*, **75**, 2365 (1999)

[60] H. Karstense and K. Drögemüller, 'Loss analysis of laser diode to single-mode fibre couplers with glass spheres or silicon plano-convex lenses', *J. Lightwave Technol.*, **8**, 739 (1990)

[61] E. –H. Park, M. –J. Kim, and Y. –S. Kwon, 'Microlens for efficient coupling between LED and optical fibre', *IEEE Photon. Technol. Lett.*, **11**, 439 (1999)

[62] W. W. Chow, K. D. Choquette, M. H. Crawford, K. L. Lear, and G. R. Hadley, 'Design, fabrication, and performance of infrared and visible vertical-cavity surface-emitting lasers', *IEEE J. Quantum Electron.*, **33**, 1810 (1997)

[63] C. T. H. F. Leidenbaum, A. Valster, A. L. G. J. Severens, and G. W. Hooft, 'Determination of the GaInP/AlGaInP band offset', *Appl. Phys. Lett.*, **57**, 2698 (1990)

[64] D. P. Bour, 'AlGaInP quantum well lasers', Ch. 9, *Quantum well lasers*, P. S. Zory, Jr., ed., Academic Press, San Diego (1993)

[65] S. J. Sweeney, G. Knowles, and T. Sale, 'Evaluating the continuous-wave performance of AlGaInP-based red (667 nm) vertical-cavity surface-emitting lasers using low-temperature and high-pressure techniques', *Appl. Phys. Lett.*, **78**, 865 (2001)

[66] M. C. P. M. Krijn, 'Heterojunction band offsets and effective masses in III-V quaternary alloys', *Semicon. Sci. Technol.*, **6**, 27 (1991)

[67] R. P. Schneider, Jr., J. A. Lott, M. Hagerott Crawford, and K. D. Choquette, 'Epitaxial design and performance of AlGaInP red (650-690 nm) VCSELs', Ch., *Current trends in vertical cavity surface emitting lasers*, T. P. Lee, ed., World Scientific Publishing, Danvers (1995)

[68] L. A. Coldren and E. R. Hegblom, 'Fundamental issues in VCSEL design', Ch.2, 'Vertical-cavity surface-emitting lasers', C. Wilmsen, H. Temkin, and L. A. Coldren, ed., Cambridge University Press, U.K. (1999)

[69] F. Bugge, G. Beister, G. Erbert, S. Gramlich, K. Vogel, U. Zeimer, and M. Weyers, 'GaInP/AlGaAs/GaAs laser diodes with high output power', *Inst. Phys. Conf. Ser.*, **155**, 573 (1997)

[70] J. E. Fouquet, V. M. Robbins, S. J. Rosner, and O. Blum, 'Unusual properties of photoluminescence from partially ordered GaInP', *Appl. Phys. Lett.*, **57**, 1566 (1990)

[71] R. G. Alonso, A. Mascarenhas, G. S. Horner, K. A. Bertness, S. R. Kurtz, and J. M. Olson, 'Spontaneous ordering in $GaInP_2$: a polarized-piezomodulated-reflectivity study', *Phys. Rev. B*, **48**, 11833 (1993)

[72] S. H. Wei and A. Zunger, 'Band-gap narrowing in ordered and disordered semiconductor alloys', *Appl. Phys. Lett.*, **56**, 662 (1990)

[73] L. C. Su, I. H. Ho, and G. B. Stringfellow, 'Control of ordering in $Ga_{0.5}In_{0.5}P$ using growth temperature', *J. Appl. Phys.*, **76**, 3520 (1994)

[74] Y. S. Chun, H. Murata, T. C. Hsu, I. H. Ho, L. C. Su, Y. Hosokawa, and G. B. Stringfellow, 'Effects of V/III ratio on ordering in GaInP: atomic scale mechanisms', *J. Appl. Phys.*, **79**, 6900 (1996)

[75] G. S Chen, D. H. Jaw, and G. B. Stringfellow, 'Effects of substrate misorientation on ordering in $GaAs_{0.5}P_{0.5}$ grown by organometallic vapor phase epitaxy', *Appl. Phys. Lett.*, **57**, 2475 (1990)

[76] G. W. Wicks, M. W. Koch, J. A. Varriano, F. G. Johnson, C. R. Wie, H. M. Kim, and P. Colombo, 'Use of a valved, solid phosphorus source for the growth of $Ga_{0.5}In_{0.5}P$ and $Al_{0.5}In_{0.5}P$ by molecular beam epitaxy', *Appl. Phys. Lett.*, **59**, 342 (1991)

[77] K. Tappura, J. Aarik, and M. Pessa, 'High-power GaInP-AlGaInP quantum-well lasers grown by solid source molecular beam epitaxy', *IEEE Photon. Technol. Lett.*, **8**, 319 (1996)

[78] D. P. Bour, D. W. Treat, R. L. Thornton, R. S. Geels, and D. F. Welch, 'Drift leakage current in AlGaInP lasers', *IEEE J. Quantum Electron.*, **29**, 1337 (1993)

[79] M. Kondo, C. Anayama, H. Sekiguchi, and T. Tanahashi, 'Mg-doping transients during metalorganic vapor phase epitaxy of GaAs and AlGaInP', *J. Cryst. Growth*, **141**, 1 (1994)

[80] R. Mosca, S. Franchi, P. Frigeri, E. Gombia, A. Carnera, and M. Peroni, 'Influence of the As/Ga flux ratio on diffusion of Be in MBE GaAs layers', *Mater. Sci. Eng. B*, **80**, 32 (2001)

[81] E. Yablonovitch, T. J. Gmitter, and R. Bhat, 'Inhibited and enhanced spontaneous emission from optically thin AlGaAs/GaAs double heterostructures', *Phys. Rev. Lett.*, **61**, 2546 (1988)

[82] D. V. Kuksenkov, H. Temkin, K. L. Lear and H. Q. Hou, 'Spontaneous emision factor in oxide confined vertical-cavity lasers', *Appl. Phys. Lett.*, **70**, 13 (1997)

[83] D. S. Citrin, 'Controlled exciton spontaneous emission in optical-microcavity-embedded quantum wells', *IEEE J. Quantum Electron.*, **30**, 997 (1994)

[84] C. Weisbuch, M. Nishioka, A. Ishikawa, and Y. Arakawa, 'Observation of the coupled exciton-photon mode splitting in a semiconductor quantum microcavity', *Phys. Rev. Lett.*, **69**, 3314 (1992)

[85] G. Björk, 'On the spontaneous lifetime change in an ideal planar microcavity – transition from a mode continuum to quantized modes', *IEEE J. Quantum Electron.*, **30**, 2314 (1994)

[86] R. J. Ram, D. I. Babic, R. A. York, and J. E. Bowers, 'Spontaneous emission in microcavities with distributed mirrors', *IEEE Quantum Electron.*, **31**, 399 (1995)

[87] I. Abram, I. Robert, and R. Kuszelewicz, 'Spontaneous emission control in semiconductor microcavitites with metallic or Bragg mirrors', *IEEE J. Quantum Electron*., **34**, 71 (1998)
[88] T. J. Rogers, D. G. Deppe, and B. G. Streetman, 'Effect of an AlAs/GaAs mirror on the spontaneous emission of an InGaAs-GaAs quantum well', *Appl. Phys. Lett*., **57**, 1858 (1990)
[89] E. F. Schubert and N. E. J. Hunt, 'Enhancement of spontaneous emission in microcavities', Ch. 3, 'Vertical-cavity surface-emitting lasers', C. Wilmsen, H. Temkin, and L. A. Coldren, ed., Cambridge University Press, U.K. (1999)
[90] A. M. Vredenberg, N. E. J. Hunt, E. F. Schubert, D. C. Jacobson, J. M. Poate, and G. J. Zydzik, 'Controlled atomic spontaneous emission from Er^{3+} in a transparent Si/SiO_2 microcavity', *Phys. Rev. Lett*., **71**, 517 (1993)
[91] N. E. J. Hunt, E. F. Schubert, R. F. Kopf, D. L. Sivco, A. Y. Cho, and G. J. Zydzik, 'Increased fibre communications bandwidth from a resonant cavity light-emitting diode emitting at $\lambda = 940$ nm', *Appl. Phys. Lett*., **63**, 2600 (1993)
[92] H. Benisty, H. De Neve, and C. Weisbuch, 'Impact of planar microcavity effects on light extraction – Part I: basic concepts and analytical trends', *IEEE J. Quantum Electron*., **34**, 1612 (1998)
[93] C. Dill, R. P. Stanley, U. Oesterle, D. Ochoa, and M. Ilegems, 'Effect of detuning on the angular emission pattern of high-efficiency microcavity light emitting diodes', *Appl. Phys. Lett*., **73**, 799 (1998)
[94] M. Brunner, K. Gulden, R. Hövel, M. Moser, J. F. Carlin, R. P. Stanley, and M. Ilegems, 'Continuous-wave dual-wavelength lasing in a two-section vertical-cavity laser', *IEEE Photon. Technol. Lett*., **12**, 1316 (2000)
[95] A. J. Fischer, W. W. Chow, K. D. Choquette, A. A. Allerman, and K. M. Geib, 'Q-switched operation of a coupled-resonator vertical-cavity laser diode', *Appl. Phys. Lett*., **76**, 1975 (2000)
[96] C. –L. Wang and C. –L. Pan, 'Tunable multiteraherz beat signal generation from a two-wavelength laser-diode array', *Opt. Lett*., **20**, 1292 (1995)
[97] A. J. Fischer, K. D. Choquette, W. W. Chow, A. A. Allerman, and K. M. Geib, 'Bistable output from a coupled-resonator vertical-cavity laser diode', *Appl. Phys. Lett*., **77**, 3319 (2000)
[98] A. J. Fischer, K. D. Choquette, W. W. Chow, A. A. Allerman, D. K. Serkland, and K. M. Geib, 'High single-mode power observed from a coupled-resonator vertical-cavity laser diode', *Appl. Phys. Lett*., **79**, 4079 (2001)
[99] P. N. Stavrinou, M. Whitehead, G. Parry, and C. C. Button, 'Angular spectrum of visible resonant cavity light-emitting diodes', *J. Appl. Phys*., **86**, 3475 (1999)
[100] J. W. Gray, R. F. Oulton, P. N. Stavrinou, M. Whitehead, G. Parry, G. Guggan, R. C. Coutinho, and D. R. Selviah, 'Angular emission profiles and coherence length measurements of highly efficient, low voltage resonant cavity light emitting diodes operating around 650 nm', *SPIE Proc*., **4278**, 81 (2001)
[101] Appendix 4
[102] C. H. Chen, M. Hargis, J. M. Woodall, M. R. Melloch, J. S. Reynols, E. Yablonovitch, and W. Wang, 'GHz bandwidth GaAs light-emitting diodes', *Appl. Phys. Lett*., **74**, 3140 (1999)
[103] K. Hild, T. E. Sale, T. J. C. Hosea, M. Hirotani, Y. Mizuno, and T. Kato, 'Spectral and thermal properties of red AlGaInP RCLEDs for polymer optical fibre applications', *IEE Proc. Optoelectron*., **148**, 220 (2001)

[104] A. K. Dutta, 'Prospects of highly efficient AlGaInP based surface emitting type ring-LED for 50 and 156 Mb/s POF data link systems', *J. Lightwave Technol.*, **16**, 106 (1997)
[105] J. Dekker, A. Tukiainen, N. Xiang, S. Orsila, M. Saarinen, M. Toivonen, and M. Pessa, 'Annealing of the deep recombination center in GaInP/AlGaInP quantum wells grown by solid-source molecular beam epitaxy', *J. Appl. Phys.*, **86**, 3709 (1999)
[106] Z. C. Huang, C. R. Wie, J. A. Varriano, M. W. Koch, and G. W. Wicks, 'Phosphorus-vacancy-related deep levels in GaInP layers', *J. Appl. Phys.*, **77**, 1587 (1995)
[107] M. Jalonen, M. Toivonen, P. Savolainen, J. Köngäs, and M. Pessa, 'Effects of rapid thermal annealing on GaInP/AlGaInP lasers growth by all-solid-source molecular beam epitaxy', *Appl. Phys. Lett.*, **71**, 479 (1997)
[108] K. Panzer, G. Müller, H. Hurt, and C. Thiel, 'From D2B to MOST', *Components*, **1**, 23 (1999)
[109] *http://www.oasis.de/*
[110] A. Z. Einstein, 'On the quantum theory of radiation', *Physikalishe Zeitschrift*, **18**, 121 (1917)
[111] G. Hasnain, K. Tai, L. Yang, Y. H. Wang, R. J. Fischer, J. D. Wynn, B. Weir, N. K. Dutta, and A. Y. Cho, 'Performance of gain-guided surface emitting lasers with semiconductor distributed Bragg reflectors', *IEEE J. Quantum Electron.*, **27**, 1377 (1991)
[112] Y. H. Lee, A. Chavez-Pirson, S. W. Koch, H. M. Gibbs, S. H. Park, J. Morhange, A. Jeffery, N. Peyghambarian, L. Banyai, A. C. Gossard, and W. Wiegmann, 'Room-temperature optical nonlinearities in GaAs', *Phys. Rev. Lett.*, **57**, 2446 (1986)
[113] R. Jin, D. Boggavarapu, G. Khitrova, H. M. Gibbs, Y. Z. Hu, S. W. Koch, and N. Peyghambarian, 'Linewidth broadening factor of a microcavity semiconductor laser', *Appl. Phys. Lett.*, **61**, 1883 (1992)
[114] W. E. Lamb, Jr., 'Theory of an optical maser', *Phys. Rev. A.*, **134**, 1429 (1964)
[115] K. Iga and F. Koyama, 'Surface-emitting lasers', Ch. 5, *Semiconductor lasers II – Materials and structures*, E. Kapon, ed., Academic Press (1998)
[116] H. Martinsson, J. A. Vukusic, M. Grabbherr, R. Michalzik, R. Jager, K. J. Ebeling, and A. Larsson, 'Transverse mode selection in large-area oxide-confined vertical-cavity surface-emitting lasers using a shallow surface relief', *IEEE Photon. Technol. Lett.*, **11**, 1536 (1999)
[117] A. K. Jansen van Doorn, M. P. van Exter, and J. P. Woerdman, 'Elastooptic anisotropy and polarisation orientation of VCSELs', *Appl. Phys. Lett.*, **69**, 1041 (1996)
[118] L. Plouzennec, 'Polarization gain dependence of vertical-cavity surface-emitting lasers: phenomenological modeling and experiments', *J. Appl. Phys.*, **87**, 2649 (2000)
[119] C. J. Hasnain, J. P. Harbison, L. T. Florez, and N. G. Stoffel, 'Polarization characteristics of quantum well vertical cavity surface emitting lasers', *Electron. Lett.*, **27**, 163 (1991)
[120] A. Valle, L Pesquera, and K. S. Shore, 'Polarization behaviour of birefringent multitransverse mode vertical-cavity surface emitting lasers', *IEEE Photon. Technol. Lett.*, **9**, 557 (1997)

[121] K. Panajotov, B. Ryvkin, J. Danckaert, M. Peeters, H. Thienpont, and I. Veretennicoff, ‘Polarization switching in VCSELs due to thermal lensing’, *IEEE Photon. Technol. Lett.*, **10**, 6 (1998)
[122] M. San Miguel, O. Feng, and J. V. Moloney, ‘Light-polarization dynamics in surface-emitting semiconductor lasers’, *Phys. Rev. A*, **52**, 1728 (1996)
[123] B. Ryvkin, K. Panajotov, A. Georgievski, J. Danckaert, M. Peeters, G. Verschaffelt, H. Thienpont, and I. Veretennicoff, ‘The effect of photon energy dependent loss and gain mechanisms on polarization switching in vertical-cavity surface-emitting lasers’, *J. Opt. Soc. Am. B.*, **16**, 2106 (1999)
[124] G. Verschaffelt, J. Albert, I. Veretennicoff, J. Danckaert, S. Barbay, G. Giacomelli, and F. Marin, ‘Frequency response of current-driven polarization modulation in vertical-cavity surface-emitting lasers’, *Appl. Phys. Lett.*, **80**, 2248 (2002)
[125] Y. H. Chen, C. I. Wilkinson, J. Woodhead, C. C. Button, J. P. R. David, M. A. Pate, and P. N. Robson, ‘Polarisation characteristics of InGaAlP/AlGaAs visible vertical cavity surface emitting lasers’, *Electron. Lett.*, **32**, 559 (1996)
[126] M. S. Park, B. T Ahn, B. –S. Yoo, H. Y. Chu, H. –H. Park, and C. J. Chang-Hasnain, ‘Polarization control of vertical-cavity surface-emitting lasers by electro-optic birefringence’, *Appl. Phys. Lett.*, **76**, 813 (2000)
[127] J. D. Lambkin, ‘Red VCSEL technology’, article in *Compound Semiconductor*, 6, 65 (2000)
[128] ESPRIT long term research programme BREDSELS-23455 *Bright red surface emitting lasers*, supported by the European Commission, article in *Compound Semiconductor*, **6**, 65 (2000)
[129] R. Pu, C. W. Wilmsen, K. M. Geib, and K. D. Choquette, ‘Thermal resistance of VCSEL’s bonded to integrated circuits’, *IEEE Photon. Technol. Lett.*, **11**, 1554 (1999)
[130] B. J. Thibeault, K. Bertilsson, E. R. Hegblom, E. Strzelecka, P. D. Floyd, R. Naone, and L. A. Coldren, ‘High-speed characteristics of low-optical loss oxide-apertured vertical-cavity lasers’, *IEEE Photon. Technol. Lett.*, **9**, 11 (1997)
[131] HFE6X90-001 VCSEL Data Sheet at *http://www.honeywell.com*
[132] F. H. Peters and M. H. MacDougal, ‘High-speed high-temperature operation of vertical-cavity surface-emitting lasers’, *IEEE Photon. Technol. Lett.*, **13**, 645 (2001)
[133] FC200-01 VCSEL Data Sheet 13-11-2001 at *http://www.firecomms.com*
[134] I. Takaaki, E. Nihei, and Y. Koike, ’Graded index polymer fibre for high-speed data communication’, *Appl. Optics*, **33**, 4261 (1994)
[135] C. Carlsson, H. Martinsson, J. Vukusic, J. Halonen, and A. Larsson, ‘Nonlinear distortion and dynamic range of red (670 nm) oxide confined VCSELs’, *IEEE Photon. Technol. Lett.*, **13**, 358 (2001)
[136] Y. Koike and T. Ishigure, ‘High-speed, low-loss polymer optical fibre’, Workshop on mechanical reliability of polymer materials and plastic packages of IC devices, *EEP*, **25**, 19 (1998)
[137] T. Ishigure, A. Horibe, E. Nihei, and Y. Koike, ‘High-bandwidth, high-numerical aperture graded-index polymer optical fibre’, *J. Lightwave Technol.*, **13**, 1686 (1995)
[138] G. Jiang, R. F. Shi, and A. F. Garito, ‘Mode coupling and equilibrium mode distribution conditions in plastic optical fibres’, *IEEE Photon. Technol. Lett.*, **9**, 1128 (1997)

[139] H. Kosaka, M. Kajita, M. Yamada, Y. Sugimoto, K. Kurata, T. Tanabe, and Y. Kasukawa, 'Plastic-based receptacle-type VCSEL-array modules with one and two dimensions fabricated using the self-alignment mounting technique', *Proc. Electron. Comp. Technol. Conf. (ECTC)*, **47**, 382 (1997)
[140] Y. Shimada, Y. Aoki, and K. Iga, 'Parallel optical-transmission module using vertical-cavity surface-emitting laser array and micro-optical bench (MOB)', *Jpn. J. Appl. Phys*., **40**, 114 (2001)
[141] T. Ouchi, A. Imada, T. Sato, and H. Sakata, 'Direct coupling of VCSELs to plastic optical fibres using guide holes patterned in a thick photoresist', *IEEE Photon. Technol. Lett*., **14**, 263 (2002)
[142] Appendix 7
[143] G. D. Khoe, Y. Koike, T. Ishigure, P. K. van Bennekom, H. P. A. van der Boom, W. Li, and G. Yabre, 'Status of GIPOF systems and related technologies', *ECOC Proc*., **II**, 274 (1999)
[144] T. Ishigure, Y. Koike, and J. W. Fleming, 'Optimum index profile of the perfluorinated polymer-based GI polymer optical fibre and its dispersion properties', *J. Lightwave Technol*., **18**, 178 (2000)
[145] H. L. T. Lee, R. V. Dalal, R. J. Ram, and K. D. Choquette, 'Dynamic range of vertical cavity surface emitting lasers in multimode links', *IEEE Photon. Technol. Lett*., **11**, 1473 (1999)
[146] F. Mederer, R. Jäger, P. Schnitzer, H. Unold, M. Kicherer, K. J. Ebeling, M. Naritomi, and R. Yoshida, 'Multi-Gb/s graded-index POF data link with butt-coupled single-mode InGaAs VCSEL', *IEEE Photon. Technol. Lett*., **12**, 199 (2000)
[147] M. Born and E. Wolf, 'Principles of optics', Pergamon Press, Oxford (1970)
[148] L. A. Coldren and S. W. Corzime, 'Diode lasers and photonic integrated circuits', Wiley, New York (1991)
[149] M. A. Afromovitz, 'Refractive index of $Ga_{1-x}Al_xAs$', *Solid State Comm*. **15**, 59 (1974)
[150] A. Cho, 'Twenty years of molecular beam epitaxy', *J. Crystal Growth*, **150**, 1 (1995)
[151] A. Bhattacharya, M Zorn, A. Oster, M. Nasarek, H. Wenzel, J. Sebastian, M. Weyers, and G. Tränkle, 'Optimization of MOVPE growth for 650 nm-emitting VCSELs, *J. Cryst. Growth*, **221**, 663 (2000)
[152] R. F. Kopf, E. F. Schubert, S. W. Downey, and A. B. Emerson, 'N- and p-type dopant profiles in distributed Bragg reflector structures and their effect on resistance', *Appl. Phys. Lett.*, **61**, 1820 (1992)
[153] Z. Pan, T. Miyamoto, D. Schlenker, F. Koyama, and K. Iga, 'Quality improvement of GaInNAs/GaAs quantum well growth by metalorganic chemical vapor deposition using tertiarybutylarsine', *Jpn. J. Appl. Phys*., **38**, 1012 (1999)
[154] L. Li, B. –K. Han, D. Law, C. H. Li, Q. Fu, and R. F. Hicks, 'A phosphorus-rich structure of InP (001) produced by metalorganic vapor-phase epitaxy', *Appl. Phys. Lett*., **75**, 683 (1999)
[155] G. W. Wicks, M. W. Koch, J. A. Varriano, F. G. Johnson, C. R. Wie, H. M. Kim, and P. Colombo, 'Use of a valved, solid phosphorus source for the growth of $Ga_{0.5}In_{0.5}P$ and $Al_{0.5}In_{0.5}P$ by molecular beam epitaxy', *Appl. Phys. Lett*., **59**, 342 (1991)
[156] M. Toivonen, P. Savolainen, H. Asonen, and M. Pessa, 'Solid-source MBE for growth of laser diode materials', *J. Crystal Growth*, **175/176**, 37 (1997)

[157] M. Pessa, M. Toivonen, M. Jalonen, P. Savolainen, and A. Salokatve, 'All-solid-source molecular beam epitaxy for growth of III-V compound semiconductors', *Thin Solid Films*, **306**, 237 (1997)

[158] M. Toivonen, 'All-Solid-Source Molecular Beam Epitaxy of III-V Compound Semiconductor devices', Tampere University of Technology, *Publications 222*, Doctoral Thesis (1997)

[159] P. Savolainen, M. Toivonen, J. Köngäs, M. Pessa, P. Corvini, and M. Jansen, 'Record quantum efficiency (92%) operation of 680 nm GaInP/AlGaInP ridge waveguide singlemode lasers', *Electron. Lett*., **34**, 1104 (1998)

[160] R. P. Schneider, Jr., and J. A. Lott, 'InAlP/InAlGaP distributed Bragg reflectors for visible vertical-cavity surface-emitting lasers', *Appl. Phys. Lett*., **62**, 2748 (1993)

[161] P. L. Gourley, R. M. Biefeld, T. J. Drummond, and T. E. Zipperian, 'Epitaxial semiconductor optical interference devices', *SPIE Proc.,* **792**, 178 (1987)

[162] M. H. MacDougal, S. G. Hummel, P. D. Dapkus, H. Zhao, and Y. Cheng, 'Epitaxial (Al, Ga)InP-oxide dstributed Bragg reflectors for use in visible-wavelength optical devices', *IEEE Photon. Technol. Lett.,* **7**, 385 (1995)

[163] J. M. Dallesasse, N. Holonyak, Jr., A. R. Sugg, T. A. Richard, and N. El-Zein, 'Hydrolyzation oxidation of $Al_xGa_{1-x}As$-AlAs-GaAs quantum well heterostructures and superlattices', *Appl. Phys. Lett*., **57**, 2235 (1990)

[164] R. L. Thornton, R. D. Burnham, and W. D. Streiffer, 'High reflectivity GaAs-AlGaAs mirrors fabricated by metalorganic chemical vapor deposition', *Appl. Phys. Lett*., **45**, 1028 (1984)

[165] J. P. van der Ziel and M. Ilegems, 'Multilayer GaAs-AlGaAs dielectric quarter wave stacks grown by molecular beam epitaxy', *Appl. Optics*, **15**, 1256 (1976)

[166] K. D. Choquette, K. M. Geib, C. I. H. Ashby, R. D. Twesten, O. Blum, H. Q. Hou, D. M. Follstaedt, B. E. Hammons, D. Mathes, and R. Hull, 'Advances in selective wet oxidation of AlGaAs alloys', *IEEE J. Selected Topics in Quantum Electron*., **3**, 916 (1997)

[167] J. A. Lott, R. P. Schneider, Jr., K. J. Malloy, S. P. Kilcoyne, and K. D. Choquette, 'Partial top dielectric stack distributed Bragg reflectors for red VCSEL arrays', *IEEE Photon. Tech. Lett*., **6**, 1397 (1994)

[168] K. L. Lear and R. P. Schneider, Jr., 'Uniparabolic mirror grading for vertical cavity surface emitting lasers', *Appl. Phys. Lett*., **68**, 605 (1996)

[169] R. P. Schneider, Jr., J. A. Lott, K. L. Lear, K. D. Choquette, M. H. Crawford, S. P. Kilcoyne, and J. J. Figiel, 'Metalorganic vapor phase epitaxial growth of red and infrared vertical-cavity surface-emitting laser diodes', *J. Crystal Growth*, **145**, 838 (1994)

[170] M. G. Peters, B. J. Thibeault, D. B. Young, J. W. Scott, F. H. Peters, A. C. Gossard, and L. A. Coldren, 'Band-gap engineered digital alloy interfaces for lower resistance vertical-cavity surface-emitting lasers', *Appl. Phys. Lett*., **63**, 3411 (1993)

[171] T. E. Sale, T. J. C. Hosea, and P. J. S. Thomas, 'Photomodulated reflectance as a valuable nondestructive process tool for VCSELs', *IEEE Photon. Technol. Lett*., **12**, 1328 (2000)

[172] M. Toivonen, P. Savolainen, and M. Pessa, 'High-performance GaInP/AlGaInP strained quantum well lasers grown by solid source molecular beam epitaxy', *Semicond. Sci. Technol*., **11**, 1923 (1996)

[173] J. Köngäs, P. Savolainen, M. Toivonen, S. Orsila, P. Corvini, M. Jansen, R. F. Nabiev, and M. Pessa, 'High-efficiency GaInP-AlGaInP ridge waveguide single-mode lasers operating at 650 nm', *IEEE Photon. Technol. Lett.*, **10**, 1533 (1998)

[174] P. Savolainen, M. Toivonen, J. Köngäs, M. Pessa, P. Corvini, and M. Jansen, 'Record quantum efficiency (92 %) operation of 680 nm GaInP/AlGaInP ridge waveguide singlemode lasers', *Electron. Lett.*, **34**, 1104 (1998)

[175] M. Jalonen, J. Köngäs, M. Toivonen, P. Savolainen, A. Salokatve, and M. Pessa', Monolithic super-bright red resonant cavity light-emitting diode grown by solid source molecular beam epitaxy', *IEEE Photon. Technol. Lett.*, **10**, 923 (1998)

[176] R. Wirth, C. Karnutsch, S. Kugler, and K. Streubel, 'High-efficiency resonant-cavity LEDs emitting at 650 nm', *IEEE Photon. Technol. Lett.*, **13**, 421 (2001)

[177] A. I. Onischenko, T. E. Sale, E. P. O'Reilly, A. R. Adams, S. M. Pinches, J. E. F. Frost, and J. Woodhead, 'Progress in the design and development of AlGaInP visible VCSELs', *IEE Proc. Optoelectron.*, **147**, 15 (2000)

[178] FC100-02 RCLED Data Sheet 07-11-2001 at *http://www.firecomms.com*

[179] P. Modak, M. D'Hondt, D. Delbeke, I. Moerman, P. van Daele, R. Baets, P. Demeester, and p. Mijlemans, 'AlGaInP Microcavity light-emitting diodes at 650 nm on Ge substrates', *IEEE Photon. Technol. Lett.*, **12**, 957 (2000)

[180] P. Modak, M. D'Hondt, I. Moerman, P. van Daele, P. Mijlemans, and P. Demeester, '5.2 % efficiency InAlGaP microcavity LEDs at 640 nm on Ge substrates', *Electron. Lett.*, **37**, 377 (2001)

[181] J. W. Gray, Y. S. Jalili, P. N. Stavrinou, M. Whitehead, G. Parry, A. Joel, R. Robjohn, R. Petrie, S. Hunjan, P. Gong, and G. Duggan, 'High-efficiency, low voltage resonant-cavity light-emitting diodes operating around 650 nm', *Electron. Lett.*, **36**, 1730 (2000)

[182] Appendix 12

[183] M. Born and E. Wolf, 'Priciples of optics', Cambridge University Press, Cambridge (1999)

[184] Appendix 4

[185] J. Talghader, and J. S. Smith, 'Thermal dependence of the refractive index of GaAs and AlAs measured using semiconductor multilayer optical cavities', *Appl. Phys. Lett.*, **66**, 335 (1995)

[186] Appendix 1

[187] Appendix 12

[188] Appendix 7

[189] H. Martinsson, J. Bengysson, M. Ghisoni, and A. Larsson, 'Monolithic integration of vertical-cavity surface-emitting laser and diffractive optical element for advanced beam shaping', *IEEE Photon. Technol. Lett.*, **11**, 503 (1999)

[190] D. W. Prather, S. Venkataraman, M. Lecompte, F. Kiamilev, J. N. Mait, and G. J. Simonis, 'Optoelectronic multichip module integration for chip level optical interconnects', *IEEE Photon. Technol. Lett.*, **12**, 1112 (2001)

[191] Appendix 10

[192] P. Savolainen, M. Toivonen, M. Pessa, P. Corvini, M. Jansen, and R. F. Nabiev, 'Red lasers grown by all-solid-source molecular beam epitaxy', *Semicond. Sci. Technol.*, **14**, 425 (1999)

[193] A. E. Bond, P. D. Dapkus, and J. D. O'Brien, 'Design of low-loss single-mode vertical-cavity surface-emitting lasers', *IEEE J. Selected Topics in Quantum Electron.*, **5**, 674 (1999)

[194] B. Demeulenaere, P. Bienstman, B. Dhoedt, and R. G. Baets, 'Detailed study of AlAs-oxidized apertures in VCSEL cavities for optimized modal performance', *IEEE J. Quantum Electron.*, **35**, 358 (1999)

[195] Y. –Z. Huang, 'Influence of lateral propagating modes on laser output characteristics in selectively oxidized vertical cavity surface-emitting lasers with double oxide layers', *J. Appl. Phys.*, **86**, 3519 (1999)

[196] BREDSELS 23455: Long term research report

[197] A. Knigge, M. Zorn, H. Wenzel, M. Weyers, and G. Tränkle, 'High efficiency AlGaInP-based 650 nm vertical-cavity surface-emitting lasers', *Electron. Lett.*, **37**, 1222 (2001)

[198] K. Tai, K. –F. Huang, C. –C. Wu, and J. D. Wynn, 'Visible InGaP/InGaAlP quantum well top surface emitting laser diodes', *Appl. Phys. Lett.*, **63**, 2732 (1993)

[199] A. Bhattacharya, M. Zorn, A. Oster, M. Nasarek, H. Wenzel, J. Sebastian, M. Weyers, and G. Tränkle, 'Optimization of MOVPE growth for 650 nm-emitting VCSELs', *J. Crystal Growth*, **221**, 663 (2000)

[200] T. Calvert, B. Corbett, and J. D. Lambkin, '80 °C continuous wave operation of AlGaInP based visible VCSEL', *Electron. Lett.*, **38**, 222 (2002)

[201] A. Tandon, S. W. Corzine, R. P. Schneider, Jr., and M. R. Tan, 'Red VCSELs for low-cost POF-based data links', *SPIE Proc.*, **3946** (2000)

[202] SV3644-001 VCSEL Data Sheet at *http://www.honeywell.com*

[203] Appendix 11

[204] M. Hagerott Crawford, R. P. Schneider, Jr., K. D. Choquette, K. L. Lear, S. P. Kilcoyne, and J. J. Figiel, 'High efficiency AlGaInP-based 660-680 nm vertical-cavity surface emitting lasers', *Electron. Lett.*, **31**, 196 (1995)

[205] M. Hagerott Crawford, R. P. Schneider, Jr., K. D. Choquette, and K. L. Lear, 'Temperature-dependent characteristics and single-mode performance of AlGaInP-based 670-690-nm vertical-cavity surface-emitting lasers', *IEEE Photon. Technol. Lett.*, **7**, 724 (1995)

[206] M. J. Hafich, K. D. Choquette, M. Hagerott Crawford, K. M. Geib, and J. J. Hindi, 'Selectively oxidized VCSELs at Sandia', *SPIE Proc.*, **3946** (2000)

[207] K. Takaoka, M. Ishikawa, and G. Hatakoshi, 'Low-threshold and high-temperature operation of InGaAlP-based proton-implanted red VCSELs', *IEEE J. Selected Topics in Quantum Electron.*, **7**, 381 (2001)

[208] Y. H. Chen, C. I. Wilkison, J. Woodhead, C. C. Button, J. P. R. David, M. A. Pate, and P. N. Robson, 'Polarisation characteristics of InGaAlP/AlGaAs visible vertical cavity surface emitting lasers', *Electron. Lett.*, **32**, 559 (1996)

[209] R. Butendeich, D. Graef, J. Schwarz, T. Ballmann, H. Schweizer, and F. Scholz, 'Low threshold current densities in red VCSELs', *J. Crystal Growth*, **221**, 657 (2000)

[210] R. Stevens, R. Marcks Von Würtemberg, R. Schatz, and K. Streubel, 'High-speed visible VCSEL for POF data links', *SPIE Proc.*, **3946** (2000)

[211] R. W. Herrick, and P. M. Petroff, 'Improved reliability of red GaInP vertical-cavity surface-emitting lasers using bias-induced annealing', *Appl. Phys. Lett.*, **72**, 1799 (1998)

Appendices

Appendix 1.

Publication 1.

P. Sipilä, M. Saarinen, M. Guina, V. Vilokkinen, M. Toivonen, and M. Pessa, 'Temperature behaviour of resonant cavity light-emitting diodes at 650 nm', *Semicondutor Science and Technology*, **15**, 418 (2000)

Reproduced by permission of the publisher.
Copyright 2000 by IOP Publishing Limited.
Journal homepage http://www.iop.org/journals/sst.

Publication 2.

M. Dumitrescu, L. Toikkanen, P. Sipilä, V. Vilokkinen, P. Melanen, M. Saarinen, S. Orsila, P. Savolainen, M. Toivonen, and M. Pessa, 'Modeling and optimization of resonant cavity light-emitting diodes grown by solid source molecular beam epitaxy', *Microelectronic Engineering*, **51-52**, 449 (2000)

Reproduced by permission of the publisher.
Copyright 2000 by Elsevier Science.

Publication 3.

M. Guina, S. Orsila, M. Dumitrescu, M. Saarinen, P. Sipilä, V. Vilokkinen, B. Roycroft, P. Uusimaa, M. Toivonen, and M. Pessa, 'Light-emitting diode emitting at 650 nm with 200-MHz small-signal modulation bandwidth', *IEEE Photonics Technology Letters*, **12**, 786 (2000)

Reproduced by permission of the publisher.
Copyright 2000 by IEEE.

Publication 4.

M. Guina, J. Dekker, A. Tukiainen, S. Orsila, M. Saarinen, M. Dumitrescu, P. Sipilä, P. Savolainen, and M. Pessa, 'Influence of deep level impurities on modulation response of InGaP light emitting diodes', *Journal of Applied Physics*, **89**, 1151 (2001)

Reproduced by permission of the publisher.
Copyright 2001 by AIP.

Appendix 5.

Publication 5.

M. Saarinen, V. Vilokkinen, M. Dumitrescu, and M. Pessa, 'Resonant-cavity light-emitting diodes operating at 655 nm with high external quantum efficiency and light power', *IEEE Photonics Technology Letters*, **13**, 10 (2001)

Reproduced by permission of the publisher.
Copyright 2001 by IEEE.

Appendix 6.

Publication 6.

M. Pessa, M. Guina, M. Dumitrescu, I. Hirvonen, M. Saarinen, L. Toikkanen, and N. Xiang, 'Resonant cavity light emitting diode for a polymer optical fibre system', *Semiconductor Science and Technology, Topical Review*, **17**, R1 (2002)

Reproduced by permission of the publisher.
Copyright 2002 by IOP Publishing Limited.
Journal homepage http://www.iop.org/journals/sst.

Publication 7.

M. M. Dumitrescu, M. J. Saarinen, M. D. Guina, and M. V. Pessa, 'High speed resonant cavity light emitting diodes at 650 nm', *IEEE Journal of Selected Topics in Quantum Electronics*, **8**, 219 (2002)

Reproduced by permission of the publisher.
Copyright 2002 by IEEE.

Publication 8.

M. Saarinen, M. Toivonen, N. Xiang, V. Vilokkinen, and M. Pessa, 'Room-temperature CW operation of red vertical-cavity surface-emitting lasers grown by solid-source molecular beam epitaxy', *Electronics Letters*, **36**, 1210 (2000)

Reproduced by permission of the publisher.
Copyright 2000 by IEE.

Publication 9.

M. Saarinen, V. Vilokkinen, P. Sipilä, N. Xiang, S. Orsila, M. Guina, P. Melanen, M. Dumitrescu, P. Uusimaa, P. Savolainen, and M. Pessa, 'Visible vertical cavity light emitters for fibre optical communication', (Invited Paper), *Electrochemical Society XXXIII SOTAPOCS Proceedings*, **18**, 49 (2000)

Reproduced by permission of the publisher.
Copyright 2000 by The Electrochemical Society, Inc.

Publication 10.

M. Saarinen, N. Xiang, V. Vilokkinen, P. Melanen, S. Orsila, P. Uusimaa, P. Savolainen, M. Toivonen, and M. Pessa, 'Red vertical-cavity surface-emitting lasers grown by solid-source molecular beam epitaxy', *Journal of Crystal Growth*, **227-228**, 324 (2001)

Reproduced by permission of the publisher.
Copyright 2001 by Elsevier Science.

Appendix 11.

Publication 11.

M. Saarinen, N. Xiang, M. Dumitrescu, V. Vilokkinen, P. Melanen, S. Orsila, P. Uusimaa, P. Savolainen, and M. Pessa, 'Visible-light vertical-cavity surface-emitting lasers grown by solid-source molecular beam epitaxy', *SPIE Proceedings*, **4286**, 156 (2001)

Reproduced by permission of the publisher.
Copyright 2001 by International Society for Optical Engineering.

Appendix 12.

Publication 12.

M. Dumitrescu, M. Saarinen, N. Xiang, M. Guina, V. Vilokkinen, and M. Pessa, 'Red wavelength range microcavity emitters', *Physica Status Solidi (A)*, **188**, 943 (2001)

Reproduced by permission of the publisher.
Copyright 2001 by Wiley-VCH.

Appendix 13.

Publication 13.

M. Saarinen, N. Xiang, M. Dumitrescu, M. Guina, I. Hirvonen, L. Toikkanen, and M. Pessa, 'Vertical cavity light emitters for plastic optical fibers', (Invited Paper), accepted for publication, 2002 issue, *Physica Scripta* (2002)

Reproduced by permission of the publisher.
Copyright 2002 by Physica Scripta within
The Royal Swedish Academy of Sciences.

Tampereen teknillinen korkeakoulu
PL 527
33101 Tampere

Tampere University of Technology
P. O. B. 527
FIN-33101 Tampere Finland